University of Alberta

SURFACE MODIFICATION OF ZIRCONIUM IMPLANTS VIA ELECTROCHEMICAL ANODIZATION AND WET CHEMICAL TECHNIQUES

by

LUNING WANG

A thesis submitted to the Faculty of Graduate Studies and Research
in partial fulfillment of the requirements for the degree of

DOCTOR OF PHILOSOPHY

IN MATERIALS ENGINEERING

DEPARTMENT OF CHEMICAL AND MATERIALS ENGINEERING

FALL 2011
Edmonton, Alberta

Dedication

To my wife, Chun Lu,
my daughter, Iris Wang,
and my parents

ABSTRACT

Metals such as titanium (Ti) and zirconium (Zr) have been widely applied in the orthopaedic and orthodontic field for construction of joint replacement prostheses and teeth implants due to their lower cytotoxicity, excellent mechanical properties, and corrosion resistance. However, the current 15-20 year life span has been a challenging problem for metal-based orthopedic materials. Limited cytocompatibility properties and osseointegration of implants with surrounding bone has been proposed as one of the leading causes of such limited lifetimes.

To improve the cytocompatibility properties of metal orthopedic implants, nanotechnology has been used to create nano-featured thin oxide films (through electrochemical anodization) on metal surfaces, such as nanotubular arrays. This thesis describes the fabrication of zirconium dioxide (ZrO_2) nanotubular arrays on Zr surfaces and several efficient techniques to enhance the biocompatibility of as-formed ZrO_2 nanotubular arrays via simple wet chemistry treatments.

A series of highly ordered ZrO_2 nanotubular array films with different thickness was synthesized in fluoride containing electrolyte by changing the anodic voltage or anodization period. Geometrical factors such as thickness and diameter of nanotubular openings depend on anodization voltage and anodization period. Mechanical properties such as apparent Young's modulus, ratio of elastic energy to the total deformation energy, and hardness are highly dependent on thickness but not on diameter of nanotubular openings. Resistance of nanotubular arrays to

sliding wear and wear loss of nanotubular arrays vary with the culture used.

Several wet chemical techniques including the evaporation-based immersion technique and accelerated immersion method have been explored and found to enhance considerably the bioactivity of ZrO_2 nanotubular arrays by enhancing the capability of formation thereon of the hydroxyapatite (HA) layer in simulated biological culture. In this work, I found that a combination of anodic ZrO_2 nanotubular arrays and wet chemical treatment achieves the required significant improvement of bioactivity of Zr implant.

ACKNOWLEDGEMENTS

I would like to take this opportunity to express my gratitude to all the people who provided great help for my Ph.D studies.

Firstly, I would like to express my sincere gratitude and appreciation to my supervisor, Professor Jingli Luo, whose guidance and encouragement gave me much help throughout the whole course of this study. From her I learned how to find, analyze and solve the problems encountered during research. More importantly, her enthusiasm and hospitability for scientific research set an excellent example for me. I believe that all I learned from her will help me through my whole life.

My deep appreciation also goes to my supervisor committee members, Professor Thomas H. Etsell and Professor Weixing Chen for their stimulating and greatly helpful suggestion during the progress of this research. Every time I met with them I learned from them, not only knowledge, but also their attitude toward research.

I greatly thank Drs. Weifeng Wei, Xinwei Cui and Xinhu Tang for their valuable help for my research. Their encouragement has helped me overcome the hardships during this work. Every time I talked with them, I always learned more than I expected.

I sincerely thank Dr. Lawrence H. Le for his encouragement for my graduate study. I would also like to extend my appreciation to Drs. Renkang Zhu, Lianpeng Tian, Xianzhu Fu, Cindy Xing Yin, Mr. Yu Yang, Mr. Wei Zhu and Ms. Nan Luo for their help, friendship, and contributions towards a wonderful research environment.

I acknowledge and appreciate Natural Science and Engineering Research Council of Canada (NSERC) for the financial support for this research.

Finally, my special thanks are given to my parents and my wife, Chun Lu, for their endless love, selfless support, and invaluable encouragement. Without them,

all of this would have been only a dream. This thesis is also for my lovely daughter, Iris Wang.

Table of Content

Chapter 1 Introduction 1

References 3

Chapter 2 Literature review 7

2.1 History of orthopedic replacements 7

2.2 Metallic materials for orthopedic prostheses 8

2.3 Surface modification of metallic implants 12

2.3.1 Surface modification via calcium phosphate coating 13

2.3.1.1 Thermal spraying HA coating 14

2.3.1.2 Plasma sprayed HA coating 14

2.3.1.3 Physical vapour deposition (PVD) and chemical vapour deposition (CVD) technique 15

2.3.1.4 Electrochemically-assisted deposition 17

2.3.1.5 Biomimetic deposition 20

2.4 Anodization modification of porous oxide layers 22

2.4.1 Micro-porous oxide films 24

2.4.2 Anodization of self-assembled nanoporous and nanotubular structure 27

2.4.2.1 Mechanisms of anodic self-assembled nanotubular structures 29

2.4.2.2 Geometry and structure of the anodic metal oxide nanotubular arrays 31

2.4.2.3 Biomedical application of anodic oxide nanotubular arrays 33

2.4.2.4 Anodic ZrO_2 nanotubular arrays 36

2.5 Summary of present status of surface modification on metallic implants and topic selection 37

References 44

Chapter 3 Experimental methods and Materials Characterization 69

3.1 Fabrication of anodic ZrO_2 nanotubular arrays 69

3.2 Materials characterization methods 69

3.2.1 Scanning electron microscope 69

3.2.2 Energy dispersive x-ray spectroscopy 71

3.2.3 X-ray diffraction 71

3.2.4 X-ray photoelectron spectroscopy 72
3.2.5 Fourier transform infrared spectroscopy 73
3.2.6 Transmission electron microscopy 73
3.2.7 Secondary ion mass spectrometry 75
3.2.8 Microindentation test 75
3.2.9 Universal Micro-Tribometer (UMT) for critical load and scratch test 76
3.210 Bonding strength of HA coating 77
3.3 Evaluation of the bioactivity of zirconium dioxide nanotubular arrays.. 77
References 83
Chapter 4 Fabrication and mechanical properties of anodized zirconium dioxide nanotubular arrays 85
4.1 Introduction 85
4.2 Results and discussion 85
4.2.1 Formation of ZrO_2 nanotubular arrays 85
4.2.2 Microindentation on ZrO_2 nanotubular arrays 88
4.2.3 Microscratch on ZrO_2 nanotubular arrays 92
4.4 Conclusions 96
References 105
Chapter 5 Enhancement of the capability of hydroxyapatite formation on anodic ZrO_2 nanotubular arrays via an effective chemical dipping treatment 108
5.1 Introduction 108
5.2 Experimental solution and comparison specimen 108
5.2.1 Dipping treatment of ZrO_2 nanotubular arrays 108
5.2.2 Comparison samples 109
5.3 Results 110
5.3.1 Fabrication of ZrO_2 nanotubular arrays 110
5.3.2 Dipping treatment on ZrO_2 nanotubular arrays 111
5.3.3 Formation of HA on dipping treated ZrO_2 nanotubular arrays 112
5.3.4 Bonding strength of HA coating 116
5.4 Discussion 117
5.5 Conclusions 120
References 135
Chapter 6 Fabrication and formation of bioactive anodic zirconium oxide

nanotubes containing presynthesized hydroxyapatite via alternative immersion method……..138
6.1 Introduction 138
6.2 The AIM treatment process 138
6.3 Results and discussions 139
6.3.1 The formation and structure of ZrO_2 nanotubes 139
6.3.2 The AIM treatment on ZrO_2 nanotubes 141
6.3.3 The HA formations on AIM treated ZrO_2 nanotubes 142
6.4 Conclusions 145
References 155
Chapter 7 Enhancing the bioactivity of zirconium with the coating of anodized ZrO_2 nanotubular arrays prepared in phosphate containing electrolyte 157
7.1 Introduction 157
7.2 Materials and methods 157
7.3 Results and discussions 158
7.4 Conclusions 162
References 167
Chapter 8 Summary and future directions 168
8.1 Main conclusions 168
8.2 Contributions to the knowledge 169
8.3 Recommendations for future work 170
Appendix I Formation of Hydroxyapatite Coating on Anodic Titanium Dioxide Nanotubes via an Efficient Dipping Treatment 173
AI.1 Introduction 173
AI.2 Experimental procedures 175
AI.2.1 TiO_2 nanotube formation 175
AI.2.2 The dipping method 176
AI.2.3 HA formation 177
AI.2.4 Surface characterizations 177
AI.3 Results 179
AI.3.1 The structure of TiO_2 nanotubes 179
AI.3.2 Dipping effect on the precipitation on TiO_2 nanotubes 180

AI.3.3 Formation of HA coating on TiO_2 nanotubes with dipping treatment 181
AI.3.4 The bonding strength of the HA coating..... 182
AI.4 Discussion..... 183
AI.5 Conclusions..... 186
References..... 200

List of Tables

Table 2-1 Requirements for joint implant materials [6,10]..... 9

Table 2-2 Comparison of the mechanical properties of metal implant alloys [12,14,23,24]..... 12

Table 3-1 Ion Concentrations in SBF and Human Blood Plasma. [10,11] ... 78

Table 4-1 Critical Load for Nanotubular Arrays Fabricated under Various Conditions..... 93

Table 5-1 Ion Concentrations in ACS and SBF. [1-3]..... 109

Table 5-2 Characterization of materials from FTIR spectra. [12, 13].....116

Table 6.2 The corresponding wavenumber of FTIR spectra..... 146

Table AI.1 Ion Concentrations of SBF and Human Blood Plasma..... 177

Table AI.2 Characterization of materials from FTIR spectra..... 183

List of Figures

Figure 2-1 Total joint replacement arthroplasty: (a) Charnley-Muller total hip replacement; (b) geometric total knee replacement; (c) Newton total ankle replacement; (d) Stanmore total shoulder replacement; (e) Fenlin total shoulder replacement; (f) Dee total elbow replacement; (g) Meuli total wrist replacement (adapted from [9]). 41

Figure 2-2 Schematic diagram of the evolution of straight nanotubes at a constant anodization voltage, as follows: (a) oxide layer formation; (b) pit formation on the oxide layer; (c) growth of the pit into scallop-shaped pores; (d) the metallic part between the pores undergoes oxidation and field-assisted dissolution; and (e) fully developed nanotubes (Adapted from [93, 119]). . 42

Figure 2-3 (a) SEM image of cross section and (b) HRTEM image and diffraction pattern of ZrO_2 nanotubular arrays (Adapted from [149]). 43

Figure 3-1 Schematic diagram of setup for electrochemical anodization of zirconium dioxide nanotubular arrays. 79

Figure 3-2 Schematic of load-displacement curve for an instrumented microindentation test. 80

Figure 3-3 Schematic diagram of the setup for scratch test by applying UMT. 81

Figure 3-4 Schematic of the bonding strength test of the HA coating to the substrate. 82

Figure 4-1 FE-SEM images of ZrO_2 nanotubular arrays fabricated at 30 V for 24 hrs: (A) top view, (B) bottom view, (C) cross-sectional view and the inserted image of the magnified view, and (D) TEM image of ZrO_2 nanotube and the inserted image of the diffraction pattern. 98

Figure 4-2 The growth curve of ZrO_2 nanotubular arrays fabricated at 30 V. The SEM images show the nanotubular opening and thickness at 4 hrs and 24 hrs anodization. 99

Figure 4-3 The comparison of nanotubular array thickness and diameter at different anodized voltage for 24 hrs anodization. 100

Figure 4-4 Mechanical properties of a series of ZrO_2 nanotubular arrays fabricated at 30 V with various anodization durations: (a) apparent Young's modulus (Y), (b) ratio of elastic energy (W_e) to total energy (W_{tot}), (c) hardness (HV), and (d) maximum depth (h_{max}). The aspect ratio of each nanotubular arrays was used to illustrate the relationship. 101

Figure 4-5 Mechanical properties of a series of ZrO_2 nanotubular arrays fabricated at 15 V, 20 V, 25 V, and 30 V in 24 hrs duration: (a) apparent Young's modulus (Y), (b) ratio of elastic energy (W_e) to total energy (W_{tot}), (c) hardness (HV), and (d) maximum depth (h_{max}). The aspect ratio of each nanotubular arrays was used to illustrate the relationship. 102

Figure 4-6 FE-SEM images: (a) typical microindentation on the surface of ZrO_2 nanotubular arrays; and (b) the magnified image showing the deformation and densification of the nanotubes. 103

Figure 4-7 (a) The scratch track by sliding the nanotubular layer in air, (b) the scratch track by sliding the nanotubular layer in pH=13 solution, (c) the comparison of the width of the scratch track obtained under different conditions, and (d) the friction force curves versus time under different conditions. 104

Figure 5-1 Schematic outline of the dipping treatment leading to deposition of CaP on ZrO_2 nanotubular arrays. 122

Figure 5-2 SEM images of surface morphology of anodic ZrO_2 nanotube structures; anodized for 20 min at: (a) 50 V; (b) 32 V; (c) 20 V; and (d) a bottom view of the sample for (a). 123

Figure 5-3 (a) Relationship between nanotube diameter, length, and applied voltage for 20 min anodization, and (b) kinetic curves of ZrO_2 nanotubular arrays anodized at different applied voltages for 20 min. 124

Figure 5-4 SEM image of surface morphology of ZrO_2 nanotubes anodized at 50 V for 20 min: after dipping (a) 4 times and (b) 8 times; (c) EDX spectra of the surface composition after different dipping treatments; (d) XPS spectrum of P-2p peak; (e) the amount of Ca deposited on the tubes as a function of cycles of dipping treatment. 125

Figure 5-5 SEM images of the dipping-treated ZrO_2 nanotubular arrays immersion in SBF for different periods: (a) 1 day; (b) 2 days; (c) 4 days; and (d) 8 days; (e) EDX spectrum of the sample for (d); (f) SEM cross section view of the HA coating formed after 8 days of immersion in SBF. 126

Figure 5-6 Effect of geometrical factors on the deposited HA coating formation: (a) mass increment of the samples as a function of tubular inner diameter after dipping treatment and soaking for up to 8 days, and (b) mass increment of the samples as a function of tubular length after dipping treatment and soaking for up to 8 days. 127

Figure 5-7 SEM top views of nanotubular arrays with: (a) dipping treatment; (c) no dipping treatment; (e) annealed at 200 ^oC after SBF soaking for 8 days;

and the corresponding EDX spectra (b), (d) and (e); (g) mass increments of the unannealed and annealed samples after dipping treatment and after SBF soaking for 2 and 8 days each, without and with the dipping treatment. ... 128

Figure 5-8 XRD patterns of the ZrO_2 nanotubular arrays: (a) before treatment; and after immersion in SBF for: (b) 2 days; (c) 4 days; and (d) 8 days. 129

Figure 5-19 FT-IR spectra of the HA coating on ZrO_2 nanotubular arrays with dipping treatment after 8 days of immersion in SBF. 130

Figure 5-10 XPS spectra showing peaks for Ca-2p, P-2p, Mg-2p, and Na-1s for the HA coating grown in SBF for 8 days. 131

Figure 5-11 (a) SEM image of the fracture surface of the substrate, and (b) EDX mapping of Ca; (c) SEM image of the fracture surface part of a steel bar, and (d) EDX mapping of Ca. 132

Figure 5-12 Proposed mechanism for the dipping treatment of ZrO_2 nanotubular arrays: (a) the Zr substrate with the ZrO_2 nanotubes dip and withdraw in ACS; (b) a wetting film filling in the nanotubes structure; (c) the film drying and forming CaP crystallites, and other crystalline chemicals, such as NaCl, KCl, and tris; CaP adheres to the nanotubes; (d) during the repeated dip-and-withdraw procedures, more and more CaP forms and adheres to the nanotubes; (e) the formation of CaP crystallites covers nanotubes after rinsing and drying (adapted from [5, 16]). 133

Figure 5-13 Schematic representation of the fracture mode of HA coating on ZrO_2 nanotubular arrays. 134

Figure 6-1 An example of SEM image of ZrO_2 nanotubular formed at 30V for 1h: (a) top view; (b) higher magnification of (a); (c) the side view and (d) the higher magnification of (c). 147

Figure 6-2 The relationship between (a) tube diameter, length and the anodization voltage and (b) anodization time at 30 V and the tube length. 148

Figure 6-3 The SEM top view of the 20 cycles AIM treated ZrO_2 nanotubular arrays (a) and the higher magnification (b); XPS spectra of the Ca-2p and P-2p of the AIM treated AIM (c); The relationship between atomic concentration of Ca and the AIM treated times (d); The XRD spectra of the non-treated ZrO_2 nanotubular arrays and the AIM treated ZrO_2 nanotubular arrays (e). 149

Figure 6-4 Dependence of weight gain of the samples on the tube diameter (a) and the tube length (b) after HA loading by AIM and immersion in SBF for 2 days and 5 days. 150

Figure 6-5 SEM images of the AIM-treated samples immersion in SBF for 2d

(a) and the corresponding EDX spectrum (b); 5 d (c) and the corresponding EDX spectrum (d); the annealed sample immersion in SBF for 5 d (e) and the corresponding EDX spectrum (f); the annealed sample after AIM treatment and immersion in SBF for 5d (g) and the weight gain of the non-annealed and annealed samples after soaking in SBF for 2 and 5 d with and without AIM treatment (h). 151

Figure 6-6 The XRD spectrum of the scratched HA coating after 5 days immersion in SBF. 152

Figure 6-7 FT-IR spectrum of the HA coating after immersion in SBF for 5days. 153

Figure 6-8 XPS P2p, Ca2p, Mg 2p and Na 1s peaks recorded from the HA coating that was grown in SBF for 5 days. 154

Figure 7-1 SEM images of ZrO_2 nanotubular arrays formed at 30 V for 1 h in ethylene glycerin containing 5 vol% H_2O, 0.35 M NH_4F and 0.05 M $(NH_4)_2HPO_4$: (a) cross-section and (b) top view; and TEM images of ZrO_2 nanotubular arrays formed in glycerin containing 5 vol% H_2O, 0.35 M NH_4F (c) with and (d) without 0.05 M $(NH_4)_2HPO_4$. 163

Figure 7-2 (a) Influence of applied voltage on the nanotubular arrays diameter and layer thickness, and (b) dependence of ZrO_2 nanotubular thickness on the anodization period at 30 V. 164

Figure 7-3 A survey of XPS spectra of anodic ZrO_2 nanotubular arrays obtained in: (a) glycerin containing 5 vol% H_2O, 0.35 M NH_4F and (b) 0.05 M $(NH_4)_2HPO_4$; (c) XPS spectra of Zr-3d and P-2p; and (d) ToF-SIMS over the cross section of the ZrO_2 nanotubular arrays. 165

Figure 7-4 SEM images of ZrO_2 nanotubular arrays formed in (a) phosphate-containing and (b) phosphate-free electrolytes after soaking in SBF for 8 days, the inserted figure showing the EDX spectrum; (c) XRD profile of intact Zr, (d) anodized ZrO_2 nanotubular arrays, (e) HA coating formed on ZrO_2 after soaking in SBF for 8 days. 166

Figure AI-1 Schematic of the procedure for dipping treatment. 188

Figure AI-2 Schematic of the bonding strength test of the HA coating to the substrate. 189

Figure AI-3 FE-SEM images showing top view and the side view (the inserts) of TiO_2 nanotubes after different anodization periods (a): 20 min, (b) 40 min, (c) 100 min, and (d) the relationship between nanotube length and anodization period. 190

Figure AI-4 FE-SEM images of TiO_2 nanotubes after different numbers of cycles of dipping treatment: (a) and (c) are the top view and side view , respectively, of the TiO_2 nanotubes after dipping for twice; (b) and (d) are the top view and side view, respectively, of the TiO_2 nanotubes after dipping eight times..... 191

Figure AI-5 (a) XPS spectra showing Ca-2p peaks before and after eight times of dipping treatment, and(b) the atomic concentration of Ca as a function of number of cycles of dipping treatment. 192

Figure AI-6 SIMS spectra of the TiO_2 nanotube structure after eight times of dipping. 193

Figure AI-7 SEM images the TiO_2 nanotubes immersed in SBF for different periods: (a) 2 days and (b) 4 days; the insertion presents the EDX spectrum. 194

Figure AI-8 (a) SEM images of TiO_2 nanotubes annealed at 723 K (450 ^oC) for 3 hr and then immersed in SBF for 4 days and (b) the corresponding EDX spectrum; (c) annealed at 823 K (550 ^oC) for 3 h and then immersed in SBF for 4 days and (d) the corresponding EDX spectrum..... 195

Figure AI-9 TF-XRD patterns of the TiO_2 nanotube structure: (a) before treatment, (b) after immersion in SBF for 2 days, and (c) after 4 days,, and the standard pattern for HA (JCPDF 09-0432). 196

Figure AI-10 FT-IR spectra of the HA coating on TiO_2 nanotubes with dipping treatment after 4 days of immersion in SBF. 197

Figure AI-11 (a) Comparison of the tensile bonding strengths of HA layers bonded to different substrates; (b) FE-SEM image of the fracture surface of the substrate; and EDX mapping of the elements (c) Ca, (d) P, and (e) Ti at the fracture surface. 198

Figure AI-12 Proposed mechanism of the dipping treatment on the TiO_2 nanotube: (a) the Ti substrate with the TiO_2 nanotubes dip and withdraw in the ACS; (b) a wetting film filled in the nanotubes structure; (c) the film dries and results in the formation of CaP crystalline and other chemical crystalline, such as NaCl, KCl, and tris; some CaP adheres to the nanotubes; (d) during the repeated dip-and-withdraw procedures, more and more CaP forms and adheres to the nanotubes; (e) the formation of CaP crystalline covers nanotubes after rinsing and drying (adapted from [25] and [44]). 199

Chapter 1 Introduction

Metal-based biomaterials are extensively used to replace hard tissue in human bodies. It is estimated that more than 500,000 artificial alloy-based joints, mainly hips and knees, and about 100,000-300,000 tooth roots are implanted *in vivo* every year in the United States alone [1,2]. Moreover, the markets for biomedical implants are growing globally as the population increasingly ages. It is predicted that the needs for implants will keep increasing. Ultimately, implant materials must possess an appropriate combination of mechanical, chemical, and biological properties. However, it is difficult for any single material to have all the required properties. By applying proper surface modifications, desirable properties from different materials can be combined during the product manufacture [3].

Metals such as titanium (Ti) and zirconium (Zr), commonly used in manufacture of valves, have been widely applied in the orthopaedic and orthodontic field for making joint replacement prostheses and teeth implants due to their low cytotoxicity, excellent mechanical properties, and corrosion resistance [4-6]. However, their expected 15-20 year life span has been a challenging problem for metallic-based orthopedic materials. Limited cytocompatibility properties and osseointegration of implants to surrounding bone have been proposed as the leading causes of such limited lifetimes [7].

As a result, many attempts have been made to improve the surface properties of

titanium-based implants (e.g., topography, chemistry and surface energy), and these directly determine the implant-environment interactions after implantation. These surface modification techniques include mechanical methods (e.g. sand-blasting), chemical methods (e.g. acid etching), coatings (e.g. plasma spraying), etc. [8-10]. Among the conventional techniques used an electrochemical method, termed anodization or anodic oxidation, is well established for improved lifetimes of valve metals, such as Al and Ti, through formation of oxide layers, and also has been successfully used in the past few decades as a surface treatment for improving lifetimes of orthopedic implants. To the same purpose, additional recent new advances include forming nanostructure features [11].

Nanotechnology has been explored to modify the surface geometry and chemical properties of metallic implants [12]. Fabrication processes including *in situ* formation of highly-ordered nanoporous and nanotubular oxide film have recently been shown to be an attractive technique to modify the surface geometry and chemical properties of metallic implants [13,14]. In addition, to improve their biocompatibility, various processes that have been carried out to form a bioactive ceramic coating such as hydroxyapatite (HA, $Ca_{10}(PO_4)_6(OH)_2$) have been proposed, such as a plasma spray method [15,16]. Since the nanoporous or nanotubular structure possesses an empty volume which then can be filled with bioactivating species and provide an interface suitable for anchoring connective tissues, it seemed straightforward to combine the formation of nanotubular layers

and ceramic coatings to improve the biocompatibility of the metal components [17].

Additionally, new metallic implant materials such as Zr has been introduced to overcome the higher magnetic susceptibility of other metals including Ti and stainless steel [13,18]. For these reasons, the objective of this research was to explore the technique for fabrication of ZrO_2 nanotubular arrays and evaluate their mechanical properties for biomedical applications. To achieve this goal several wet chemical techniques were explored for applying bioactive HA coatings on the nanotubular structures from a simulated biological environment. These combinations of nanotubular structure and the HA coating were anticipated to offer acceleration of establishing the interaction between the implant and surrounding tissues during the implantation.

References

[1] G.L. Bowlin, G. Wnek, Encyclopedia of biomaterials and biomedical engineering, Taylor & Francis Group, Boca Raton, FL, 2004.

[2] C.G. Moran, T.C. Horton, Total knee replacement: the joint of the decade. A successful operation, for which there's a large unmet need, BMJ J. 320 (2000) 820.

[3] K. Duan, R.Z. Wang, Surface modifications of bone implants through wet chemistry, J. Mater. Chem. 16 (2006) 2309-2321.

[4] S.A. Brown, J.E. Lemons, Medical Applications of Titanium and its Alloys : The Material and Biological Issues, ASTM Store, West Conshohocken, PA, 1996.

[5] M. Niinomi, Recent applications, research and development in titanium and its alloys, Tetsu to Hagane-Journal of the Iron and Steel Institute of Japan. 90 (2004) 462-471.

[6] A. Wennerberg, T. Albrektsson, On implant surfaces: a review of current knowledge and opinions, Int. J. Oral Maxillofac. Implants. 25 (2010) 63-74.

[7] K. Bordji, J.Y. Jouzeau, D. Mainard, E. Payan, P. Netter, K.T. Rie, T. Stucky, M. Hage-Ali, Cytocompatibility of Ti-6Al-4V and Ti-5Al-2.5Fe alloys according to three surface treatments, using human fibroblasts and osteoblasts, Biomaterials. 17 (1996) 929-940.

[8] T. Kokubo, H.M. Kim, M. Kawashita, T. Nakamura, Bioactive metals: preparation and properties, J. Mater. Sci. Mater. Med. 15 (2004) 99-107.

[9] C. Larsson, P. Thomsen, B.O. Aronsson, M. Rodahl, J. Lausmaa, B. Kasemo, L.E. Ericson, Bone response to surface-modified titanium implants: studies on the early tissue response to machined and electropolished implants with different oxide thicknesses, Biomaterials. 17 (1996) 605-616.

[10] H.M. Kim, F. Miyaji, T. Kokubo, T. Nakamura, Effect of heat treatment on apatite-forming ability of Ti metal induced by alkali treatment, J. Mater. Sci. Mater. Med. 8 (1997) 341-347.

[11] C. Yao, T.J. Webster, Anodization: a promising nano-modification technique of titanium implants for orthopedic applications, J. Nanosci Nanotechnol. 6 (2006) 2682-2692.

[12] N. Tran, T.J. Webster, Nanotechnology for bone materials, Wiley Interdiscip. Rev. Nanomed Nanobiotechnol. 1 (2009) 336-351.

[13] S. Bauer, J. Park, J. Faltenbacher, S. Berger, K. von der Mark, P. Schmuki, Size selective behavior of mesenchymal stem cells on ZrO_2 and TiO_2 nanotube arrays, Integr. Biol. (Camb). 1 (2009) 525-532.

[14] F. Variola, J.B. Brunski, G. Orsini, P. Tambasco de Oliveira, R. Wazen, A. Nanci, Nanoscale surface modifications of medically relevant metals: state-of-the art and perspectives, Nanoscale. (2010).

[15] A.V. Lombardi Jr, K.R. Berend, T.H. Mallory, Hydroxyapatite-coated titanium porous plasma spray tapered stem: experience at 15 to 18 years, Clin. Orthop. Relat. Res. 453 (2006) 81-85.

[16] R.J. Talib, M.R. Toff, Plasma-sprayed coating of hydroxyapatite on metal implants--a review, Med. J. Malaysia. Suppl B 59 (2004) 153-154.

[17] A. Kodama, S. Bauer, A. Komatsu, H. Asoh, S. Ono, P. Schmuki, Bioactivation of titanium surfaces using coatings of TiO_2 nanotubes rapidly pre-loaded with synthetic hydroxyapatite, Acta Biomater. 5 (2009) 2322-2330.

[18] Y. Tsutsumi, D. Nishimura, H. Doi, N. Nomura, T. Hanawa, Cathodic alkaline treatment of zirconium to give the ability to form calcium phosphate, Acta Biomater. 6 (2010) 4161-4166.

Chapter 2 Literature review

2.1 History of orthopedic replacements

For more than 180 years several means have been applied in surgical treatments for degenerating joints [1]. The methods on treatment have included early excision arthroplasty technology and interpositions arthroplasty technology, and more recently replacement arthroplasty. Until the 1940s, femoral head replacements using acrylic prostheses originally were developed by the Judet brothers in France [2]. In the 1950s, the first prostheses made from cobalt-chromium (CoCr) alloy were developed in parallel by Moore in the United States [3] and McKee in England [4]. However, in the early stages of these developments, it was reported that many patients suffered from a high incidence of fractures and severe abrasion of the acrylic, as well as the potential for migration of the acetabulum and penetration of the Co-Cr femoral head into the pelvis.

Total hip replacements were successfully applied until the metal-on-metal implants or metal on polymer were invented. Metal-on-metal prostheses were first introduced by McKee in 1957 with both the femoral and acetabular components being made of stainless steel [5]. During the treatment, the acetabular cup was fixed into the pelvis by means of screws. However, the contact between screws and major materials became loose due to excessive friction related to the stainless steel ball within a close-fitting acetabular cup. Subsequently, modifications were

implemented including the adoption of CoCrMo alloy and Ti-based alloy instead of stainless steel [6,7]. It was found that the success rate depended strongly on the tightness of the metallic components within the bone. In the late 1960s, a cement component was introduced to secure the components in place that improved the success rate to over 90%. Metal-on-polymer prostheses are outstanding success of modern replacement joint operations. This technique was attributed to John Charnley, who invented use of ultrahigh molecular weight polyethylene (UHMWPE) as the cup material, which remains the polymer most used in joint replacement prostheses [8].

2.2 Metallic materials for orthopedic prostheses

Common total joint replacement prostheses are shown in Figure 2-1 such as: (a) Charnley-Muller total hip replacement, (b) geometric total knee replacement, (c) Newton total ankle replacement, (d) Stanmore total shoulder replacement, (e) Felin total shoulder replacement, (f) Dee total elbow replacement, and (g) Meuli total wrist replacement [9].

A variety of failures have been observed in each kind of replacement shown in Figure 2-1 [9]. The durability of a total joint prosthesis depends on many factors. In the short term, it is closely related to the medical operation and tends to depend on biological factors. In particular, infection is a major cause of failure in the short term. Long term failures tend to be related to the materials' properties. Most of long

term failures are due to materials fracture, wear loss, and degradation.

Table 2-1 gives a summary of the general requirements for materials to be applied in artificial implants. A purpose of materials research in the biomedical field is to develop materials or modify existing materials to optimize these requirements, among which the biocompatibility of a material is the most important property. In this section, some conventional materials that can be used as implant materials are introduced briefly.

Table 2-1 Requirements for joint implant materials [6,10]

Properties	Requirements
Mechanical	High yield and fatigue strength; Elasticity modulus of bone interference; Wear resistance
Chemical and physical	Low corrosion rate Low susceptibility to crevice and pitting corrosion; Density approaching that of cortical bone; Low friction coefficient.
Biological	Not to induce inflammatory response; Absence of tumorgenicity; Not activate immune system; Available for regeneration of skeletal tissues.

Stainless steel (SS)

In the late 1950s, 316L type SS was introduced for use in biomedical

application due to its good corrosion resistance in saline water or chloride containing electrolytes [11]. In comparison with other alloys for implants, SS 316L has moderate yield and ultimate strength combined with high ductility and cost effectiveness, making it still a good choice in short term fracture fixation devices [12].

Co-based alloys

There are three kinds of Co-based alloys suitable for applications as implant materials (ASTM F1537, F562, and F563). F1537 is a commercial wrought alloy and the most commonly used alloy today in orthopedics. It was originally called Vitallium [13]. Other than F1537, F562 [14] and F563 [15] are commercial Co-based alloys containing additional Ni or Ni, W and Fe, which are occasionally used in Europe. When compared to stainless steel, Co-based alloys have slightly higher elastic moduli and much higher strengths, lower ductility and higher cost.

Ti-based alloys

Ti and Ti-based alloys are relatively new materials in the field of joint prosthesis. The first commercial Ti implant was introduced in 1965 [16,17]. Since it has low specific strength, less than SS and Co-based alloys and closer to that of bone, high strength and Ti is a less toxic element, they are important candidates for use as implant materials. Commercially pure (CP) titanium and Ti-6A1-4V alloy are the two most common titanium-based implant biomaterials.

Since some authors have reported that vanadium has potential toxicity to the human body, this has led to the development of V-free titanium implant alloys with

properties similar to Ti-6Al-4V during the last decade. It has been reported that alloys such as Ti-6Al-7Nb, Ti-8Ta-3Nb, Ti-10Ta-10Nb, Ti-Zr and Ti-xMo (x = 5-20), have been developed as alternative Ti-based implant materials. Although there have been numerous publications regarding the *in vitro* and *in vivo* behaviour of such alloys, there are few commercial products that have been approved for real application [18,19].

Zr and Zr-based alloy

Zr is characterized as one of refractory metals because of its relative chemical stability through formation of a passive oxide layer and high melting point. Because of the surface layer stability Zr is highly corrosion resistant. Corrosion resistance generally correlates with biocompatibility since more stable metal alloys tend to be less chemically active and have lower tendency to participate in biological reactions. The elastic modulus of Zr is closer to the human bone comparing with other metals, which makes less modulus mismatch to the bone. Additionally, Zr possesses a high level of hardness (about HRC67) and wear resistance, which is about 10 times that of Co alloys and Ti alloys, making it well suited for bearing surface applications [18]. Another advantage of Zr is a lower susceptibility to magnetic response than Ti alloys. These advantageous properties make it possible to use them in downsized, safe, and MRI-compatible devices in medicine [20]. Therefore, Zr is predicted to gain popularity as an orthopedic material in the immediate future. Another advantage for Zr as implant is that surface modification

can be carried out on Zr surface to form highly ordered ZrO_2 nanotubular arrays, which may highly enhance the biocompatibility, which will be summarized in later section. Thus, Zr has been taken into account as the primary candidate within the present research. A comparison of the mechanical properties of the above orthopedic alloys is shown in Table 2-2.

Table 2-2 Comparison of the mechanical properties of metal implant alloys [12,14,23,24]

Properties	SS 316L (F138)	CoCrMo (F1537)	Ti6Al4V (F136)	Zr	Human Bone
Elastic modulus (GPa)	193	258	105	99	4-30
Yield strength (MPa)	170	827	795	381	~150
Hardness (HRC)	17	43	36	67	<20
Specific tensile strength (kN·m/kg)	62.7	133.8	288	81	~100
Elongation (%)	28	20	10	18	~1.5
Magnetic susceptibility	High	High	Medium	low	N/A

2.3 Surface modification of metallic implants

The bone-implant interface plays a critical role in determining the performance of an implant. An immediate bone-implant contact after the surgery enhances osseointegration, leading to better mechanical stability and longer implant service life [21]. However, current prosthetic metals typically develop a thin fibrous layer

at the interface with bone. The fibrous layer is mechanically weak and susceptible to micromotion which results in premature loosening. In addition, the fibrous layer tends to prevent the implant from directly contacting with the bone, which is also detrimental to osseointegration [22]. One of challenges for use of implant materials is to enhance the process of osseointegration and to accelerate the implant fixation time, thus reducing the implant micro-motion and minimizing fibrous tissue formation at the bone-implant interface, as well as reducing the recipient's hospitalization time and cost, thereby improving the quality of life for patients. Therefore, during the past several decades, researchers have found that development of novel surfaces via modification to facilitate healing process is highly required [23].

2.3.1 Surface modification via calcium phosphate coating

Since healthy bone contains about 70 wt% carbonated apatite, which is chemically similar to hydroxyapatite (HA, $Ca_{10}(OH)_2(PO_4)_6$) [24], a layer of HA coating on metallic implant was considered to be a reasonable choice for enhancing the biocompatibility of implants with bone. HA coating is now extensively produced is because of their chemical similarities and bone may not recognize HA as foreign. As a result, the interface between implant and bone may heal faster and integrate bone with a HA-coated implant more firmly [25]. A number of techniques have been used for producing HA coatings on metallic implants [25,26]. Thermal spraying techniques, such as plasma spraying, have been applied for production of

HA coatings for many years [27,28]. More recently techniques such as physical vapour deposition (PVD) techniques, chemical vapour deposition (CVD), electrochemically assisted deposition (ECAD), and biomimetic deposition have been investigated [25,29]. In the following subsections, these techniques and their features will be reviewed briefly.

2.3.1.1 Thermal spraying HA coating

The thermal spraying technique is a coating process in which melted materials are sprayed onto the substrate. In the case of HA coating, HA powders are fed in powder or wire form, heated to a molten or semi-molten state and accelerated towards substrates in the form of micrometer-size particles. Thermal spraying can provide relatively thick coating ranging from several μm to several mm [30]. The history of thermal spraying dates back to the late 1800s [31]. There are now many different thermal spray processes. One successful process for the production of hydroxyapatite coatings is plasma spraying.

2.3.1.2 Plasma sprayed HA coating

Plasma spraying is currently the only FDA approved method for the production of HA coatings [32]. The first industrial plasma spray guns appeared in the 1960s [33]. Advances since then include changes in spray gun and spray nozzle design. High pressure plasma spray and vacuum plasma spray systems have also been introduced [34].

Positive results with plasma-sprayed HA coatings have been demonstrated in

clinics: a recent survey of 6,652 cases conducted in Norway shows that for patients younger than 60 years, 2% of HA coated hip stems failed after 10 years, whereas more than 25% of uncoated ones failed (e.g. with smooth and threaded surfaces) [35,36]. However, there is also detrimental effect of these coatings. The coatings obtained typically differ from the calcium phosphate powder input. At the plasma flame temperature (up to several thousand degrees centigrade), HA powders may decompose into other phases (e.g. calcium oxide, calcium pyrophosphate and tricalcium phosphates) [34,37,38]. Carbonate and hydroxyl groups in HA, both normal constituents in bone mineral, also may be destroyed. The fast cooling of partially melted powders creates a non-crystalline calcium phosphate phase [30]. Moreover, the plasma spray method can only be applied to areas that are in the direct line-of-sight. Therefore, it is difficult to uniformly coat implants having complex shapes and it is unfeasible to coat internal surfaces like the internal surface of porous bead coatings, which have been widely used in orthopedic and dental implants. In addition, plasma-sprayed coatings comprise fused grains tens of micrometers in size, a feature very different from bone minerals [39].

2.3.1.3 Physical vapour deposition (PVD) and chemical vapour deposition (CVD) technique

Many physical vapour deposition techniques have been developed in recent years to obtain calcium phosphate coatings. These include radio frequency magnetron sputtering [40], ion beam assisted deposition (IBAD) [41], ion beam

mixing (IBM) [42] and techniques that are based on plasma-assisted ion implantation such as plasma source ion implantation (PSII) and plasma immersion ion implantation (PIII) [43,44]. One disadvantage common to all physical vapour deposition techniques is that the deposition rate is very slow and, for this reason, these systems have been used very little in the preparation of calcium phosphate based coatings [43].

The typical HA coatings formed using PVD techniques are amorphous [45]. This is because the sputtered components (containing Ca, P, O and H) do not recombine to reform crystalline HA. It is possible to create coatings with excellent adherence and smoothness. However, as they are very thin, typically having a thickness of 638 nm according to Kim et al., their durability *in vivo* is questionable [46]. Variations in chemical composition of the coatings are brought about during the deposition process, such as distortion of the phosphate lattice, loss of hydroxyl groups, and the incorporation of CO_3^{2-} [43].

The chemical vapour deposition (CVD) process involves the nucleation and growth of a coating through chemical reactions involved in the gases immediately above the substrate. The process is carried out in a vacuum at high temperatures, usually about 1000°C. The rate of coating deposition can be maintained by controlling the chemical potential (concentration) of reaction gases. Generally, the rate of deposition and the temperature of deposition determine the reaction kinetics and rates at which the products can crystallize and deposit on the reaction surface

[47].

2.3.1.4 Electrochemically-assisted deposition

Electrochemically-assisted deposition (ECAD) of calcium phosphates (CaP, such as hydroxyapatite (HA), octacalcium phosphate (OCP), and $CaHPO_4$, etc.) coating is a non-line-of-sight, aqueous and low temperature coating method [48]. It is a process using electrochemically conductive substrates in a Ca^{2+} and phosphate-containing electrolyte. The process is based on several electrode reactions and induced pH jump effect adjacent to the cathode [39,48]:

$$2H^+ + 2e \rightarrow H_2 \uparrow \text{ (discharge of proton)} \quad (2.1)$$

$$2H_2O + 2e \rightarrow 2\,OH^- + H_2 \uparrow \text{ (reduction of molecular water)} \quad (2.2)$$

$$O_2\,(aq) + 2H_2O + 4e \rightarrow 4\,OH^- \text{ (reduction of dissolved oxygen)} \quad (2.3)$$

All these reactions can cause a local increase in pH at the substrate surface. In an electrolyte containing Ca^{2+} and phosphate species, the local pH increase drives hydrogen phosphate anions to dissociate. As the solubility of CaP is pH-dependent, when the pH reaches a critical point the rise in pH results in formation of crystallites of CaP and formation of a coating. Coatings obtained using ECAD can be carried out under potentiostatic, galvanostatic, and constant voltage modes depending on the cell setup. The variation of ECAD parameters, such as ion concentration, current density, temperature, affects the deposition phase and morphology [25].

Redepenning et al. first obtained brushite coating on 316L SS in an acidic (pH =

3.5) saturated $Ca(H_2PO_4)_2$ electrolyte [49]. The coating contained flake-like crystals having lengths of several tens of μm. In order to make the coating more biocompatible post-treatment, such as immersion in NaOH or buffered phosphate saline solution, was required to convert the brushite to HA. In order to obtain other CaP such as octacalcium phosphate (OCP) or HA coating, a mildly acidic or neutral pH electrolyte with low concentration of Ca^{2+} and PO_4^{3-} is required. The coatings contain crystals with dimensions ranging from several tens of nanometers to several μm size [50].

Until the present there have been thousands of publications describing the deposition of CaP coating by ECAD (based on ISI web of Science since 1994). Among these, two groups of researchers (Ban et al. and Röβler et al.) detailed the effect of current density, deposition duration, temperature, and electrolyte composition on the growth kinetics and composition of ECAD-formed CaP, especially OCP and HA coatings on metallic implant. Both of them found that the electrolyte and conditions should contain Ca^{2+} from 1.67-2.5 mM and PO_4^{3-} from 1-1.67 mM and pH between 6.4 and 7.2. The current density varied from 1.3 mA/cm^2 to 12.9 mA/cm^2 with temperature from room temperature (25 ^oC) up to 200 ^oC. A lower current density resulted in more OCP than HA in the coating. Enhancing the current density and temperature more readily induced HA coating. The duration of deposition always lasted for 30 min and prolonging the duration did not change the deposited phase but only the deposition thickness [50-55]. Most of

other groups followed these two groups' work and developed coatings by changing the ratio of Ca and P composition or different combinations of deposition parameters [56].

ECAD is also applied for electrochemical codeposition of HA composite coatings. Wang et al. obtained HA-collagen composite coatings via this technique. The aim was to obtain a coating more bone-like than pure HA and with better biocompatibility [57]. Following their work, successful cases including codeposition of HA-chitosan coating and OCP-collagen coating have been reported [58]. There has also been reported codeposition of HA-protein coating [59]. It is predicted that such coatings might offer improved healing chances for patients with systemic diseases such as osteoporosis and diabetes [57].

Electrophoretic deposition (EPD) is another approach for generating CaP coating using a setup and an electrical field similar to those for ECAD [60,61]. EPD is also taken into account as an alternative to ECAD. In EPD processes, CaP suspension is present in the electrolyte. The positively charged CaP particles move to the substrate surface in an electrical field. The 'current efficiency' of EPD is much higher than that of ECAD. The deposition rate is proportional to the strength of the electric field; fields in the range of 10 V/cm are commonly applied for deposition HA coating [60,62]. Typical EPD processing times to deposit layers with coating weights in the range of about 10 mg/cm^2 are less than 1 min [63]. Because of the nature of the deposition process the initial adherence of the coatings is poor.

For this reason the deposition is followed in all cases by thermal treatment (mostly in vacuum), typically at 800 ^{o}C to 1200 ^{o}C for at least 1 h [63]. Because of the nature of the method the lowest possible layer thickness is determined by the average diameter of particles suspended in the electrolyte. When particle diameters generally are in the micrometer range coatings produced by EPD commonly have a thickness of 10 to 1000 μm [61]. Preparation of composite coatings such as HA-Ag-chitosan and HA-$CaSiO_3$-chitosan coating using a EPD approach has also been reported [64].

2.3.1.5 Biomimetic deposition

Biomimetic deposition is based on heterogeneous nucleation onto biomedical materials. It is a technique that requires rigorously controlled solution conditions and temperatures to induce the deposition nucleation on the substrate materials. The term 'biomimetic' is from the strategy that it widely used by living organisms to form hard tissues: the organic matrices use anionic groups (e.g. carboxyl groups $-COO^-$) at the surface to nucleate biominerals in a well controlled manner. The electrostatic attraction between surface anions and Ca^{2+} is the key step for nucleation [39].

An example of biomimetic deposition of HA coating onto commercial titanium implants has been reported by Kim et al. [65]. As described in their study, Ti and its alloys were immersed in 10 M NaOH at 60 ^{o}C for 24 h and then heat-treated at 600 ^{o}C. The reaction between Ti and NaOH transformed the surfaces into a mesh-like

sodium titanate with sub-micrometer pores. After soaking for 4 weeks in simulated biological fluid (SBF) a continuous coating of nano sized HA crystallites was formed. A similar result was also reported by same group for deposition onto Ta implants [66]. The mechanism can be summarized as: Na^+-H^+ exchange increases the local pH and saturation of OH^-, then Ti-OH or Ta-OH act as nucleation sites for development of apatite. Kim et al. also showed that this method was appropriate on Ti and Ta but not for deposition onto CoCrMo or 316L SS [67]. Many researchers adopted this method during the last decade. For example, Wei et al. found out that Ti alloys after 3 days soaking in 5M NaOH following by heat treatment at 600℃ for 1h could form uniform HA coating by immersion in SBF for 1 week [68]. Wen et al. used an acid-base two step etching and a more highly supersaturated solution (accelerated calcified solution) to prepare HA coatings within 1 day [69,70]. Because the simulate the natural process for the formation of the CaP coating it is widely believed that the biomimetic deposition process for CaP coating is the most appropriate for *in vivo* application for metallic implants [71-73].

2.3.1.6 Effective dipping treatments to induce HA coating

Other than the alkaline and post heat treatment, there have been reports by applying simple dipping treatments to induce calcium phosphorous species on metallic implant to enhance the HA coating formation in SBF.

An effective dipping method was developed to form insoluble crystalline calcium phosphate (CaP) on bulk metal substrate and porous metallic implants

[74][75]. This method is summarized as follows: dipping and withdrawing of a sample from a saturated calcium solution; allowing the sample to dry totally in air; repeating the dipping; withdrawing, and drying process. Following the repeated dipping and withdrawing steps, the CaP crystallites attached to the metallic substrate during the drying process as the liquid evaporated. Once the treated materials were immersed in the simulated biological fluid (SBF), these CaP crystallites were nucleation centers which served as precursors for subsequent rapid formation of HA.

An alternative immersion method (AIM) was recently reported for synthesizing HA coating on porous metal in order to enhance the bioactivity of the metal surfaces, such as porous Al and TiO_2 nanotubes [76-78]. Briefly, the AIM contained several repeated procedures by immersing the porous metal in saturated $Ca(OH)_2$ and consequently $(NH_4)_2HPO_4$ solutions. It was reported that on the metal with meso-pores, such as Al, and Mg or nanotubular structure, such as Ti, the AIM was highly efficient for the deposition of synthesized HA. The formation rate of HA coating on AIM-treated metals can be enhanced more than several fold [77].

2.4 Anodization modification of porous oxide layers

Electrochemical anodization typically is carried out in an electrochemical cell which usually has a two-electrode or three-electrode configuration [79]. For a two-electrode setup the anode is metal, such as titanium and zirconium, while the

cathode is platinum. A reference electrode is included in a three-electrode setup. When a constant voltage or current is applied between the anode and cathode electrode reactions (oxidation and reduction) a combination of field-driven ion diffusions lead to the formation of an oxide layer on the anode surface [80,81].

The main electrochemical reactions specifically for anodizing of metal are listed below. At the metal/metal oxide interface [80]:

$$M \leftrightarrow M^{n+} + ne^- \quad (2.4)$$

At the metal oxide/electrolyte interfaces:

$$n/2H_2O \leftrightarrow n/2O^{2-} + nH^+ \quad (2.5)$$

$$n/2H_2O \leftrightarrow n/4O_2 + nH^+ + ne^- \quad (2.6)$$

At both interfaces:

$$M^{n+} + n/2O^{2-} \leftrightarrow MO_{n/2} + ne^- \quad (2.7)$$

Because metal oxides have higher resistivity than both the electrolyte and the metallic substrate the applied voltage will drop over the oxide film on the anode. The oxide film will keep growing only as long as the electrical field is strong enough to drive ion conduction through the oxide. It has been reported that thickness of anodized titanium dioxide film, d, is almost linearly dependent on the applied voltage, U:

$$d \approx kU \quad (2.8)$$

where k is a constant for anodic titanium dioxide depending on the anodization culture [82].

The anodic oxide film properties such as surface roughness, microscale/nanoscale morphology, and chemistry vary over a wide range depending on process parameters including applied potential, electrical field, electrolyte, and physical conditions (pH and temperature) [83,84]. Commonly anodization can be carried out in different acids (phosphoric acid, H_3PO_4, sulfuric acid, H_2SO_4, acetic acid, etc) [85-87], neutral salts solution, and alkaline solutions. Usually, H_3PO_4 and H_2SO_4 have been used to develop thick and micro-porous oxide layers with tens of μm at high voltage (over 50 V) [84]. On the other hand, fluoride solutions were found to have the ability of producing biologically-inspired nanotubular structures in the past few years [82,88,89].

2.4.1 Micro-porous oxide films

During the electrochemical process, micro-porous metal oxide films form at an applied voltage exceeding the dielectric breakdown limit of the oxide, which will no longer be sufficiently resistive to prevent further current flow and oxide growth. The electrochemical technique applied for formation of micro-porous film is also called anodized spark deposition (ASD) or micro-arc oxidation (MAO) [90]. It has been reported that the breakdown potentials of TiO_2 film in H_3PO_4 and H_2SO_4 were around 80 and 100 V, respectively [91-93].

The mechanism of the ASD or MAO is usually described by a so-called avalanche theory [94,95]. At the onset of anodization an oxide layer is formed on the anode. During the anodization, the newly-formed oxide layer acts as a dielectric

barrier to the current flow and keeps growing until reaching the dielectric breakdown limit. Since the anodized layer is not uniform owing to the existence of flaws, defects, local stress, and non-uniform oxide thickness, the potential drop at these weak points exceeds the dielectric limit while the applied voltage increases. As a result, sparking happens at the weak points. The local temperature at these points can be up to several thousand Kelvin. The increasing temperature leads to a local melting process and results in a transformation of amorphous oxide to dense oxide phase. The thermal stressing due to the formation of dense crystallites consequently induces the multiplication of weak points, where the breakdown of the barrier oxide film occurs and pores are formed. Moreover, the areas of breakdown of the oxide are immediately covered with metal oxide again due to the repassivation characteristics of these metals. When the breakdown occurs again inside the repassivated pores, small pores are formed during an alternative breakdown and repassivation process. In this manner the porous oxide films are formed [91,95,96].

The micro-porous oxide layer has been shown to be more biocompatible than intact metal through *in vitro* and *in vivo* tests. The micro-porous titanium dioxide layer is more biocompatible than intact Ti [97]. Ishizawa et al. reported an anodization process of titanium in electrolytes containing Ca and phosphate species. Both Ca and P were embedded in the oxide layer. After an additional hydrothermal treatment, columnar or needle-like HA crystals were precipitated randomly on the

anodic oxide film [98,99]. In order to obtain a uniformly distributed HA coating several approaches have been reported showing that higher voltage (> 100 V) is required to obtain a crystalline TiO_2 layer [93]. The resulting oxide layer is composed mainly of an anatase phase and is able to induce HA formation by simply soaking the specimen in simulated biological fluid. Wei et al. reported that a uniform HA coating was induced on anodic TiO_2 layers, which was obtained by anodization in 1 M H_2SO_4 at 150 V in SBF for 6 days [100]. Alternatively, anodization in alkaline electrolyte formed a biocompatible titanium dioxide layer. Xie et al. reported anodization of Ti and Ti6Al4V in a very highly concentrated NaOH electrolyte to obtain a micro-porous oxide layer. The oxide layer was amorphous with some remaining Na^+ species inside the pores, resulting in an alkali surface. Consequently, the HA coating grew on the treated specimen in an accelerated calcium solution [101,102].

In vitro cytocompatibility tests also have been conducted on anodized titanium with micro-porous oxide film. Fini et al. compared the adhesion, proliferation, and differentiation behaviour of HOS-TE85, which is an osteoblast-like cell, on four kinds of specimen: unanodized titanium, anodized titanium enriched with Ca, anodized titanium enriched with P and anodized titanium followed by hydrothermal treatment. Their results indicated that the cytotoxicity of the four kinds of specimen were quite similar. Among them, the anodized titanium followed by hydrothermal treatment showed better osteoconductive capability. However, the anodized

titanium did not show good bone apposition possibly owing to the degradation of amorphous TiO_2 [103]. Suh et al. and Zhu et al. reported that anodized titanium formed in electrolyte containing Ca enhanced the osteocalcin production and MG63 cell attachment and proliferation. The cells on the surface with micro-pores showed an irregular and polygonal growth and more lamellipodia while cells on the unanodized titanium showed many thick stress fibers and intense focal contacts [104-106]. Li et al. reported a threshold of the anodization voltage on titanium. Their results showed a decreasing of proliferation of MG63 cell on anodized titanium when the anodization voltage increased above 190 V [107].

A number of *in vivo* studies were carried out on porous oxide film to investigate the new bone growth. It was shown that TiO_2 porous film with thickness less than 200 nm and anodized in acetic acid had no significant difference when compared to unanodized samples after implantation in a rabbit for 6 weeks [108]. In contrast, anodization in H_3PO_4/H_2SO_4 electrolyte was applied to obtain thick porous film up to tens of microns. Obvious enhancement of bone bonding on these thick films was found in rabbit cases [109]. In addition, Giavaresi et al. supported the concept that hydrothermal treated anodized titanium with HA production had a positive role in accelerating bone growth and mineralization [110].

2.4.2 Anodization of self-assembled nanoporous and nanotubular structure

During the last decade researches have focused on creating biological mimic nanostructures by anodization of valve metals and their alloys. In 1999, Zwilling et

al. first reported the formation of self-ordered titanium dioxide nanoporous structures on titanium and Ti6Al4V in fluoride containing electrolyte at low applied voltage (<10 V) [111,112]. Shortly after Zwilling et al.'s reports, Grimes and co-workers first successfully fabricated the self-ordered titanium dioxide nanotubular structure in dilute (0.5-1.5 wt %) HF electrolyte via anodization between 10 – 40 V [113]. They obtained nanotubular arrays with diameter of 60 nm and layer thickness of 200 nm in 0.5 wt % HF under 20 V for 20 min anodization. They also showed that the diameters of nanotubes were determined by the applied voltage and that the final thicknesses of the nanotubular layers were independent of the anodization time [114]. Since then, the formation of such nanotubular structure has been reported on Ti [115], Zr [116], Hf [117], Ta [118], W [119], Nb [120], and their alloys, such as TiNb, TiAl, and TiZr [121,122]. The progressively increasing research interest in the anodic metal oxide nanotubular structure, mainly TiO_2, is evidenced by the statistics for publications from 1999 to 2010. There are more than 3000 publications have been output for the attractive field since the first report by Zwilling et al. Among these publications, there have been more than 2800 publications regarding the TiO_2 nanotubular arrays while only a very small section focuses on other valve metals. Meanwhile, by controlling the electrochemical anodization parameters of metals (temperature, potential ramping speed, applied potential, electrolyte species, electrolyte pH, viscosity, aqueous or organic electrolyte, etc.), one can obtain oxide nanotubular structures with thickness of

several nanometers to several hundreds of micrometers, and the pore diameter can be varied from several nanometers to several hundreds nanometers [123-131].

2.4.2.1 Mechanisms of anodic self-assembled nanotubular structures

Although the mechanism of the formation of self-assembled nanotubular structures is still being debated among researchers, a phenomenological mechanism has been accepted by most [115,132,133]. This section will summarize the current state of the knowledge of the formation of titanium dioxide nanotube layers during anodization and the formation of nanotubular structures. Figure 2-2 is a schematic diagram of the formation of straight nanotubes at a constant anodization voltage [134,135].

The first step of the formation of anodic self-assembled nanotubular structures is similar to that for microporous structures (Figure 2-2(a)). At the onset of electrochemical anodization a thick oxide layer is formed. For most valve metals in most electrolytes anodization leads to a uniform oxide layer, which is a compact layer on the microscopic level. Using the example of Ti, there are two processes to be considered:

(1) Ti^{0} is oxidized to Ti^{4+} at the metal-oxide interface and the Ti^{4+} ions migrate (under the electric field) and,

(2) O^{2-} ions are incorporated in the film and migrate towards the metal-oxide interface.

This process is also generally agreed as the active dissolution of Ti metal to form a

passive layer of TiO_2:

$$Ti + 2H_2O \rightarrow TiO_2 + 4H^+ + 4e^- \quad (2.8)$$

In the absence of F^- the growth of the oxide is self-limiting and eventually the thickness stabilizes at a constant value. Similar to formation of a microporous layer, the final thickness of oxide layer is directly related to the external potential for different electrolyte cultures.

The second stage is the formation of nanopores (Figure 2-2 (b)). The existence of F^- is a key factor for the chemical dissolution of TiO_2 to form soluble TiF_6^{2-} ions:

$$TiO_2 + 4H^+ + 6F^- \rightarrow [TiF_6]^{2-} + 2H_2O \quad (2.9)$$

Since the distribution of the electrical field in the oxide is strongly correlated with the surface morphological fluctuations, more pronounced fluctuations lead to more locally focused electrical field. As a result, localized dissolution at these spots takes place as described in (2.9) and the nanopores start to form. Nanopore formation results in the reduction of local oxide film thickness and increases the electrical field intensity at the bottom of the pores. The increased electrical field intensity drives the formation of new oxide at the metal/oxide interface while also increasing the rate of chemical dissolution at the oxide electrolyte interface.

The third stage is the transition from nanopores to nanotubular structure (Figure 2-2 (c)). Based on results from Mor et al. [115], it is suggested that the unanodized regions between pores are susceptible to electrical field-assisted oxidation/dissolution causing the formation of gaps between nanopore regions. As

the pores become deeper, the electric field in these protruded metallic regions increases, enhancing the field-assisted oxide growth and oxide dissolution, and simultaneously with the pores the well-defined interpore voids start forming.

The fourth stage is the formation of final nanotubular arrays (Figure 2-2 (d)). With the continued anodization, the nanotubular arrays continue to grow in length and the interpore grows until an equilibrium state of chemical dissolution and electrochemical oxidation is reached. At this stage the rate of chemical dissolution at the top of tubes is equal to the rate of oxide formation at the bottom of the tube.

2.4.2.2 Geometry and structure of the anodic metal oxide nanotubular arrays

The geometrical factors, such as nanotubular diameter and nanotubular array thickness, generally are reported to be linearly dependant to applied voltage during growth [88]. Typically, the TiO_2 nanotubular arrays have been reported with layer thickness from 10 nm to several tens of μm under the applied voltage from 1 V – 40 V in aqueous electrolyte [136-138]. Higher length TiO_2 nanotubular arrays with more than hundreds microns can be obtained in viscous electrolyte or higher voltage. Schmuki and his co-workers anodized Ti at 120 V in 0.2 M HF with 15 mins anodization time. Their results showed that anodic TiO_2 nanotubular arrays could be obtained more than 250 μm thick, which resulted in the nanotubular arrays with aspect-ratios over 300, [139]. Shortly thereafter, Grimes and his co-workers reported TiO_2 nanotubular arrays with more than 1 mm thickness and aspect-ratio about 10,000, which is the highest aspect ratio for anodic valve metallic oxide

nanotubular arrays reported up to now [131]. In cases of other metals or alloys most researches have reported nanotubular arrays thicknesses of several μm. The top morphology can be also tailored to form a high uniform geometry. By optimizing the anodization conditions, a hexagonal distribution of the nanotubular structure forms on TiO_2, ZrO_2, and TiTa alloys in non-aqueous electrolyte [130,134,140-145].

Some advanced geometries such as nanobamboo, nanolace, branched nanotube, and double walled nanotubes also have been reported to form on Ti and its alloys by amending the voltage during growth or by using several separate anodization steps. Moreover, there are also reports describing formation of interpore nanotubes and multiple layer nanotubular arrays on Ti [89,134,138,143,146,147].

The as-formed anodic valve metal oxide nanotubular layers typically have amorphous structures [136,143,148-150]. Figure 2-3 shows a typical HRTEM image and diffraction pattern of anodic ZrO_2 nanotubular arrays, which clearly demonstrates the amorphous nature. Some results indicate that for nanotubular arrays formed under certain conditions, typically at comparably high voltage and temperature, some nanocrystallites may be presented such as rutile phase of TiO_2 nanotubular arrays. Until now, in order to obtain crystalline nanotubular arrays thermal treatment above 300 ^oC was required to transform amorphous oxides to crystalline. For instance, thermal treatment above 450 ^oC is needed to convert amorphous TiO_2 into anatase or a mixture of anatase and rutile [125,151]. Pure

rutile nanotubular arrays never have been successfully obtained until now because there is significant morphological deterioration [127]. It has been reported that ZrO_2 nanotubular arrays transform from amorphous to tetragonal when the temperature is higher than 400 ^oC. It can be converted further to monoclinic phase at 700 ^oC [152,153].

2.4.2.3 Biomedical application of anodic oxide nanotubular arrays

Most of valve metals have been shown potential utility in biomedical applications. Among them, titanium and its alloys have been widely used in biomedical applications. Additionally, there have been reports of zirconium and tantalum biomedical implant products for orthopaedic and orthodontic applications [18,154,155]. It is therefore of interest to study valve metal oxide nanotubular surfaces in view of their biomedical effects [156].

One of the key features of metallic implant interacting with body fluids is that it induces hydroxyapatite (HA) growth [157]. Recent studies indicate that hydroxyapatite growth on TiO_2 nanotubular arrays can be enhanced, resulting in a faster and denser HA precipitation than that observed for compact TiO_2 oxide films and commercial Ti [158,159]. Moreover, several researches showed that a crystalline form of TiO_2 is an important factor for HA formation. Schmuki and co-workers suggested that a combination of anatase and rutile TiO_2 nanotubular arrays strongly enhanced the growth process of HA in simulated biological fluid within two weeks [158,160,161]. As the nanotube formation is also possible on

implant alloys such as Ti6Al4V or Ti6Al7Nb, the findings of the enhanced apatite formation on nanotubular surfaces are important [162]. Feng et al. and Liu et al. observed that anatase TiO_2 was able to induce HA precipitation with 10 μm thickness within 14 days. However, they applied SBF with higher concentrations of Ca and P species than existing *in vivo* environments [163]. A challenge still remains on the formation of HA coating on amorphous TiO_2 nanotubular arrays since it takes longer time than annealing the specimen (normally more than 20 days) [160]. Another example is that 28 days of immersion in SBF are required to form HA precipitation on ZrO_2 nanotubular arrays [164].

Since a significant time still is required to obtain the HA precipitation on nanotubular arrays, surface modifications of nanotubular arrays have been introduced. Jin and his co-workers first applied alkaline treatment, as described in section 2.3.1.5, on TiO_2 nanotubular arrays to form nanotubular arrays with top portions of Na_2TiO_3. EDX-detectable HA coating was observed after immersion of SBF for 1 day [137]. Liu et al. reported similar alkaline treatment on TiO_2 nanotubular arrays. Their results suggested that the alkaline treatment allows the TiO_2 nanotubular arrays to quickly react with NaOH and totally form Na_2TiO_3 after 30 min treatment. Thus, the formation of TiO_2 nanotubular arrays accelerates the process of pretreatment for HA coating formation comparing with intact Ti. However, it is a crucial aspect of their report that the primary structure of the nanotube layer could be destroyed in high concentration alkali and at high

temperature over a long time [165]. So it is difficult to confirm the role of the nanotube feature in HA deposition. Electrochemical deposition was also applied to generate HA coating on TiO_2 nanotubular arrays. Kar et al. applied a pulsed voltage technique to deposit HA using low voltage at room temperature. The HA nanorods so formed were deposited right from the bottom surface of nanotubes [166-168].

A more spectacular aspect is the cytocompatibility of the nanotubular structures. Some studies have been carried out on the interaction of living cells with nanotubular arrays. Schmuki and his co-workers studied the effect of TiO_2 nanotubular diameter on the adhesion, spreading and growth of mesenchymal stem cells [169-172]. Their results suggested that the vitality of the cells was significantly increased for nanotubes with diameters of approximate 15 nm when compared with flat TiO_2 surfaces. A strong decay in cell activity was observed for diameters about 50 nm. Once the diameter reaches about 100 nm it led to apoptosis, which was the programmed cell death [170,173]. More recently, the same group also observed similar cell behaviors on TiO_2 nanotubular arrays with different diameters such as 15 nm, 50 nm, and 100 nm [171]. Some surface chemistry modifications have been introduced on adjust the TiO_2 nanotubular arrays from superhydrophilic to superhydrophobic by organic monolayer (SAM) attachment since the adhesion and proliferation of cells as well as adsorption of extracellular matrix proteins can be strongly influenced by the control of the wettability properties of the nanotubular layers [172,174,174-176].

Although there are only a few *in vivo* studies of nanotubular arrays until now, it can be implied from studies carried out in simulated biological environment and *in vitro* that the valve metallic oxide nanotubular arrays are highly promising surface for implant in desired manner [177].

2.4.2.4 Anodic ZrO_2 nanotubular arrays

In most recent two years, highly ordered ZrO_2 nanotubular arrays with high aspect ratio have been paid significant attention to due to their existing and potential applications, such as host matrix for optical application, components for oxygen sensor, electrolyte in solid-oxide fuel cell [178-184]. The ZrO_2 nanotubular arrays have also been suggested having potential in biomedical application since they can possess an empty volume for filling with bioactive species and provide an interface suitable for anchoring connective tissue [164]. It is also predicted that the nanotubular structure has potential to contribute on local delivery of antibiotics off-implant at the site of implantation and the control of hemorrhage by forming significant strong clots at reduced clotting times [171]. One of the most important properties of materials in biomedical application is the mechanical property, which may be crucial for the materials as long-term in vivo implants [185,186]. The mismatching of the mechanical properties, such as elastic modulus, between bone and the implant surface layer, may result in bone resorption, therefore causing implant loosening and eventual failure. To our best knowledge, there is no mechanical evaluation of ZrO_2 nanotubular arrays being reported. Thus, it is

important to characterize the mechanical behavior of these implant materials. Furthermore, it is important to establish the relationship between microstructure and mechanical behavior, in an effort to elucidate deformation mechanisms [187].

Another aspect is to efficiently generate HA coating on ZrO_2 nanotubular arrays. There has been reported that HA coating were induced on ZrO_2 nanotubular arrays within 4 weeks immersion in SBF and the resulting coating was less then 1 μm thick. Guo et al. modified the ZrO_2 nanotubular arrays by annealing the samples to 200 – 400 ^oC and obtained the HA coating within 14 days immersion in SBF. The as-formed coating was still as thin as 1 μm [152,164].

2.5 Summary of present status of surface modification on metallic implants and topic selection

The above review on the status of research of surface modification of metallic biomedical materials mainly includes the wet chemistry approach and the electrochemical anodization technique. Considerable progress has been achieved in formation of uniform calcium phosphate coating (HA and OCP) via biomimetic processes on metallic implants and calcium phosphate-organic species composites coating via electrodeposition or electrophoretic deposition. Attempts have been made to develop anodic oxide nanotubular arrays with optimum structure to deposit calcium phosphate coating and enhance their biocompatibility. Moreover, since anodic oxide nanotubular arrays are a relatively new concept, further extensive and

intensive work can be carried out to understand their mechanical properties and to explore the technique with the objective of accelerating the wet chemistry process to modify the nanotubular structure [89].

Considering the potential biomedical applications of Zr with anodic ZrO_2 nanotubular arrays, the present work focuses on fabrication of anodic ZrO_2 nanotubular arrays and examines their mechanical properties. Meanwhile, several wet chemistry modifications have been explored to efficiently generate bioactive HA coating on nanotubular structures from the *in vitro* simulated biological environment. These techniques offer good prospects for acceleration of the interaction between the implant and surrounding tissues during the implantation [75,78,149]. The results obtained have been grouped and introduced in the chapters as listed below.

Chapter 3: Experimental methods and materials characterization. This chapter summarizes the technique for ZrO_2 nanotubular arrays fabrication and materials characterization techniques applied in this thesis.

Chapter 4: Fabrication and mechanical properties of anodic ZrO_2 nanotubular arrays. This chapter investigates the growth and geometry of ZrO_2 nanotubular arrays by varying the anodization parameters such as time and anodization voltage. The mechanical and wear properties have also been observed.

Chapter 5: Enhancement of the capability of hydroxyapatite formation on anodic oxide nanotubular arrays via an effective dipping pretreatment. In this

chapter, an effective wet chemical pretreatment has been introduced to induce amorphous calcium phosphate on anodic oxide nanotubular arrays. This pretreatment has shown to highly enhance the formation of hydroxyapatite (HA) coating on TiO_2 and ZrO_2 nanotubular arrays. HA deposition appears shortly after only 12 hrs immersion in SBF.

Chapter 6: Fabrication and formation of bioactive zirconium using coatings containing anodized zirconium oxide nanotubes with preloaded hydroxyapatite. This chapter presents an effective approach to obtain bioactive zirconium implant by applying presynthesized hydroxyapatite on ZrO_2 nanotubular arrays via chemical reaction in $Ca(OH)_2$ and $(NH_4)_2HPO_4$. The surface quickly induces the HA formation by immersion in SBF.

Chapter 7: Enhancing the bioactivity of zirconium with the coating of anodized ZrO_2 nanotubular arrays prepared in phosphate containing electrolyte. This chapter provides a new route to form bioactive Zr with anodic ZrO_2 nanotubular arrays. Anodization in phosphorous containing electrolyte allows phosphorous adsorbing on the nanotubular arrays. By immersion in SBF, the phosphorous ions attract Ca^{2+} to form precipitation and result in HA coating.

Chapter 8: General conclusions and future recommendations.

Appendix I: Formation of Hydroxyapatite Coating on Anodic Titanium Dioxide Nanotubes via an Efficient Dipping Treatment. In this appendix, the effective dipping treatment, which has been discussed in chapter 5, has been

applied on anodic TiO_2 nanotubular arrays. The possible mechanism of the dipping treatment and the bonding strength of HA also discussed.

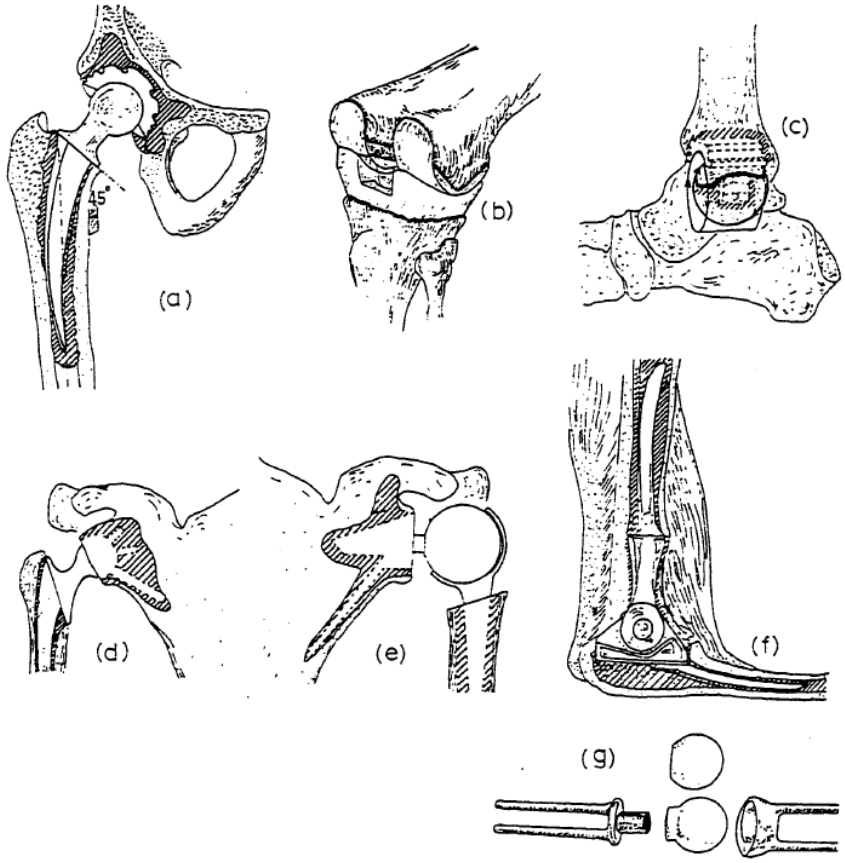

Figure 2-1 Total joint replacement arthroplasty: (a) Charnley-Muller total hip replacement; (b) geometric total knee replacement; (c) Newton total ankle replacement; (d) Stanmore total shoulder replacement; (e) Fenlin total shoulder replacement; (f) Dee total elbow replacement; (g) Meuli total wrist replacement (adapted from [9]).

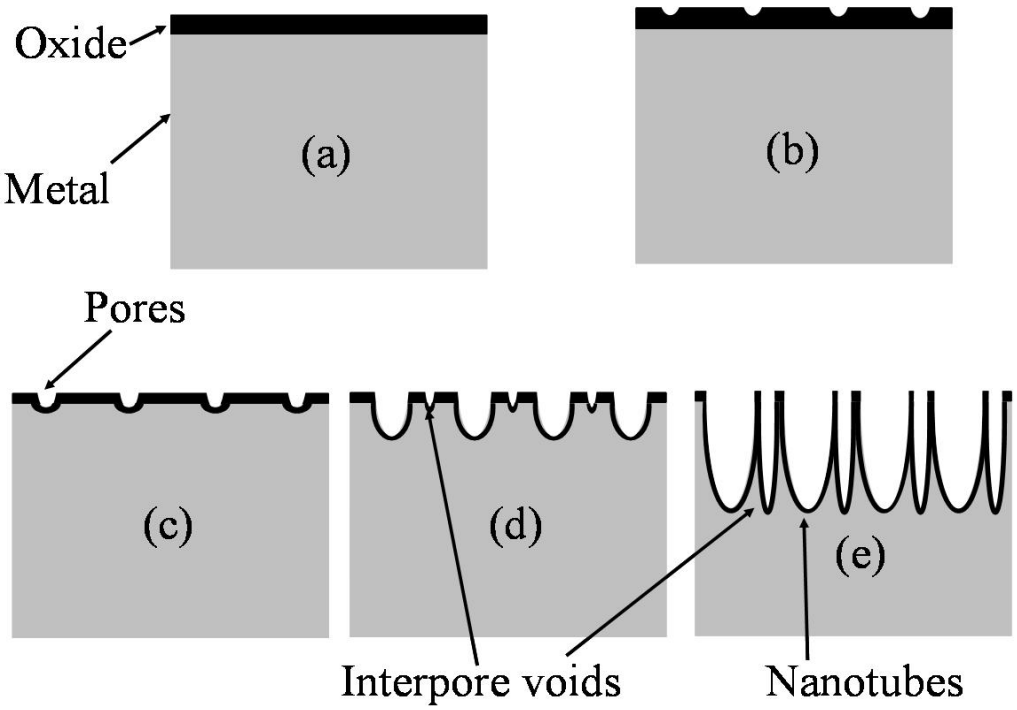

Figure 2-2 Schematic diagram of the evolution of straight nanotubes at a constant anodization voltage, as follows: (a) oxide layer formation; (b) pit formation on the oxide layer; (c) growth of the pit into scallop-shaped pores; (d) the metallic part between the pores undergoes oxidation and field-assisted dissolution; and (e) fully developed nanotubes (Adapted from [93, 119]).

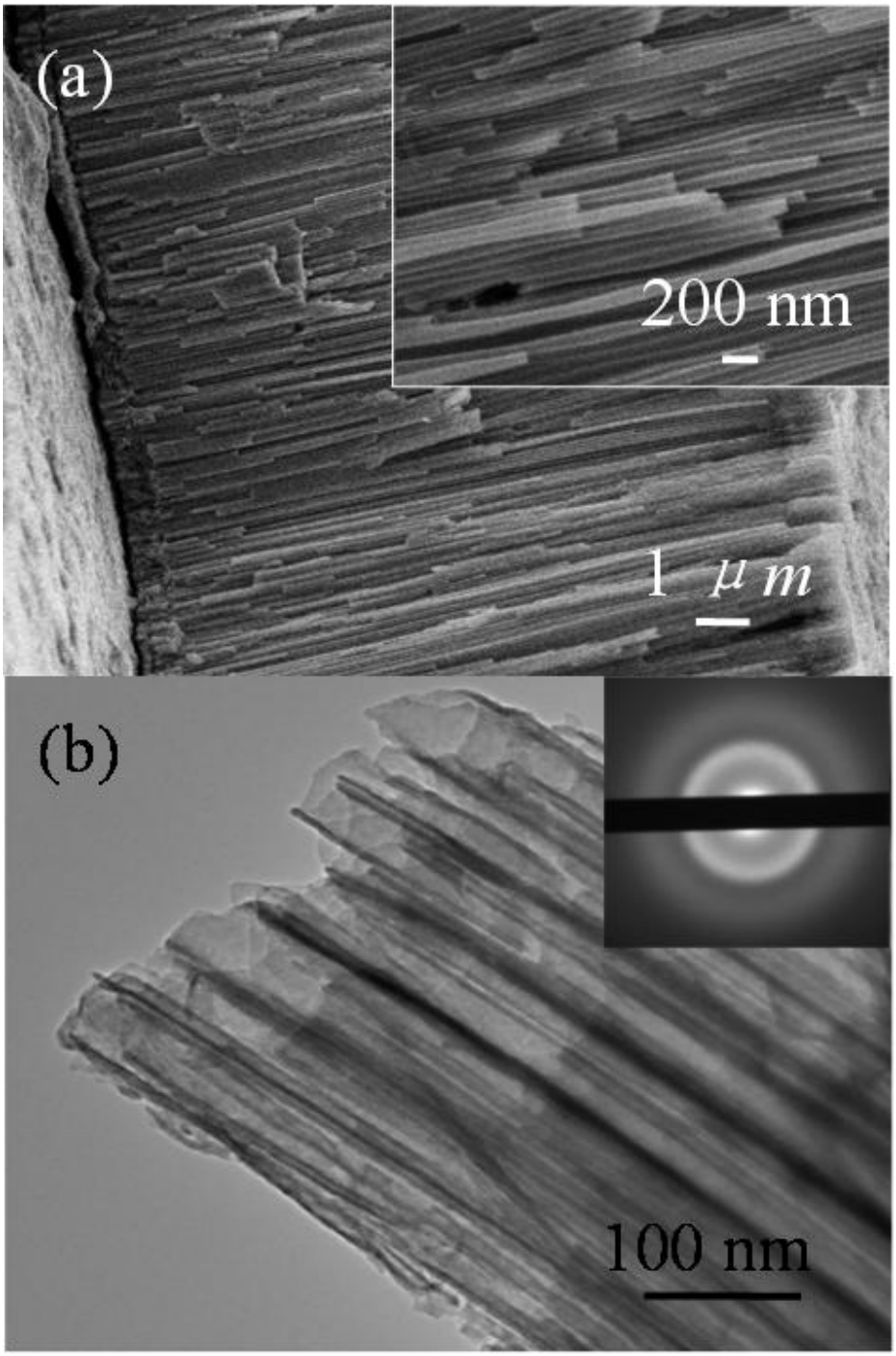

Figure 2-3 (a) SEM image of cross section and (b) HRTEM image and diffraction pattern of ZrO_2 nanotubular arrays (Adapted from [149]).

References

[1] K.J. Hamelynck, The history of mobile-bearing total knee replacement systems, Orthopedics. 29 (2006) S7-12.

[2] J. JUDET, R. JUDET, The use of an artificial femoral head for arthroplasty of the hip joint, J. Bone Joint Surg. Br. 32-B (1950) 166-173.

[3] A.T. MOORE, The self-locking metal hip prosthesis, J. Bone Joint Surg. Am. 39-A (1957) 811-827.

[4] G.K. McKee, Cup Arthroplasty of the Hip, with Film, Proc. R. Soc. Med. 41 (1948) 394.

[5] G.K. McKee, J. Watson-Farrar, Replacement of arthritic hips by the McKee-Farrar prosthesis, J. Bone Joint Surg. Br. 48 (1966) 245-259.

[6] A. Unsworth, Tribology of human and artificial joints, Proc. Inst. Mech. Eng. H. 205 (1991) 163-172.

[7] R.B. Welch, J. Charnley, Low-friction arthroplasty of the hip in rheumatoid arthritis and ankylosing spondylitis, Clin. Orthop. Relat. Res. 72 (1970) 22-32.

[8] J. Charnley, The long-term results of low-friction arthroplasty of the hip performed as a primary intervention, J. Bone Joint Surg. Br. 54 (1972) 61-76.

[9] http://www.saimm.co.za/Journal/v077n04p093.pdf, access on Apr.25, 2011.

[10] K.A. Gustke, The Natural-Knee system: 25 years of successful results, Am. J. Orthop. (Belle Mead NJ). 39 (2010) 5-8.

[11] J. Brettle, A survey of the literature on metallic surgical implants, Injury. 2 (1970) 26-39.

[12] P. Huang, Martensitic Transformation and its Role on the Tribological Behavior of a CoCrMo Implant Alloy, PhD Thesis, University of Wisconsin-Milwaukee (1997) 206.

[13] ASTM F1537-07 Standard Specification for Wrought Cobalt 28Chromium 6Molybdenum Alloys for Surgical Implants (UNS R31537, UNS R31538, and UNS R31539), ASTM F1537-07. (2007).

[14] ASTM F562 - 07 Standard Specification for Wrought 35Cobalt 35Nickel 20Chromium 10Molybdenum Alloy for Surgical Implant Applications (UNS R30035), ASTM F562-07. (2007).

[15] ASTM F563-00 Standard Specification for Wrought Cobalt 20Nickel 20Chromium 3.5Molybdenum 3.5Tungsten 5Iron Alloy for Surgical Implant Applications (UNS R30563), ASTM F563-00. (2000).

[16] C. Leyens, M. Peters, Titanium and Titanium Alloys : Fundamentals and Applications, Wiley-VCH; John Wiley distributor, Weinheim; Chichester, 2003.

[17] H.J. Rack, J.I. Qazi, Titanium alloys for biomedical applications, Mater. Sci. Eng. C. 26 (2006) 1269-1277.

[18] M.H. Huo, K.G. Stockton, M.A. Mont, J. Parvizi, What's new in total hip arthroplasty, J. Bone Joint Surg. Am. 92 (2010) 2959-2972.

[19] Y. Oshida, Bioscience and Bioengineering of Titanium Materials, Elsevier, New York 2007.

[20] Y. Tsutsumi, D. Nishimura, H. Doi, N. Nomura, T. Hanawa, Cathodic alkaline treatment of zirconium to give the ability to form calcium phosphate, Acta Biomater. 6 (2010) 4161-4166.

[21] G.E. Wnek, G.L. Bowlin, Encyclopedia of Biomaterials and Biomedical Engineering, Marcel Dekker, Inc., New York, 2004.

[22] P. Minaire, Immobilization osteoporosis: a review, Clin. Rheumatol. Suppl 2 (1989) 95-103.

[23] D.A. Puleo, A. Nanci, Understanding and controlling the bone-implant interface, Biomaterials. 20 (1999) 2311-2321.

[24] W.E. Brown, L.C. Chow, Chemical Properties of Bone Mineral, Annu. Rev. Mater. Sci. 6 (1976) 213-236.

[25] B. Leon, J.A. Jansen, Thin Calcium Phosphate Coatings for Medical Implants, Springer, London, 2009.

[26] S.A. Catledge, M.D. Fries, Y.K. Vohra, W.R. Lacefield, J.E. Lemons, S. Woodard, R. Venugopalan, Nanostructured ceramics for biomedical implants, J. Nanosci Nanotechnol. 2 (2002) 293-312.

[27] Y. Yang, K. Kim, J.L. Ong, A review on calcium phosphate coatings produced using a sputtering process—an alternative to plasma spraying, Biomaterials. 26 (2005) 327-337.

[28] L. Sun, C.C. Berndt, K.A. Gross, A. Kucuk, Material fundamentals and clinical performance of plasma-sprayed hydroxyapatite coatings: a review, J. Biomed. Mater. Res. 58 (2001) 570-592.

[29] M. Yoshinari, Y. Ohtsuka, T. Dérand, Thin hydroxyapatite coating produced by the ion beam dynamic mixing method, Biomaterials. 15 (1994) 529-535.

[30] H. Li, K.A. Khor, P. Cheang, Thermal sprayed hydroxyapatite splats: nanostructures, pore formation mechanisms and TEM characterization, Biomaterials. 25 (2004) 3463-3471.

[31] K.A. Gross, C.C. Berndt, Thermal processing of hydroxyapatite for coating production, J. Biomed. Mater. Res. 39 (1998) 580-587.

[32]http://www.fda.gov/downloads/MedicalDevices/DeviceRegulationandGuidance/GuidanceDocuments/ucm080225.Pdf, access on Apr. 03, 2011.

[33] R.B. Heimann, Plasma-Spray Coating: Principles and Applications, VCH Publishers, Cambridge, England, 1996.

[34] K.A. Gross, C.C. Berndt, Thermal processing of hydroxyapatite for coating production, J. Biomed. Mater. Res. 39 (1998) 580-587.

[35] G. Hallan, E. Dybvik, O. Furnes, L.I. Havelin, Metal-backed acetabular components with conventional polyethylene: a review of 9113 primary components with a follow-up of 20 years, J. Bone Joint Surg. Br. 92 (2010) 196-201.

[36] J.C. Schrama, B. Espehaug, G. Hallan, L.B. Engesaeter, O. Furnes, L.I. Havelin, B.T. Fevang, Risk of revision for infection in primary total hip and knee

arthroplasty in patients with rheumatoid arthritis compared with osteoarthritis: a prospective, population-based study on 108,786 hip and knee joint arthroplasties from the Norwegian Arthroplasty Register, Arthritis Care. Res. (Hoboken). 62 (2010) 473-479.

[37] Y.C. Tsui, C. Doyle, T.W. Clyne, Plasma sprayed hydroxyapatite coatings on titanium substrates. Part 1: Mechanical properties and residual stress levels, Biomaterials. 19 (1998) 2015-2029.

[38] Y.C. Tsui, C. Doyle, T.W. Clyne, Plasma sprayed hydroxyapatite coatings on titanium substrates. Part 2: optimisation of coating properties, Biomaterials. 19 (1998) 2031-2043.

[39] K. Duan, R.Z. Wang, Surface modifications of bone implants through wet chemistry, J. Mater. Chem. 16 (2006) 2309-2321.

[40] T. Wan, H. Aoki, J. Hikawa, J.H. Lee, RF-magnetron sputtering technique for producing hydroxyapatite coating film on various substrates, Biomed. Mater. Eng. 17 (2007) 291-297.

[41] J.M. Choi, H.E. Kim, I.S. Lee, Ion-beam-assisted deposition (IBAD) of hydroxyapatite coating layer on Ti-based metal substrate, Biomaterials. 21 (2000) 469-473.

[42] M. Yoshinari, Y. Ohtsuka, T. Derand, Thin hydroxyapatite coating produced by the ion beam dynamic mixing method, Biomaterials. 15 (1994) 529-535.

[43] R.M. Trommer, L.A. Santos, C.P. Bergmann, Alternative technique for hydroxyapatite coatings, Surf. Coat. Tech. 201 (2007) 9587-9593.

[44] S. Mändl, B. Rauschenbach, Improving the biocompatibility of medical implants with plasma immersion ion implantation, Surf. Coat. Tech. 156 (2002) 276-283.

[45] V. Nelea, C. Morosanu, M. Iliescu, I.N. Mihailescu, Microstructure and mechanical properties of hydroxyapatite thin films grown by RF magnetron sputtering, Surf. Coat. Tech.. 173 (2003) 315-322.

[46] T.N. Kim, Q.L. Feng, Z.S. Luo, F.Z. Cui, J.O. Kim, Highly adhesive hydroxyapatite coatings on alumina substrates prepared by ion-beam assisted deposition, Surf. Coat. Tech. 99 (1998) 20-23.

[47] J.A. Darr, Z.X. Guo, V. Raman, M. Bououdina, I.U. Rehman, Metal organic chemical vapour deposition (MOCVD) of bone mineral like carbonated hydroxyapatite coatings, Chem. Commun. (Camb). (6) (2004) 696-697.

[48] I. Zhitomirsky, Cathodic electrodeposition of ceramic and organoceramic materials. Fundamental aspects, Adv. Colloid Interface Sci. 97 (2002) 279-317.

[49] J. Redepenning, J.P. McIsaac, Electrocrystallization of brushite coatings on prosthetic alloys, Chem. Mater.. 2 (1990) 625-627.

[50] S. Rossler, A. Sewing, M. Stolzel, R. Born, D. Scharnweber, M. Dard, H. Worch, Electrochemically assisted deposition of thin calcium phosphate coatings at

near-physiological pH and temperature, J. Biomed. Mater. Res. A. 64 (2003) 655-663.

[51] S. Ban, S. Maruno, Hydrothermal-electrochemical deposition of hydroxyapatite, J. Biomed. Mater. Res. 42 (1998) 387-395.

[52] S. Ban, S. Maruno, Morphology and microstructure of electrochemically deposited calcium phosphates in a modified simulated body fluid, Biomaterials. 19 (1998) 1245-1253.

[53] S. Ban, S. Maruno, Effect of temperature on electrochemical deposition of calcium phosphate coatings in a simulated body fluid, Biomaterials. 16 (1995) 977-981.

[54] S. Ban, S. Maruno, N. Arimoto, A. Harada, J. Hasegawa, Effect of electrochemically deposited apatite coating on bonding of bone to the HA-G-Ti composite and titanium, J. Biomed. Mater. Res. 36 (1997) 9-15.

[55] S. Roessler, R. Born, D. Scharnweber, H. Worch, A. Sewing, M. Dard, Biomimetic coatings functionalized with adhesion peptides for dental implants, J. Mater. Sci. Mater. Med. 12 (2001) 871-877.

[56] S. Lin, R.Z. LeGeros, J.P. LeGeros, Adherent octacalciumphosphate coating on titanium alloy using modulated electrochemical deposition method, J. Biomed. Mater. Res. A. 66 (2003) 819-828.

[57] J. Wang, P. Layrolle, M. Stigter, K. de Groot, Biomimetic and electrolytic calcium phosphate coatings on titanium alloy: physicochemical characteristics and cell attachment, Biomaterials. 25 (2004) 583-592.

[58] S. Miao, W. Weng, Z. Li, K. Cheng, P. Du, G. Shen, G. Han, Electrolytic deposition of octacalcium phosphate/collagen composite coating on titanium alloy, J. Mater. Sci. Mater. Med. 20 (2009) 131-134.

[59] X. Cheng, M. Filiaggi, S.G. Roscoe, Electrochemically assisted co-precipitation of protein with calcium phosphate coatings on titanium alloy, Biomaterials. 25 (2004) 5395-5403.

[60] I. Zhitomirsky, L. Gal-Or, Electrophoretic deposition of hydroxyapatite, J. Mater. Sci. Mater. Med. 8 (1997) 213-219.

[61] S. Yamaguchi, T. Yabutsuka, M. Hibino, T. Yao, Generation of hydroxyapatite patterns by electrophoretic deposition, J. Mater. Sci. Mater. Med. 19 (2008) 1419-1424.

[62] A.J.S. Peaker, J.T. Czernuszka, The effect of electric field on the formation of hydroxyapatite coatings, Thin Solid Films. 287 (1996) 174-183.

[63] A.R. Boccaccini, S. Keim, R. Ma, Y. Li, I. Zhitomirsky, Electrophoretic deposition of biomaterials, J. R. Soc. Interface. 7 Suppl 5 (2010) S581-613.

[64] X. Pang, T. Casagrande, I. Zhitomirsky, Electrophoretic deposition of hydroxyapatite-CaSiO3-chitosan composite coatings, J. Colloid Interface Sci. 330 (2009) 323-329.

[65] H.M. Kim, F. Miyaji, T. Kokubo, T. Nakamura, Preparation of bioactive Ti and its alloys via simple chemical surface treatment, J. Biomed. Mater. Res. 32 (1996) 409-417.

[66] T. Miyazaki, H.M. Kim, F. Miyaji, T. Kokubo, H. Kato, T. Nakamura, Bioactive tantalum metal prepared by NaOH treatment, J. Biomed. Mater. Res. 50 (2000) 35-42.

[67] H.M. Kim, F. Miyaji, T. Kokubo, T. Nakamura, Effect of heat treatment on apatite-forming ability of Ti metal induced by alkali treatment, J. Mater. Sci. Mater. Med. 8 (1997) 341-347.

[68] M. Wei, H.-. Kim, T. Kokubo, J.H. Evans, Optimising the bioactivity of alkaline-treated titanium alloy, Mater. Sci. Eng. C. 20 (2002) 125-134.

[69] H.B. Wen, J.R. De Wijn, Q. Liu, K. De Groot, F.Z. Cui, A simple method to prepare calcium phosphate coatings on Ti6Al4V, J. Mater. Sci. Mater. Med. 8 (1997) 765-770.

[70] H.B. Wen, J.G. Wolke, J.R. de Wijn, Q. Liu, F.Z. Cui, K. de Groot, Fast precipitation of calcium phosphate layers on titanium induced by simple chemical treatments, Biomaterials. 18 (1997) 1471-1478.

[71] T. Kokubo, H.M. Kim, M. Kawashita, Novel bioactive materials with different mechanical properties, Biomaterials. 24 (2003) 2161-2175.

[72] P. Li, Biomimetic nano-apatite coating capable of promoting bone ingrowth, J. Biomed. Mater. Res. A. 66 (2003) 79-85.

[73] S. Mann, Biomineralization : Principles and Concepts in Bioinorganic Materials Chemistry, Oxford University Press, New York, 2001.

[74] K. Duan, A. Tang, R. Wang, A new evaporation-based method for the preparation of biomimetic calcium phosphate coatings on metals, Mater. Sci. Eng. C. 29 (2009) 1334-1337.

[75] L. Wang, J. Luo, Formation of Hydroxyapatite Coating on Anodic Titanium Dioxide Nanotubes *Via* an Efficient Dipping Treatment, Metall. Mater. Trans. A. (2010) 1-10.

[76] S. Ono, A. Kiyotake, H. Asoh, Effect of Nanostructured Surface of Light Metals on Hydroxyapatite Coating, ECS Trans. 11 (2008) 1-8.

[77] A. Kodama, S. Bauer, A. Komatsu, H. Asoh, S. Ono, P. Schmuki, Bioactivation of titanium surfaces using coatings of TiO_2 nanotubes rapidly pre-loaded with synthetic hydroxyapatite, Acta Biomater. 5 (2009) 2322-2330.

[78] L. Wang, J. Luo, Fabrication and formation of bioactive anodic zirconium oxide nanotubes containing presynthesized hydroxyapatite via alternative immersion method, Mater.Sci. Eng. C. 31 (2011) 748-754.

[79] A.J. Bard, L.R. Faulkner, Electrochemical Methods : Fundamentals and Applications, 2nd ed., Wiley, New York, 2001.

[80] A.J. Bard, I. Rubinstein, Electroanalytical Chemistry, Marcel Dekker, New York, 2004.

[81] M. Schlesinger, Modern Aspect of Electrochemistry, Springer, New York, 2008.

[82] A. Domenech-Carbo, Electrochemistry of Porous Materials, Taylor & Francis, Boca Raton, 2010.

[83] A.J. Bard, Integrated Chemical Systems : A Chemical Approach to Nanotechnology, Wiley, New York, 1994.

[84] X. Liu, P.K. Chu, C. Ding, Surface modification of titanium, titanium alloys, and related materials for biomedical applications, Mater. Sci. Eng. R. 47 (2004) 49-121.

[85] Y.T. Sul, C.B. Johansson, Y. Jeong, K. Roser, A. Wennerberg, T. Albrektsson, Oxidized implants and their influence on the bone response, J. Mater. Sci. Mater. Med. 12 (2001) 1025-1031.

[86] W.W. Son, X. Zhu, H.I. Shin, J.L. Ong, K.H. Kim, In vivo histological response to anodized and anodized/hydrothermally treated titanium implants, J. Biomed. Mater. Res. B. Appl. Biomater. 66 (2003) 520-525.

[87] M. Fini, A. Cigada, G. Rondelli, R. Chiesa, R. Giardino, G. Giavaresi, N. Nicoli Aldini, P. Torricelli, B. Vicentini, In vitro and in vivo behaviour of Ca- and P-enriched anodized titanium, Biomaterials. 20 (1999) 1587-1594.

[88] C.A. Grimes, G.K. Mor, Use of TiO_2 Nanotube Arrays for Biological Applications, in: C.A. Grimes, G.K. Mor (Eds.), TiO_2 Nanotube Arrays Synthesis, Properties, and Applications, Springer, New York, 2009.

[89] A. Ghicov, P. Schmuki, Self-ordering electrochemistry: a review on growth and functionality of TiO2 nanotubes and other self-aligned MO(x) structures, Chem. Commun. (Camb). (20) (2009) 2791-2808.

[90] J.P. Schreckenbach, G. Marx, F. Schlottig, M. Textor, N.D. Spencer, Characterization of anodic spark-converted titanium surfaces for biomedical applications, J. Mater. Sci. Mater. Med. 10 (1999) 453-457.

[91] J. Choi, R.B. Wehrspohn, J. Lee, U. Gösele, Anodization of nanoimprinted titanium: A comparison with formation of porous alumina, Electrochim. Acta. 49 (2004) 2645-2652.

[92] R. Chiesa, E. Sandrini, M. Santin, G. Rondelli, A. Cigada, Osteointegration of titanium and its alloys by anodic spark deposition and other electrochemical techniques: a review, J. Appl. Biomater. Biomech. 1 (2003) 91-107.

[93] H. Habazaki, M. Uozumi, H. Konno, K. Shimizu, P. Skeldon, G.E. Thompson, Crystallization of anodic titania on titanium and its alloys, Corros. Sci. 45 (2003) 2063-2073.

[94] N. Tran, T.J. Webster, Nanotechnology for bone materials, Wiley Interdiscip. Rev. Nanomed Nanobiotechnol. 1 (2009) 336-351.

[95] C. Yao, T.J. Webster, Anodization: a promising nano-modification technique of titanium implants for orthopedic applications, J. Nanosci Nanotechnol. 6 (2006) 2682-2692.

[96] D.V. Bavykin, F.C. Walsh, P. O'Brien, H. Craighead, H. Kroto, Titanate and Titania Nanotubes: Synthesis, Properties and Applications, The Royal Society of Chemistry, London, 2009.

[97] Y. Han, S. Hong, K. Xu, Structure and in vitro bioactivity of titania-based films by micro-arc oxidation, Surf. Coat.Tech.. 168 (2003) 249-258.

[98] H. Ishizawa, M. Ogino, Characterization of thin hydroxyapatite layers formed on anodic titanium oxide films containing Ca and P by hydrothermal treatment, J. Biomed. Mater. Res. 29 (1995) 1071-1079.

[99] H. Ishizawa, M. Ogino, Formation and characterization of anodic titanium oxide films containing Ca and P, J. Biomed. Mater. Res. 29 (1995) 65-72.

[100] D. Wei, Y. Zhou, D. Jia, Y. Wang, Characteristic and in vitro bioactivity of a microarc-oxidized TiO(2)-based coating after chemical treatment, Acta Biomater. 3 (2007) 817-827.

[101] J. Xie, B.L. Luan, Formation of hydroxyapatite coating using novel chemo-biomimetic method, J. Mater. Sci. Mater. Med. 19 (2008) 3211-3220.

[102] J. Xie, B.L. Luan, Nanometer-scale surface modification of Ti6Al4V alloy for orthopedic applications, J. Biomed. Mater. Res. A. 84 (2008) 63-72.

[103] M. Fini, A. Cigada, G. Rondelli, R. Chiesa, R. Giardino, G. Giavaresi, N. Nicoli Aldini, P. Torricelli, B. Vicentini, In vitro and in vivo behaviour of Ca- and P-enriched anodized titanium, Biomaterials. 20 (1999) 1587-1594.

[104] J.Y. Suh, B.C. Jang, X. Zhu, J.L. Ong, K. Kim, Effect of hydrothermally treated anodic oxide films on osteoblast attachment and proliferation, Biomaterials. 24 (2003) 347-355.

[105] X. Zhu, J. Chen, L. Scheideler, T. Altebaeumer, J. Geis-Gerstorfer, D. Kern, Cellular reactions of osteoblasts to micron- and submicron-scale porous structures of titanium surfaces, Cells Tissues Organs. 178 (2004) 13-22.

[106] X. Zhu, J. Chen, L. Scheideler, R. Reichl, J. Geis-Gerstorfer, Effects of topography and composition of titanium surface oxides on osteoblast responses, Biomaterials. 25 (2004) 4087-4103.

[107] L.H. Li, H.W. Kim, S.H. Lee, Y.M. Kong, H.E. Kim, Biocompatibility of titanium implants modified by microarc oxidation and hydroxyapatite coating, J. Biomed. Mater. Res. A. 73 (2005) 48-54.

[108] Y.T. Sul, C. Johansson, E. Byon, T. Albrektsson, The bone response of oxidized bioactive and non-bioactive titanium implants, Biomaterials. 26 (2005) 6720-6730.

[109] E. Sandrini, C. Morris, R. Chiesa, A. Cigada, M. Santin, In vitro assessment of the osteointegrative potential of a novel multiphase anodic spark deposition coating for orthopaedic and dental implants, J. Biomed. Mater. Res. B. Appl. Biomater. 73 (2005) 392-399.

[110] G. Giavaresi, M. Fini, A. Cigada, R. Chiesa, G. Rondelli, L. Rimondini, N.N. Aldini, L. Martini, R. Giardino, Histomorphometric and microhardness

assessments of sheep cortical bone surrounding titanium implants with different surface treatments, J. Biomed. Mater. Res. A. 67 (2003) 112-120.

[111] V. Zwilling, E. Darque-Ceretti, A. Boutry-Forveille, D. David, M.Y. Perrin, M. Aucouturier, Structure and physicochemistry of anodic oxide films on titanium and T6Al4V alloy, Surf. Interface Anal. 27 (1999) 629-637.

[112] V. Zwilling, M. Aucouturier, E. Darque-Ceretti, Anodic oxidation of titanium and Ti6Al4V alloy in chromic media. An electrochemical approach, Electrochim. Acta. 45 (1999) 921-929.

[113] D. Gong, C.A. Grimes, O.K. Varghese, W.C. Hu, R.S. Singh, Z. Chen, E.C. Dickey, Titanium oxide nanotube arrays prepared by anodic oxidation, J. Mater. Res. 16 (2001) 3331-3334.

[114] G.K. Mor, O.K. Varghese, M. Paulose, C.A. Grimes, A self-cleaning, room-temperature titania-nanotube hydrogen gas sensor, Sensor Lett. 1 (2003) 42-46.

[115] G.K. Mor, O.K. Varghese, M. Paulose, N. Mukherjee, C.A. Grimes, Fabrication of tapered, conical-shaped titania nanotubes, J. Mater. Res. 18 (2003) 2588-2593.

[116] H. Tsuchiya, J.M. Macak, I. Sieber, P. Schmuki, Self-organized high-aspect-ratio nanoporous zirconium oxides prepared by electrochemical anodization, Small. 1 (2005) 722-725.

[117] H. Tsuchiya, P. Schmuki, Self-organized high aspect ratio porous hafnium oxide prepared by electrochemical anodization, Electrochem. Comm. 7 (2005) 49-52.

[118] N.K. Allam, X.J. Feng, C.A. Grimes, Self-Assembled Fabrication of Vertically Oriented Ta_2O_5 Nanotube Arrays, and Membranes Thereof, by One-Step Tantalum Anodization, Chem. Mater. 20 (2008) 6477-6481.

[119] H. Tsuchiya, J.M. Macak, I. Sieber, L. Taveira, A. Ghicov, K. Sirotna, P. Schmuki, Self-organized porous WO_3 formed in NaF electrolytes, Electrochem. Comm. 7 (2005) 295-298.

[120] I. Sieber, H. Hildebrand, A. Friedrich, P. Schmuki, Formation of self-organized niobium porous oxide on niobium, Electrochem. Comm. 7 (2005) 97-100.

[121] H. Jha, R. Hahn, P. Schmuki, Ultrafast oxide nanotube formation on TiNb, TiZr and TiTa alloys by rapid breakdown anodization, Electrochim. Acta. 55 (2010) 8883-8887.

[122] A. Ghicov, S. Aldabergenova, H. Tsuchyia, P. Schmuki, TiO_2-Nb_2O_5 nanotubes with electrochemically tunable morphologies, Angew. Chemie-Inter. Ed. 45 (2006) 6993-6996.

[123] S. Bauer, S. Kleber, P. Schmuki, TiO_2 nanotubes: Tailoring the geometry in H_3PO_4/HF electrolytes, Electrochem. Comm. 8 (2006) 1321-1325.

[124] S. Berger, J. Faltenbacher, S. Bauer, P. Schmuki, Enhanced self-ordering of anodic ZrO_2 nanotubes in inorganic and organic electrolytes using two-step anodization, Phys. Stat. Solidi-RRL. 2 (2008) 102-104.

[125] J.M. Macák, H. Tsuchiya, P. Schmuki, High-Aspect-Ratio TiO_2 Nanotubes by Anodization of Titanium, Angew. Chemie Inter. Ed. 44 (2005) 2100-2102.

[126] J.M. Macak, P. Schmuki, Anodic growth of self-organized anodic TiO_2 nanotubes in viscous electrolytes, Electrochim. Acta. 52 (2006) 1258-1264.

[127] J.M. Macak, H. Tsuchiya, A. Ghicov, K. Yasuda, R. Hahn, S. Bauer, P. Schmuki, TiO_2 nanotubes: Self-organized electrochemical formation, properties and applications, Curr. Opi. in Solid State Mater. Sci.. 11 (2007) 3-18.

[128] K.S. Raja, T. Gandhi, M. Misra, Effect of water content of ethylene glycol as electrolyte for synthesis of ordered titania nanotubes, Electrochem. Comm. 9 (2007) 1069-1076.

[129] L.V. Taveira, J.M. Macak, K. Sirotna, L.F.P. Dick, P. Schmuki, Voltage oscillations and morphology during the galvanostatic formation of self-organized TiO_2 nanotubes, J. Electrochem. Soc. 153 (2006) B137-B143.

[130] K. Yasuda, P. Schmuki, Control of morphology and composition of self-organized zirconium titanate nanotubes formed in $(NH_4)_2SO_4/NH_4F$ electrolytes, Electrochim. Acta. 52 (2007) 4053-4061.

[131] M. Paulose, H.E. Prakasam, O.K. Varghese, L. Peng, K.C. Popat, G.K. Mor, T.A. Desai, C.A. Grimes, TiO_2 nanotube arrays of 1000 mu m length by

anodization of titanium foil: Phenol red diffusion, J. Phys. Chem. C. 111 (2007) 14992-14997.

[132] C. Yao, T.J. Webster, Anodization: a promising nano-modification technique of titanium implants for orthopedic applications, J. Nanosci Nanotechnol. 6 (2006) 2682-2692.

[133] K. Yasuda, J.M. Macak, S. Berger, A. Ghicov, P. Schmuki, Mechanistic aspects of the self-organization process for oxide nanotube formation on valve metals, J. Electrochem. Soc. 154 (2007) C472-C478.

[134] S.C. Han, J.M. Doh, J.K. Yoon, G.H. Kim, J.Y. Byun, S.H. Han, K.T. Hong, S.I. Kwun, Highly ordered self-organized TiO_2 nanotube arrays prepared by a multi-step anodic oxidation process, Metals Mater. Inter. 15 (2009) 493-499.

[135] J.L. Tao, J.L. Zhao, C.C. Tang, Y.R. Kang, Y.X. Li, Mechanism study of self-organized TiO_2 nanotube arrays by anodization, New J. Chem.. 32 (2008) 2164-2168.

[136] D. Gong, C.A. Grimes, O.K. Varghese, W.C. Hu, R.S. Singh, Z. Chen, E.C. Dickey, Titanium oxide nanotube arrays prepared by anodic oxidation, J. Mater. Res. 16 (2001) 3331-3334.

[137] S. Oh, R.R. Finõnes, C. Daraio, L. Chen, S. Jin, Growth of nano-scale hydroxyapatite using chemically treated titanium oxide nanotubes, Biomaterials. 26 (2005) 4938-4943.

[138] S.Q. Li, G.M. Zhang, D.Z. Guo, L.G. Yu, W. Zhang, Anodization Fabrication of Highly Ordered TiO_2 Nanotubes, J. Phys. Chem. C. 113 (2009) 12759-12765.

[139] S.P. Albu, A. Ghicov, J.M. Macak, P. Schmuki, 250 mu m long anodic TiO_2 nanotubes with hexagonal self-ordering, Phys. Stat. Solidi-RRL. 1 (2007) R65-R67.

[140] S. Berger, F. Jakubka, P. Schmuki, Formation of hexagonally ordered nanoporous anodic zirconia, Electrochem. Comm. 10 (2008) 1916-1919.

[141] Y. Shin, S. Lee, A freestanding membrane of highly ordered anodic ZrO_2 nanotube arrays, Nanotech. 20 (2009).

[142] Y. Alivov, Z.Y. Fan, D. Johnstone, Titanium nanotubes grown by titanium anodization, J. Appl. Phys. 106 (2009).

[143] M.A. Khan, H.T. Jung, O.B. Yang, Synthesis and characterization of ultrahigh crystalline TiO_2 nanotubes, J Phys Chem B. 110 (2006) 6626-6630.

[144] J.M. Macak, S. Albu, D.H. Kim, I. Paramasivam, S. Aldabergerova, P. Schmuki, Multilayer TiO_2-nanotube formation by two-step anodization, Electrochem. Solid State Lett. 10 (2007) K28-K31.

[145] K. Yasuda, P. Schmuki, Formation of self-organized zirconium titanate nanotube layers by alloy anodization, Adv Mater. 19 (2007) 1757-+.

[146] Y. Alivov, Z.Y. Fan, A TiO_2 nanostructure transformation: from ordered nanotubes to nanoparticles, Nanotech.. 20 (2009).

[147] G.A. Crawford, N. Chawla, Porous hierarchical TiO_2 nanostructures: Processing and microstructure relationships, Acta Mater. 57 (2009) 854-867.

[148] Y. Yang, X.H. Wang, L.T. Li, Crystallization and phase transition of titanium oxide nanotube arrays, J Am Ceram Soc. 91 (2008) 632-635.

[149] L.N. Wang, J.L. Luo, Enhancing the bioactivity of zirconium with the coating of anodized ZrO_2 nanotubular arrays prepared in phosphate containing electrolyte, Electrochem. Comm. 12 (2010) 1559-1562.

[150] J.L. Zhao, X.X. Wang, R.Q. Xu, F.B. Meng, L.M. Guo, Y.X. Li, Fabrication of high aspect ratio zirconia nanotube arrays by anodization of zirconium foils, Mater. Lett. 62 (2008) 4428-4430.

[151] J.M. Macak, S. Aldabergerova, A. Ghicov, P. Schmuki, Smooth anodic TiO_2 nanotubes: annealing and structure, Phys. Status Solidi A-Appl. Mater. Sci. 203 (2006) R67-R69.

[152] L.M. Guo, J.L. Zhao, X.X. Wang, X.W. Xu, H.Y. Liu, Y.X. Li, Structure and Bioactivity of Zirconia Nanotube Arrays Fabricated by Anodization, Inter. J. Appl. Ceram. Tech. 6 (2009) 636-641.

[153] D. Fang, K.L. Huang, Z.P. Luo, Y. Wang, S.Q. Liu, Q.G. Zhang, Freestanding ZrO_2 nanotube membranes made by anodic oxidation and effect of heat treatment on their morphology and crystalline structure, J. Mater. Chem. 21 (2011) 4989-4994.

[154] S.A. Brown, J.E. Lemons, Medical Applications of Titanium and its Alloys : The Material and Biological Issues, Astm, West Conshohocken, 1996.

[155] M. Fernandez-Fairen, V. Querales, A. Jakowlew, A. Murcia, J. Ballester, Tantalum is a good bone graft substitute in tibial tubercle advancement, Clin. Orthop. Relat. Res. 468 (2010) 1284-1295.

[156] M. Geetha, A.K. Singh, R. Asokamani, A.K. Gogia, Ti based biomaterials, the ultimate choice for orthopaedic implants – A review, Progress Mater. Sci. 54 (2009) 397-425.

[157] T. Kokubo, H. Takadama, How useful is SBF in predicting in vivo bone bioactivity? Biomaterials. 27 (2006) 2907-2915.

[158] H. Tsuchiya, J.M. Macak, L. Muller, J. Kunze, F. Muller, P. Greil, S. Virtanen, P. Schmuki, Hydroxyapatite growth on anodic TiO_2 nanotubes, J. Biomed. Mater. Res. A. 77A (2006) 534-541.

[159] L. Gao, B. Feng, J.X. Wang, X. Lu, D.L. Liu, S.X. Qu, J. Weng, Micro/Nanostructural Porous Surface on Titanium and Bioactivity, J. Biomed. Mater. Res. B.App. Biomater. 89B (2009) 335-341.

[160] J. Kunze, L. Muller, J.M. Macak, P. Greil, P. Schmuki, F.A. Muller, Time-dependent growth of biomimetic apatite on anodic TiO_2 nanotubes, Electrochim. Acta. 53 (2008) 6995-7003.

[161] A. Pittrof, S. Bauer, P. Schmuki, Micropatterned TiO_2 nanotube surfaces for site-selective nucleation of hydroxyapatite from simulated body fluid, Acta Biomater.. 7 (2011) 424-431.

[162] K.S. Raja, G.L. Craviso, M. Misra, A.M. Raichur, A. Kar, Development of Novel Biocompatible Hydroxyapatite Coated Nanotubular Titania for Implant Application, Ad. Bioceram. Porous Ceram. 29 (2009) 227-237.

[163] B. Feng, X.J. Chu, J.M. Chen, J.X. Wang, X.O. Lu, J. Weng, Hydroxyapatite coating on titanium surface with titania nanotube layer and its bond strength to substrate, J. Porous Mater. 17 (2010) 453-458.

[164] L.M. Guo, J.L. Zhao, X.X. Wang, R.Q. Xu, Z.M. Lu, Y.X. Li, Bioactivity of zirconia nanotube arrays fabricated by electrochemical anodization, Mater. Sci. Eng. C. 29 (2009) 1174-1177.

[165] X.F. Xiao, T. Tian, R.F. Liu, H.D. She, Influence of titania nanotube arrays on biomimetic deposition apatite on titanium by alkali treatment, Mater. Chem. Phys. 106 (2007) 27-32.

[166] Y.K. Lai, Y.X. Huang, H. Wang, J.Y. Huang, Z. Chen, C.J. Lin, Selective formation of ordered arrays of octacalcium phosphate ribbons on TiO_2 nanotube surface by template-assisted electrodeposition, Colloids and Surfaces B-Biointer.. 76 (2010) 117-122.

[167] A. Kar, K.S. Raja, M. Misra, Electrodeposition of hydroxyapatite onto nanotubular TiO_2 for implant applications, Surf. Coat. Technol. 201 (2006) 3723-3731.

[168] K.S. Raja, M. Misra, K. Paramguru, Deposition of calcium phosphate coating on nanotubular anodized titanium, Mater. Lett. 59 (2005) 2137-2141.

[169] J. Park, S. Bauer, K. von der Mark, P. Schmuki, Nanosize and vitality: TiO_2 nanotube diameter directs cell fate, Nano Letters. 7 (2007) 1686-1691.

[170] J. Park, S. Bauer, P. Schmuki, K. von der Mark, Narrow Window in Nanoscale Dependent Activation of Endothelial Cell Growth and Differentiation on TiO_2 Nanotube Surfaces, Nano Letters. 9 (2009) 3157-3164.

[171] S. Bauer, J. Park, J. Faltenbacher, S. Berger, K. von der Mark, P. Schmuki, Size selective behavior of mesenchymal stem cells on ZrO_2 and TiO_2 nanotube arrays, Integra. Biol. 1 (2009) 525-532.

[172] Y.Y. Song, P. Roy, I. Paramasivam, P. Schmuki, Voltage-Induced Payload Release and Wettability Control on TiO_2 and TiO_2 Nanotubes, Angew. Chemie-Inter. Ed. 49 (2010) 351-354.

[173] J. Park, S. Bauer, K.A. Schlegel, F.W. Neukam, K. von der Mark, P. Schmuki, TiO_2 Nanotube Surfaces: 15 nm - An Optimal Length Scale of Surface Topography for Cell Adhesion and Differentiation, Small. 5 (2009) 666-671.

[174] E. Balaur, J.M. Macak, L. Taveira, P. Schmuki, Tailoring the wettability of TiO_2 nanotube layers, Electrochem. Comm. 7 (2005) 1066-1070.

[175] S. Bauer, J. Park, K. von der Mark, P. Schmuki, Improved attachment of mesenchymal stem cells on super-hydrophobic TiO_2 nanotubes, Acta Biomater. 4 (2008) 1576-1582.

[176] F. Schmidt-Stein, J.F. Gnichwitz, J. Salonen, R. Hahn, A. Hirsch, P. Schmuki, Electrochemical wettability control on conductive TiO_2 nanotube surfaces modified with a ferrocene redox system, Electrochem. Comm. 11 (2009) 2000-2003.

[177] C. von Wilmowsky, S. Bauer, R. Lutz, M. Meisel, F.W. Neukam, T. Toyoshima, P. Schmuki, E. Nkenke, K.A. Schlegel, In Vivo Evaluation of Anodic TiO_2 Nanotubes: An Experimental Study in the Pig, J. Biomed. Mater. Res. B Appl. Biomater. 89B (2009) 165-171.

[178] W. Lee, W.H. Smyrl, Zirconium Oxide Nanotubes Synthesized via Direct Electrochemical Anodization, Electrochem. Solid-State Lett. 8 (2005) B7-B9.

[179] S.A. Johnson, P.J. Ollivier, T.E. Mallouk, Ordered Mesoporous Polymers of Tunable Pore Size from Colloidal Silica Templates, Science. 283 (1999) 963-965.

[180] N. Wu, S. Wang, I.A. Rusakova, Inhibition of Crystallite Growth in the Sol-Gel Synthesis of Nanocrystalline Metal Oxides, Science. 285 (1999) 1375-1377.

[181] W. Cao, O.K. Tan, W. Zhu, B. Jiang, C.V. Gopal Reddy, An amorphous-like xα-Fe2O3–(1 − x)ZrO2 solid solution system for low temperature resistive-type oxygen sensing, Sensors Actuators B: Chem. 77 (2001) 421-426.

[182] E.P. Murray, T. Tsai, S.A. Barnett, A direct-methane fuel cell with a ceria-based anode, Nature. 400 (1999) 649-651.

[183] S. Park, J.M. Vohs, R.J. Gorte, Direct oxidation of hydrocarbons in a solid-oxide fuel cell, Nature. 404 (2000) 265-267.

[184] R. Hahn, S. Berger, P. Schmuki, Bright visible luminescence of self-organized ZrO_2 nanotubes, J. Solid State Electrochem.. 14 (2010) 285-288.

[185] P.E. Sinnett-Jones, J.A. Wharton, R.J.K. Wood, Micro-abrasion–corrosion of a CoCrMo alloy in simulated artificial hip joint environments, Wear. 259 (2005) 898-909.

[186] G.A. Crawford, N. Chawla, K. Das, S. Bose, A. Bandyopadhyay, Microstructure and deformation behavior of biocompatible TiO_2 nanotubes on titanium substrate, Acta Biomater. 3 (2007) 359-367.

[187] Lu-Ning Wang, Fabrication and Mechanical Properties of Anodized Zirconium Dioxide Nanotubular Arrays, J. Phys. D. 44 (2011) 075301.

Chapter 3 Experimental methods and Materials Characterization

In this chapter, all the materials fabrication, surface chemistry treatment, and materials characterization techniques will be introduced and briefly reviewed.

3.1 Fabrication of anodic ZrO_2 nanotubular arrays

The fabrication of anodic zirconium nanotubular arrays is carried out in a two-electrode cell setup by an external power supply. Figure 3-1 illustrates the schematic of the anodization setup. A zirconium foil is the anode while a platinum plate is the cathode. Before anodization, Zr foil was dip-etched in a solution containing $HF/HNO_3/H_2O$ (volume ration, 1/4/2) for 1 second to get rid of the natural-formed oxide film [1]. The electrolyte is mainly glycerin containing different volume of water and different concentration of NH_4F. By varying the electrochemical parameters, such as anodization time, voltage, and ion concentration, ZrO_2 nanotubular arrays can be obtained with different diameter and thickness.

3.2 Materials characterization methods

3.2.1 Scanning electron microscope

A scanning electron microscope (SEM) is a type of electronic technique that

images a sample surface by scanning it with a high-energy electron beam, which typically has an energy ranging from 0.5 kV to 20 kV, in a raster scan pattern. Interaction between electrons and atoms makes up the sample producing signals that contain information about the sample's surface topography, composition, and other properties such as electrical conductivity.

The types of signals produced by SEM include secondary electrons (SE), back-scattered electrons (BSE), characteristic X-rays, light (cathodoluminescence), specimen current and transmitted electrons. Among these signals, SE and BSE SEM signals are the most commonly detected signals. SE mode is primarily used to obtain the surface topography of the sample, while BSE mode is mainly coupled together with energy dispersive x-ray spectroscopy to provide the distribution of different elements in the sample.

SEM micrographs have a large depth of field yielding a characteristic three-dimensional appearance useful for understanding the surface structure of a sample. This is exemplified by the micrograph of pollen shown to the right. A wide range of magnifications is possible, from about 10 times (about equivalent to that of a powerful hand-lens) to more than 500,000 times, about 250 times the magnification limit of the best light microscopes. Detailed information of theory and techniques of SEM has been authored by Goldstein et al [2]. In present work, a JEOL 6301F field emission scanning electron microscopy (FE-SEM) is applied to analyze the surface morphology. By applying SEM, the nanotubular diameter and

the array thickness can be obtained by reading the image.

3.2.2 Energy dispersive x-ray spectroscopy

Energy dispersive x-ray spectroscopy (EDS) is an analytical technique used for elemental analysis or chemical characterization of a specimen. It is normally coupled with SEM or TEM to extend the variety of those techniques. The principle of EDS can be simply interpreted as follow. When a high-energy beam of electrons, or photons, or X-rays is focused onto a specimen, some electrons of the inner shells are excited, ejecting from the shell while creating holes where the electrons were. The electrons from outer, higher-energy shells then drop into and fill the holes, and the difference in energy between the higher-energy shell and the lower energy shell may be released in the form of an X-ray. The energy of the characteristic X-rays can be used to indentify the unique element(s) present, while the relative intensity of different elements can be employed to determine the percentage of the elements in the specimen [2].

3.2.3 X-ray diffraction

X-ray diffraction (XRD) techniques are a family of non-destructive analytical techniques which reveal information about the crystallographic structure, chemical composition, and physical properties of materials and thin films. These techniques are based on observing the scattered intensity of an X-ray beam hitting a sample as a function of incident and scattered angle, polarization, and wavelength or energy [2].

Powder diffraction and thin film diffraction are the two most commonly used modes in XRD. Powder diffraction mode is performed by varying the X-ray beam incident angle within a fairly large range (0° to 90°), while thin film diffraction mode, which is also commonly called small angle diffraction, is performed by fixing the incident beam at a small angle (normally between 1° and 5°) allowing the X-ray interaction depth on the scale of hundreds of nanometers to several microns. Hence, powder diffraction is commonly used to identify unknown substances while small angle diffraction mode is preferred to characterize thin films. Other than these two modes, XRD techniques are also applied to characterize thin film thickness, crystallographic structure, strain, distribution of crystalline orientations, and quantify grain size. A Rigaku with Cu Kα radiation source XRD is used to examine the crystal structure.

3.2.4 X-ray photoelectron spectroscopy

X-ray photoelectron spectroscopy (XPS) is a quantitative spectroscopic technique that measures the composition, chemical state, electronic state, and empirical formula of the elements at the sample surface, which is typically between 1 to 10 nm. When the X-ray hits the sample, photoelectrons escape from the sample surface. The stimulated photoelectrons are detected and measured in terms of their kinetic energy and numbers. Normally, the numbers of photoelectrons are converted to the intensity at specific binding energies to form the XPS spectrum for analyzing [3]. XPS measurement is performed using an

Axis-Ultra (Kratos Analytical) spectrometer controlled by a SUN workstation.

3.2.5 Fourier transform infrared spectroscopy

Fourier transform infrared spectroscopy (FTIR) is a technique which is used to obtain an infrared spectrum of absorption, emission, photoconductivity or Raman scattering of a solid, liquid or gas. In infrared spectroscopy, IR radiation is passed through a sample. Some of the infrared radiation is absorbed by the sample and some of it is passed through (transmitted), which correspond to the frequencies of vibrations between the bonds of the atoms. The resulting spectrum represents the molecular absorption and transmission, creating a unique characteristic of the sample. Like a fingerprint no two unique molecular structures produce the same infrared spectrum. This makes infrared spectroscopy useful for several types of analysis to identify the unknown substance, to determine the quality and consistence of the samples, and to determine the amount of components in a mixture [4]. An FT-IR, Nicolet 5700, is used to analyze the specimen in present study.

3.2.6 Transmission electron microscopy

Transmission electron microscopy (TEM) is a microscopy technique that a beam of high energy (accelerating voltage normally over 200 kV) electrons is transmitted through the ultra thin specimen and interact with the specimen to form an image on an imaging device. TEM is able to image at a significantly high magnification with high resolution due to the small wavelength of high energy

electron beam [5].

The most common mode of operation for a TEM is the bright field imaging mode. In this mode the contrast formation, when considered classically, is formed directly by occlusion and absorption of electrons in the sample. Thicker regions of the sample, or regions with a higher atomic number will appear dark, whilst regions with no sample in the beam path will appear bright – hence the term 'bright field'. On the other hand, an aperture is allowed to be inserted into the back focal plane of the objective lens in order to admit only some scattered electrons to go through it. This mode is called dark field imaging mode. Bright field imaging is used for observation of the morphology of the sample, while the dark field imaging mode is usually applied to observe the defects in sample.

By changing the focal position, the crystallographic structure of the sample can be obtained through selected area diffraction (SAD) pattern technique. In this case, electrons are treated as wave-like, rather than particle-like. Because the wavelength of high-energy electrons is a fraction of a nanometer, and the spacings between atoms in a solid is only slightly larger, the atoms act as a diffraction grating to the electrons, which are diffracted. That is, some fraction of them will be scattered to particular angles, determined by the crystal structure of the sample, while others continue to pass through the sample without deflection. As a diffraction technique, SAD can be used to identify crystal structures and examine crystal defects. It is similar to x-ray diffraction, but unique in that area as small as

several hundred nanometers in size can be examined. In present study, a JEOL 2010 TEM system is applied.

3.2.7 Secondary ion mass spectrometry

Secondary ion mass spectrometry (SIMS) is a technique used in materials science and surface science to analyze the composition of solid surfaces and thin films by sputtering the surface of the specimen with a focused primary ion beam and collecting and analyzing ejected secondary ions. These secondary ions are measured with a mass spectrometer to determine the elemental, isotopic, or molecular composition of the surface. SIMS is the most sensitive surface analysis technique, being able to detect elements present in the parts per billion range. A time of flight secondary ion mass spectrometry (ToF-SIMS) is perfomed using a PHI 7200 spectrometer equipped with two ion guns (Cs^+, Ga^+) and a reflection analyzer to obtain the surface composition in present work.

3.2.8 Microindentation test

The mechanical properties, such as Young's modulus, hardness (HV), and ratio of elastic energy (W_e) to total deformation energy (W_{tot}), were obtained in terms of microindentation. Indentation hardness tests are used to determine the hardness of a material to deformation. In microindentation hardness testing, a diamond indenter of specific geometry is impressed into the surface of the test specimen using a known applied force (commonly called a "load" or "test load") of 1 to 1000 gf. Microindentation tests typically have forces of 2 N (roughly

200 gf) and produce indentations of about 50 μm. Due to their specificity, microhardness testing can be used to observe changes in hardness on the microscopic scale. Additionally, during the course of the instrumented indentation process, a record of the depth of penetration is made, and then the area of the indent is determined using the known geometry of the indentation tip. During the indenting, various parameters, such as load and depth of penetration, can be measured. A record of these values can be plotted on a graph to create a load-displacement curve (such as the one shown in Figure 3-2). The slope of the curve, dP/dh, upon unloading is indicative of the stiffness of the contact, which is used to calculate the Young's modulus [6].

3.2.9 Universal Micro-Tribometer (UMT) for critical load and scratch test

The critical load of ZrO_2 nanotubular arrays to scratch was evaluated using a Universal Micro-Tribometer (UMT) (Center for Tribology, Inc., Campbell, CA) as shown in Figure 3-3. During the tests, a tungsten carbide tip scratched a surface under a normal load that was linearly increased within 1 min. The critical load at the point of failure of ZrO_2 nanotubular array films during scratch tests was determined by monitoring the variation in the contact electric resistance (CER) between the tip and zirconium substrate. During the scratch test, the sample is fixed on the moving stage. a normal load of 25 mN for 10 min at a sliding speed of 4 mm/s in air and water at different pH culture. The acidic solution, which is with pH value of 2.5, is made from 0.1 N HCl by adding appropriate amount of

tris-hydroxymethylaminomethane (tris). Meanwhile, the alkali solution, which is with pH value of 13, is made from 0.1 N NaOH by adjusting with appropriate amount of 0.01 N HCl. The width of the wear track was measured using a calibrated microscope system (Leica, ltd) [7].

3.2.10 Bonding strength of HA coating

The bonding strength of the HA layer to the substrate was measured using a method described by Kim et al., which is a modified ASTM C-633-08 method, using an Instron Model 4505 Universal Testing System [8, 9]. Five samples were tested to determine the bonding strength of the coating layer. Both sides of the sample were affixed to stainless steel square bars using rapid-type LePage® glue (Figure 3-4). After the glue had dried fully, a continuous tensile load was applied vertical to the sample surfaces using a weight scale. The load (N) at which the coating became separated from the substrate was recorded. The bonding strength was calculated dividing the load at fracture by the sample surface area. The adhesive strength value (MPa) was taken as the average value for the five tested samples.

3.3 Evaluation of the bioactivity of zirconium dioxide nanotubular arrays

The bioactivity of zirconium dioxide nanotubular arrays under different wet chemical treatment is evaluated by the capability of formation of HA coating

during immersion in simulated biological fluid (SBF). The ion concentration is listed in Table 3-1. An electrolyte with ionic concentrations similar to human plasma was prepared by dissolving reagent grade NaCl, KCl, $NaHCO_3$, $MgCl_2 \cdot 6H_2O$, Na_2SO_4, $CaCl_2$, and $K_2HPO_4 \cdot 3H_2O$ into DI water and buffered at pH = 7.25 with tris and HCl at 37 ^oC [10, 11]. The ratio of sample surface to the volume of SBF, S/V, was about 0.01 cm^{-1} [10]. The samples were immersed in SBF under different time interval without stirring to investigate their bioactivity. After immersion, the samples were removed, rinsed with DI water, and dried in air.

Table 3-1 Ion Concentrations in SBF and Human Blood Plasma. [10,11]

	Concentrations (mM)							
	Na^+	K^+	Mg^{2+}	Ca^{2+}	Cl^-	HCO_3^-	HPO_4^{2-}	SO_4^{2-}
SBF	142.0	5.0	1.5	2.5	148.8	4.2	1.0	0.5
Blood plasma	142.0	5.0	1.5	2.5	103.0	27.0	1.0	0.5

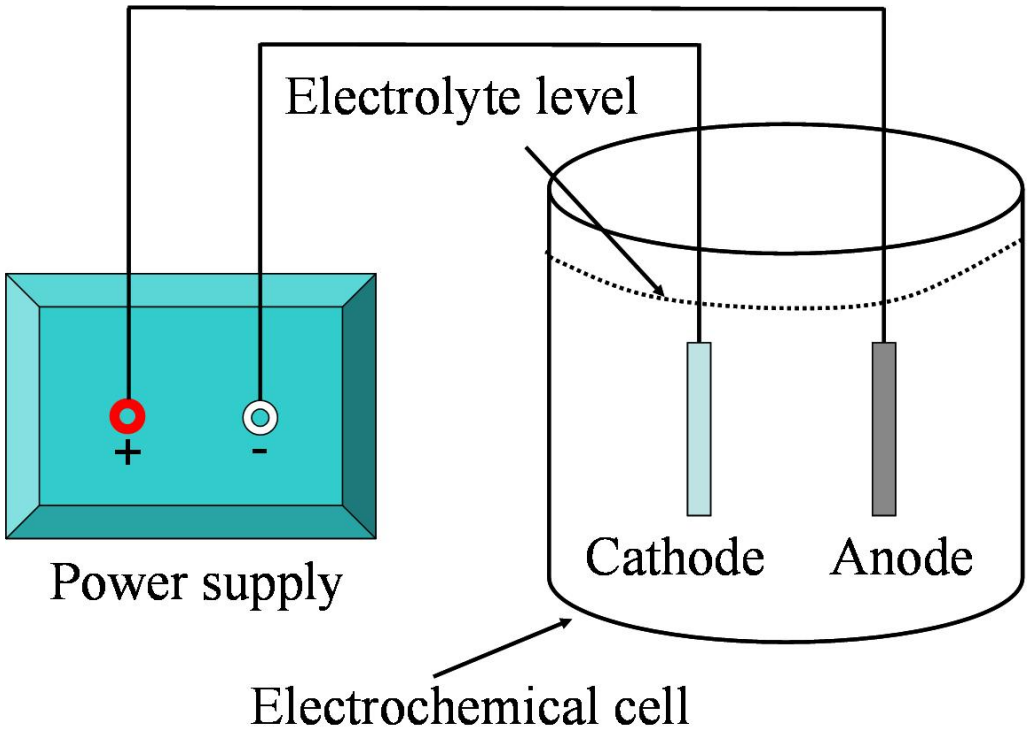

Figure 3-1 Schematic diagram of setup for electrochemical anodization of zirconium dioxide nanotubular arrays.

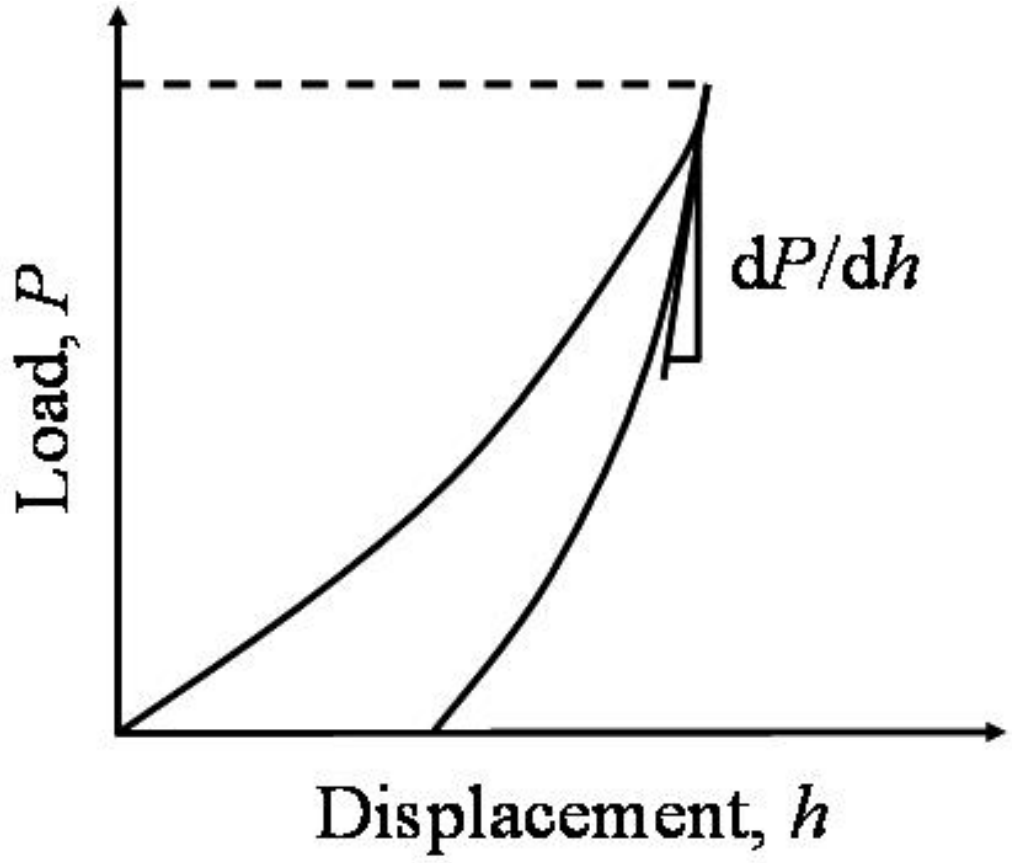

Figure 3-2 Schematic of load-displacement curve for an instrumented microindentation test.

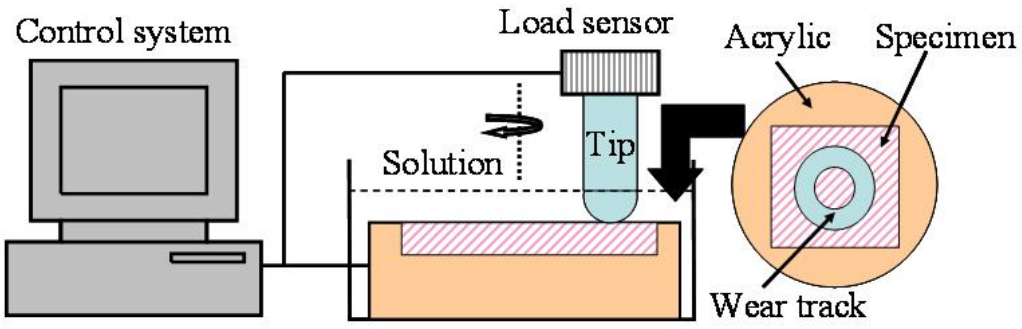

Figure 3-3 Schematic diagram of the setup for scratch test by applying UMT.

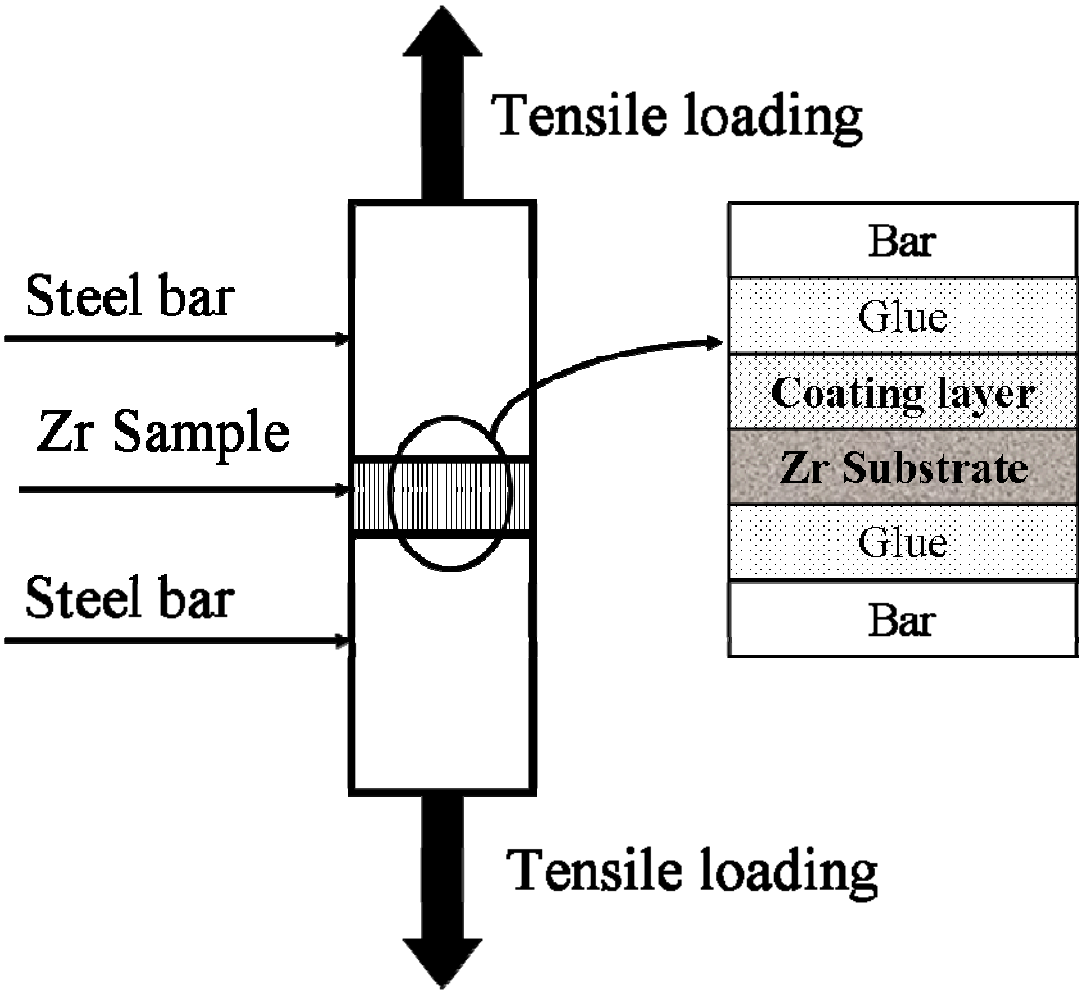

Figure 3-4 Schematic of the bonding strength test of the HA coating to the substrate.

References

[1] S. Berger, J. Faltenbacher, S. Bauer, P. Schmuki, Enhanced self-ordering of anodic ZrO_2 nanotubes in inorganic and organic electrolytes using two-step anodization, Phys. Status Solidi-RRL. 2 (2008) 102-104.

[2] J. I. Goldstein, D. E. Newbury, D. C. Joy, C. E. Lyman, P. Echlin, E. Lifshin, L. Sawyer, J. R. Michael, Scanning electron microscopy and X-ray microanalysis, 3rd edition, Springer, New York, 2003.

[3] Surface Analysis by Auger and X-ray Photoelectron Spectroscopy, ed. J.T.Grant and D.Briggs, published by IM Publications, 2003, Chichester, UK.

[4] P. Griffiths, J. A. de Hasseth, Fourier Transform Infrared Spectrometry (2nd ed.), Wiley-Blackwell.

[5] D. B. Williams, C. B. Carter, Transmission electron microscropy: a text book for materials science, Springer, New York, 1996.

[6] Manual of Fisherscope H100C Microhardness Measurement System, Version 0.1, 2000.

[7] Manual of UMT-2 Multi-Specimen Test System, Version 1.01, 2004.

[8] H. M. Kim, F. Miyaji, T. Kokubo, T. Nakamura, Bonding Strength of Bonelike Apatite Layer to Ti Metal Substrate, J. Biomed. Mater. Res. (Appl. Biomater.) 38 (1997) 121–127.

[9] B. Feng, X. Chu, J. Chen, J. Wang, X. Lu, J. Weng, Hydroxyapatite coating on

titanium surface with titania nanotube layer and its bond strength to substrate, J. Porous Mater. 17 (2009) 453-458.

[10] T. Kokubo, H. Takadama, How useful is SBF in predicting in vivo bone bioactivity? Biomaterials 27 (2006) 2907-2915.

[11] L. Müller, F. A. Müller, Preparation of SBF with different HCO_3^- content and its influence on the composition of biomimetic apatite on anodic TiO_2 nanotubes. Acta Biomater. 2 (2005) 181-189.

Chapter 4 Fabrication and mechanical properties of anodized zirconium dioxide nanotubular arrays*

4.1 Introduction

In this chapter, a series of highly ordered, and vertically aligned ZrO_2 nanotubular arrays have been fabricated via anodization in fluoride containing electrolyte by changing the anodization voltage and period. We have studied the effect of changes in anodic oxidation duration and stimulated voltage on tube diameter and coating thickness. Microindentation was conducted to probe the mechanical properties, such as Young's modulus, hardness, and ratio of the elastic energy to the total deformation energy. Universal Micro-Tribometer (UMT) was applied to evaluate the wear resistance of the ZrO_2 nanotubular arrays in dry and wet conditions. Efforts were made to clarify the mechanism responsible for variations in mechanical properties with respect to the geometric features of ZrO_2 nanotubular arrays.

4.2 Results and discussion

4.2.1 Formation of ZrO_2 nanotubular arrays

ZrO_2 nanotubular arrays were formed on the zirconium substrate by anodization

* Part of material in this chapter has been published in:
L.N.Wang and J.L.Luo, J. Phys. D. App. Phys. 44 (2011) 075301 (8 pp).

with different time under different voltages in order to systematically investigate the variation of tube length and tube diameters under different conditions. Figure 4-1 portraits the typical SEM images of top view, bottom view, and cross-section view of the arrays anodized at 30 V for 24 hrs as well as the Zr substrate by removing the arrays. Top view and cross-section view show the highly ordered nanotubular structure with an average individual inner diameter of 50 nm and tube wall about 10 nm. The length of the tube arrays is about 12 μm, resulting in the length-to-width aspect ratio of 240. The higher magnification inserted image in Figure 4-1c illustrates that the individual tube is very smooth and all the tubes has similar tube diameter and wall thickness. It is also found out that the diameter and wall thickness of tubes anodized at 30 V but with different times do not significantly change, implying that these two parameters may be independent of anodization time. Figure 4-1d shows the TEM image and the diffraction pattern of the as-formed tubes. It reveals that the tube is amorphous.

By analyzing the FE-SEM images of the top view and cross-section view of tubular arrays, a relationship of the tube thickness versus anodization time is established and the results are illustrated in Figure 4-2. It can be demonstrated that the growth of the tubes can be split into two regions according to the growth rate characteristics. There is an obvious thickness increasing region in the first 10 hrs. After 10 hrs anodization, the thickness slightly increases until 12 hrs and becomes relatively unchanged from 12 hrs to 24 hrs. Therefore, an equilibrium thickness

region can be defined for the region after 10 hrs. Additionally, the top view at 4 hrs anodization and 24 hrs anodization indicates that the nanotubular diameter keeps same value under the constant anodization voltage.

The stimulated voltage is another parameter affecting the formation of the ZrO_2 nanotubular arrays. The effect of stimulated voltage on the tubular arrays was also examined by varying the voltage from 15 V to 30 V with 24 hrs of the anodization periods. The resulting ZrO_2 nanotubular arrays were observed FE-SEM. Figure 4-3 shows the curve that illustrates the relationship between nanotubular array thickness and anodizing voltage. The result demonstrates that the thicknesses grow with the increasing of the anodized voltage, which is understandable since the high anodic voltage will speed up the oxidation rate of the Zr foil, accelerating the formation of ZrO_2 nanotubular arrays.

Although the exact mechanism of the formation of ZrO_2 nanotubular arrays is still the subject of some debate, it is well established that the formation of ZrO_2 nanotubular arrays in F^- containing electrolyte is the result of three simultaneous processes: 1) electric field-assisted oxidation of Zr substrate to form zirconium oxide, 2) electric field-assisted dissolution of the zirconium oxide and 3) chemical dissolution of zirconium oxide [1-4]. These processes can be expressed by the following possible reactions [4]:

$$Zr^{4+} + 2O^{2-} \rightarrow ZrO_2. \quad (4.1)$$

$$H_2O \rightarrow 2H^+ + O^{2-} \quad (4.2)$$

$$Zr^{4+} + 4OH^- \rightarrow Zr(OH)_4 \quad (4.3)$$

$$Zr^{4+} + 2H_2O \rightarrow ZrO_2 + 4H^+ \quad (4.4)$$

$$6F^- + ZrO_2 + 4H^+ \rightarrow [ZrF_6]^{2-} + 2H_2O \quad (4.5)$$

The detailed process of the growth of highly ordered nanotubular arrays, somehow is still not very clear. Nevertheless, it is widely accepted that three processes can be derived from the growth procedure: 1) the formation of the initial barrier oxide layer, 2) the formation of the uniformly distributed nanopores, and 3) separation of the interconnection of the pores into nanotubes [4-6]. Moreover, further studies are required to fully clarify the mechanism of the growth of highly ordered ZrO_2 nanotubular arrays.

4.2.2 Microindentation on ZrO_2 nanotubular arrays

Mechanical properties of the ZrO_2 nanotubular arrays were evaluated via a microindentation for the information of the local hardness (HV), apparent Young's modulus (Y), maximum depth (H_{max}), and elastic behaviour. The elastic behaviour was characterized using the ratio of elastic deformation energy (W_e) to the total deformation energy (W_{tot}). It is well known that in the nanoindentation system, when the indentation depth is smaller than 10 % of the thickness of a film, the influence of the substrate on the measurement of the mechanical properties of the film might be neglected [7]. In present study, a light load of 25 mN was applied for the microindentation test in order to minimize the effect of substrate on the nanotubular arrays. We firstly examine the nanotubular arrays formed under

constant voltage, i.e. 30 V but different anodization time. By calculating the aspect ratio, Figure 4-4 shows the effect of aspect ratio under same anodization voltage on the mechanical properties of nanotubular arrays. As shown in Figure 4-4a. 4b, and 4c, the apparent Young's modulus, W_e/W_{tot}, and hardness all decrease. The apparent Young's modulus decreases from 62.2 to 29.6GPa when the aspect ratio of ZrO_2 nanotubular arrays increases from 68 to 160 μm. The hardness and W_e/W_{tot} also sharply decreases from 52.5 to 9.9 and from 38.5% to 10%, respectively. Once the aspect ratio exceeds 180, the hardness keeps decreasing to 5.8 and the ratio of W_e/W_{tot} reaches a stable value about 6 %. On the other hand, the H_{max} increases with the enhancement of aspect ratio, which corresponds to a thicker nanotubular arrays. This result indicates that thicker nanotubular arrays are softer than their thinner counterparts.

Similarly, the apparent mechanical properties of ZrO_2 nanotubular arrays with different thickness under different anodization voltages are shown in Figure 4-6. As the aspect ratio increases, the H_{max} increases since the thickness increases. Consequently, the apparent Young's modulus, W_e/W_{tot}, and hardness decreases, similar to the changes shown in Figure 4-6. It should be pointed out that, since ZrO_2 nanotubular arrays fabricated at the lowest voltage (15 V) are very thin, the measurement of mechanical properties could be more or less influenced by the substrate, and the obtained results may somewhat deviate from the real values. However, the general tendency of the variation of mechanical properties of the

nanotubular arrays film is consistent with that of samples fabricated at 30 V (see Figure 4-4).

It is found out that the anodization time and the anodic voltage do not show significant influences on the wall thickness and slightly affect the opening diameter of the tubes. However, the thickness of the nanotubular arrays varies under different anodization time and anodic voltage. Thus, the variations of mechanical properties with respect to the anodization time and anodic voltage, which influences the thickness of the nanotubular arrays, could be ascribed to the deformation behaviour of the tubular arrays, such as buckling and densification, under the indentation force. The deformation of the region with nanotubular arrays right under indentation force can be described as densification due to the collapse of the nanotubes, in which the buckling of the nanotubes might play an important role. Similar to the thin wall shells with one ends open, when the nanotubes are subjected to an axial compressive load, the tubes will begin to fail with the buckling, followed by fracture [8]. The critical load at failure for a clamped simple support column is expressed as following equation [9]:

$$P_{cr} = \frac{2\pi^2 EI}{L^2} \tag{4.6}$$

where P_{cr} is the critical load, E is the modulus of elasticity, I is the moment of inertia of the cross section about the axis of bending, and L is the length of the column. As discussed above, the main difference among the nanotubes in present

study is their thickness, i.e. length, E and I could be assumed to be the same value. Therefore in Eq. 4.6, the P_{cr} is inversely proportional to the L^2, which indicates the longer the column, the smaller the critical load. The long nanotubular arrays are easier to fail than the shorter ones. It should be noticed that the nanotubes in the arrays were constrained by the neighboring tubes, which were deformed in a similar manner. Thus the Eq. 4.6 is only applied to qualitatively explain the poor mechanical behaviour of the longer nanotubular arrays rather than quantitatively predict the failure process. After the buckling stage, when the compressive force is further applied to nanotubular arrays, the arrays are crushed down and results in the densification as shown in Figure 4-6 It can be summarized from the results of microindentation test that the thicker ZrO_2 nanotubular arrays, fabricated with higher anodic voltage or longer anodization time, are with weaker apparent mechanical properties.

From the above analysis, it is still difficult to obtain the precise value of the mechanical parameters, such as Young's modulus of ZrO_2 nanotubular arrays themselves. Nevertheless it is well known that the modulus of ceramic materials decreases with increases in porosity [10]. Several researchers have proposed theoretical models to predict the effect of porosity on the elastic properties of ceramic materials [10-12]. One of the simplest models is the commonly used for continuous fiber reinforced composites [13]. It assumes an isostrain condition (longitudinal loading, parallel to the fibers) or isostress condition (transverse

loading, perpendicular to the fibers). By taking the cylindrical porous part in tubes as the null fibers, Crawford et al. derived that the Young's modulus of the porous tube structure (E_c) may be derived by a simple equation [14]:

$$E_c = E_m(1 - P) \tag{4.7}$$

where E_m is the matrix material and P is the fraction of porosity. In present study, it can be assume the volume fraction of pores in the ZrO_2 nanotubular arrays is approximately 75% (from image analysis of Figure 4-1a) and a modulus for ZrO_2 of 100-200 GPa (for solid materials) [15]. By applying Eq. 4.7, it yields a Young's modulus of ZrO_2 nanotubular arrays with the porosity in the present study of approximately 25–50 GPa. Our result for the longest array is about 29.6 GPa, which is within the range for the calculation. Since there is buckling and densification during the deformation of the test, our result for the measurement of Young's modulus of ZrO_2 nanotubular arrays seems reasonable. One can also compare our results with the Zr substrate, 88 GPa [15], that ZrO_2 nanotubular arrays have a significantly lower value of Young's modulus than that of the metal.

4.2.3 Microscratch on ZrO_2 nanotubular arrays

Microscratch tests were also performed to evaluate the resistance of the ZrO_2 nanotubular arrays to scratch damage. During the scratch tests, a tungsten carbide tip scratched a ZrO_2 nanotubular array film under a linearly increasing load with *in situ* monitoring variations in CER. Since ZrO_2 is a semiconductor, ZrO_2 nanotubular array film has a higher electrical resistance than the Zr substrate. The

scratch tip touches the metal substrate, resulting in a sharp drop of CER once the ZrO_2 nanotubular array film is broken during scratching. The critical normal load corresponding to the drop of CER reflects the minimum scratch load that causes failure of the ZrO_2 nanotubular array film. Critical loads for ZrO_2 nanotubular array films fabricated under various conditions are summarized in Table 4-1.

Table 4-1 Critical Load for Nanotubular Arrays Fabricated under Various Conditions

No.	Voltage (V)	Time (h)	Thickness (μm)	Critical load (N)
1	30	1	3.7 ± 0.22	2.0 ± 0.8
2	30	2	5.6 ± 1.18	2.4 ± 0.5
3	30	4	8.3 ± 1.58	2.8 ± 1.1
4	30	8	10.3 ± 0.98	3.5 ± 0.9
5	30	12	12.0 ±0.85	4.1 ± 1.6
6	30	24	12.6 ± 1.01	4.1 ± 1.4
7	15	24	6.0 ± 1.16	2.5 ± 0.9
8	20	24	7.0 ± 1.03	2.6 ± 1.1
9	25	24	8.6 ± 1.13	3.1 ± 1.2

It can be seen that the critical loads on nanotubular arrays depended on the thickness of the array film rather than the hardness or apparent Young's modulus of the nanotubular arrays. The thicker the ZrO_2 nanotubular array film, the higher is its resistance to scratch. On the basis of the results of microindentation and scratch test, it has to be emphasized that the higher scratch resistance of a thicker ZrO_2

nanotubular array film does not indicate a stronger film. It can only demonstrate that a thicker nanotubular array film makes the scratch tip more difficult to penetrate the damaged film to contact the substrate.

In order to evaluate the sliding wear resistance of the ZrO_2 nanotubular arrays, we tested the ZrO_2 nanotubular arrays in various environments: air, and water at pH 2.5, 7, and 13. Typical wear tracks of ZrO_2 nanotubular array films tested in air and in water at pH 13 are illustrated in Figure 4-7a and 4-7b, respectively. The wear tracks are smooth with clear edges. The width of the track is also determined by measuring the distance between two edges of the wear track. Results of the track width are presented in Figure 4-7c. As shown in Figure 4-7c, the width of wear track caused by sliding wear in water at various pH levels were lower than that in air and decreased as pH increased from 2.5 to 13. Since the volume loss due to wear is proportional to the width of wear track [16], it also can be deduced that variation of the volume loss is with the same sequence of the width of wear track. The difference of the width of wear track is ascribed to the lubrication effect of water, which could reduce friction, demonstrated by the decrease in frictional force with respect to the pH values observed during sliding wear tests, as shown in Figure 4-8d. The changes of the frictional force may well explain the variations in width of wear track of ZrO_2 nanotubular array films during sliding wear in different cultures. Compared to those observed during the sliding wear tests in air, the frictional forces observed during wear tests in water were significantly decreased, resulting in

smaller mechanical forces to cause wear of the ZrO_2 nanotubular array film.

The small differences in frictional force caused by sliding wear in water at various pH levels may be caused by different electrostatic properties of ZrO_2 at different pH level. Similar as other valve metal oxide such as TiO_2, ZrO_2 is amphoteric and it can be hydrolyzed into ‖Zr-OH in water [7], in which '‖Zr' represents the bulk materials and –OH represents a hydrolyzed surface in neutral solution. In different pH conditions, two relevant reactions may occur.

In acidic conditions:

$$\text{‖Zr-OH} + H^+ \leftrightarrow \text{‖Zr-OH}_2^+ \quad (4.8)$$

In alkaline solution:

$$\text{‖Zr-OH} + OH^- \leftrightarrow \text{‖Zr-O}^- + H_2O \quad (4.9)$$

In acidic solution, ‖Zr-OH reacts with H^+ to form ‖Zr-OH_2^+, forming a positively charged surface. In alkaline solution, ‖Zr-OH reacts with OH^- to form ‖Zr-O^-, resulting a negative charge surface in alkaline conditions [7]. The isoelectric point (pH_{iep}) of ZrO_2 in water has been widely reported to be in the range of 4-10 [17]. Therefore, at pH 2.5, the surface of ZrO_2 is positively charged as ‖Zr-OH_2^+, whereas it is negatively charged as ‖Zr-O^-at pH 13. Shyue et al. [18] studied the force interaction between atomic force microscopy (AFM) tip and the ZrO_2 particles in aqueous solutions over a wide range of pH values using AFM. They found out that the interaction between the AFM tip and the ZrO_2 is slightly positive charged at pH=2.5 and negatively charged at pH=9.7. They also found out that the

interaction between tip and ZrO_2 changed from attraction to repulsion as the pH value increased. Therefore, in the present study, the higher frictional force at pH 2.5 in water could be ascribed to the attractive interaction between the silicon nitride ball tip and the ZrO_2 nanotubular array film, whereas the frictional force decreased at pH 7 and pH 13, resulting from the change in the interaction from attraction to repulsion. The increased frictional force could enhance the wear attack. The above-mentioned studies reported in literature may explain the phenomenon observed in our study. Further work is required to clarify the mechanism of the wear behaviour of ZrO_2 nanotubular arrays in different culture.

4.4 Conclusions

A series of ZrO_2 nanotubular arrays with different thicknesses are fabricated by varying the anodic voltages and anodization periods in fluoride containing electrolyte. The thickness of the nanotubular array films highly depends on the anodic voltage and anodization duration. The tube opening slightly increases with the interval of the anodic voltage but not the anodic duration.

The growth of ZrO_2 nanotubular arrays at 30V shows two regions in the 24 hrs anodization time: a thickness increasing region within the first 8hrs and an equilibrium thickness region from 10 hrs to 24 hrs. Compared to the anodization time, the anodic voltage played a more important role in the formation of ZrO_2 nanotubular arrays. The growth of ZrO_2 nanotubular arrays was accelerated with

increasing anodic voltage.

Microindentation tests demonstrate that the apparent Young's modulus, W_e/W_{tot}, and hardness decreases as the ZrO_2 nanotubular array film become thick. However, the resistance to the scratch of the nanotubular array film does not depend on the mechanical parameter such as hardness and apparent Young's modulus, but only depends on the thickness of the film.

The resistance of ZrO_2 nanotubular arrays to sliding wear in water is lower than that in air. In the culture of water, the resistance to sliding wear in acidic water is lower than that in alkaline and neutral water due to the change from attractive interaction to repulsion between the tip and the ZrO_2 nanotubular array film as the pH value is increased from pH 2.5 to pH 13. The difference of the force in different pH level may be explained by the electrostatic property of ZrO_2 in water with varied pH environments.

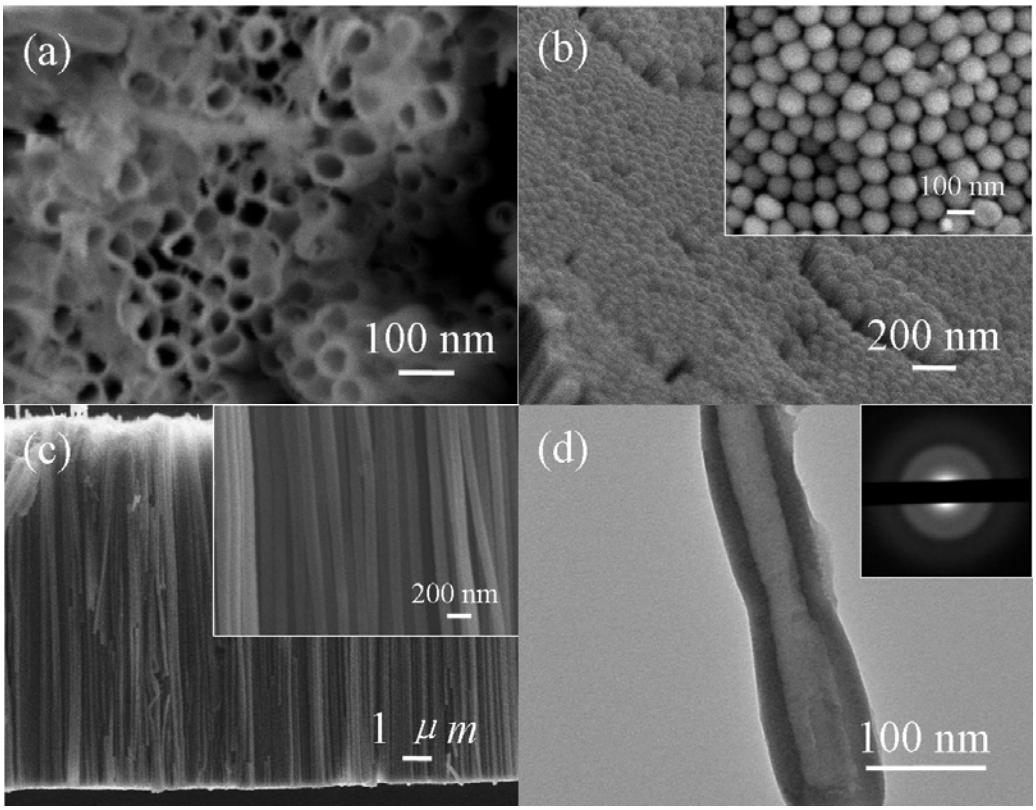

Figure 4-1 FE-SEM images of ZrO_2 nanotubular arrays fabricated at 30 V for 24 hrs: (A) top view, (B) bottom view, (C) cross-sectional view and the inserted image of the magnified view, and (D) TEM image of ZrO_2 nanotube and the inserted image of the diffraction pattern.

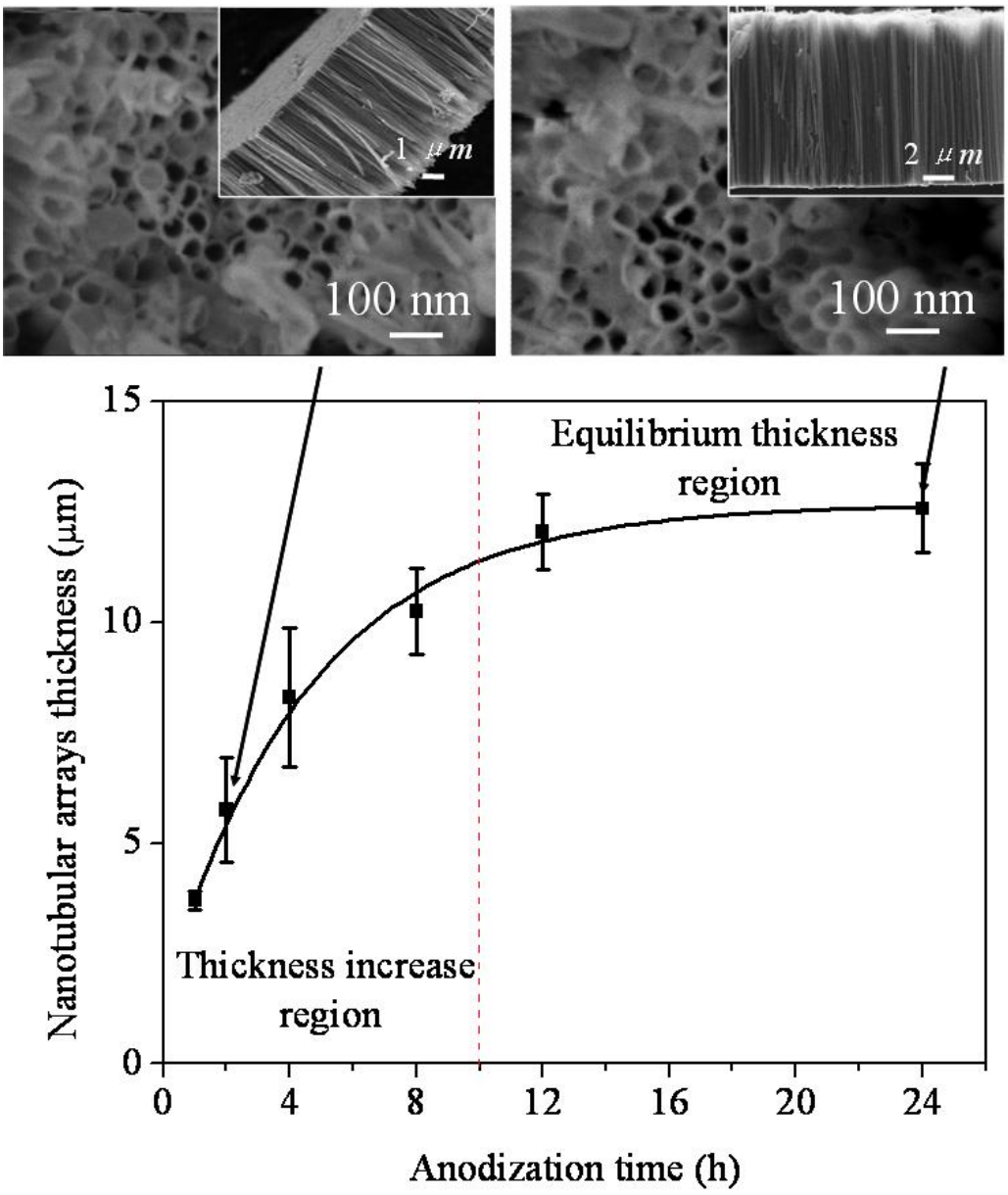

Figure 4-2 The growth curve of ZrO_2 nanotubular arrays fabricated at 30 V. The SEM images show the nanotubular opening and thickness at 4 hrs and 24 hrs anodization.

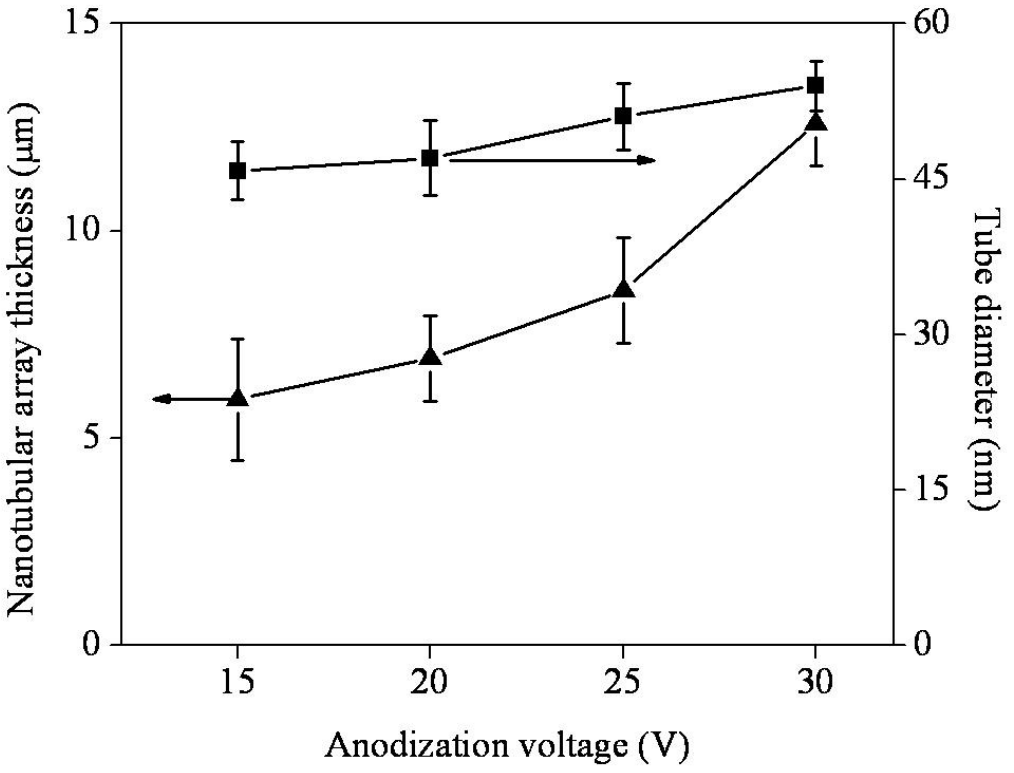

Figure 4-3 The comparison of nanotubular array thickness and diameter at different anodized voltage for 24 hrs anodization.

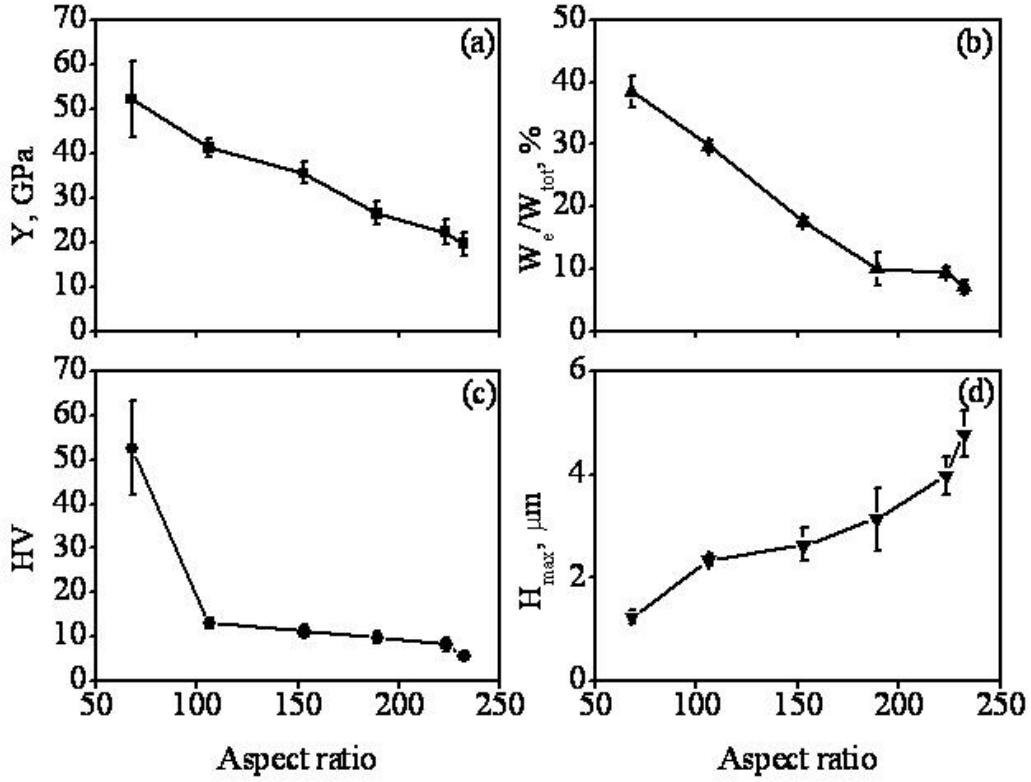

Figure 4-4 Mechanical properties of a series of ZrO_2 nanotubular arrays fabricated at 30 V with various anodization durations: (a) apparent Young's modulus (Y), (b) ratio of elastic energy (W_e) to total energy (W_{tot}), (c) hardness (HV), and (d) maximum depth (h_{max}). The aspect ratio of each nanotubular arrays was used to illustrate the relationship.

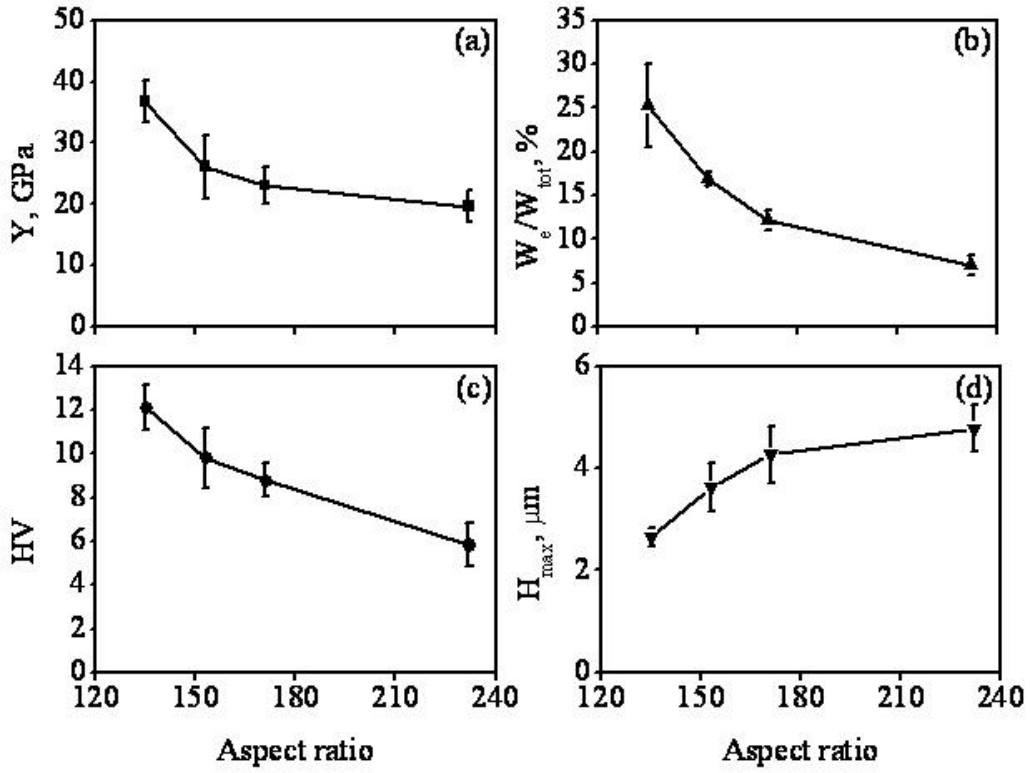

Figure 4-5 Mechanical properties of a series of ZrO_2 nanotubular arrays fabricated at 15 V, 20 V, 25 V, and 30 V in 24 hrs duration: (a) apparent Young's modulus (Y), (b) ratio of elastic energy (W_e) to total energy (W_{tot}), (c) hardness (HV), and (d) maximum depth (h_{max}). The aspect ratio of each nanotubular arrays was used to illustrate the relationship.

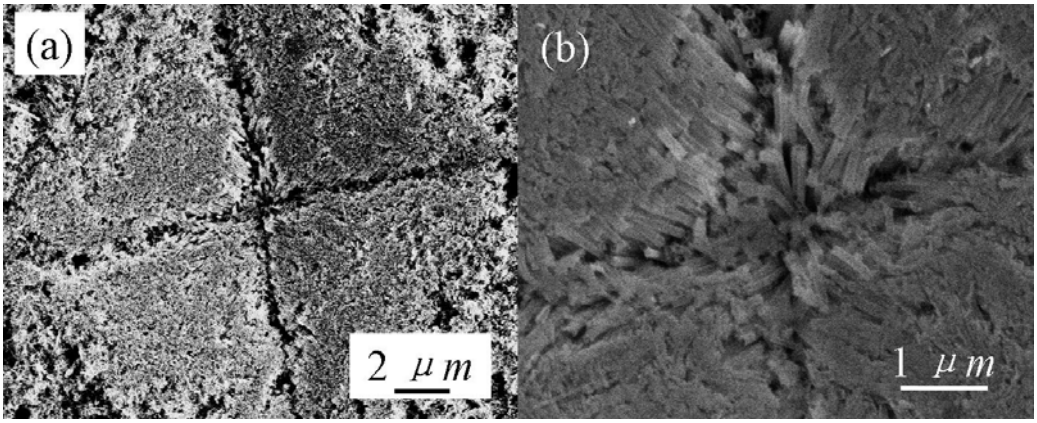

Figure 4-6 FE-SEM images: (a) typical microindentation on the surface of ZrO_2 nanotubular arrays; and (b) the magnified image showing the deformation and densification of the nanotubes.

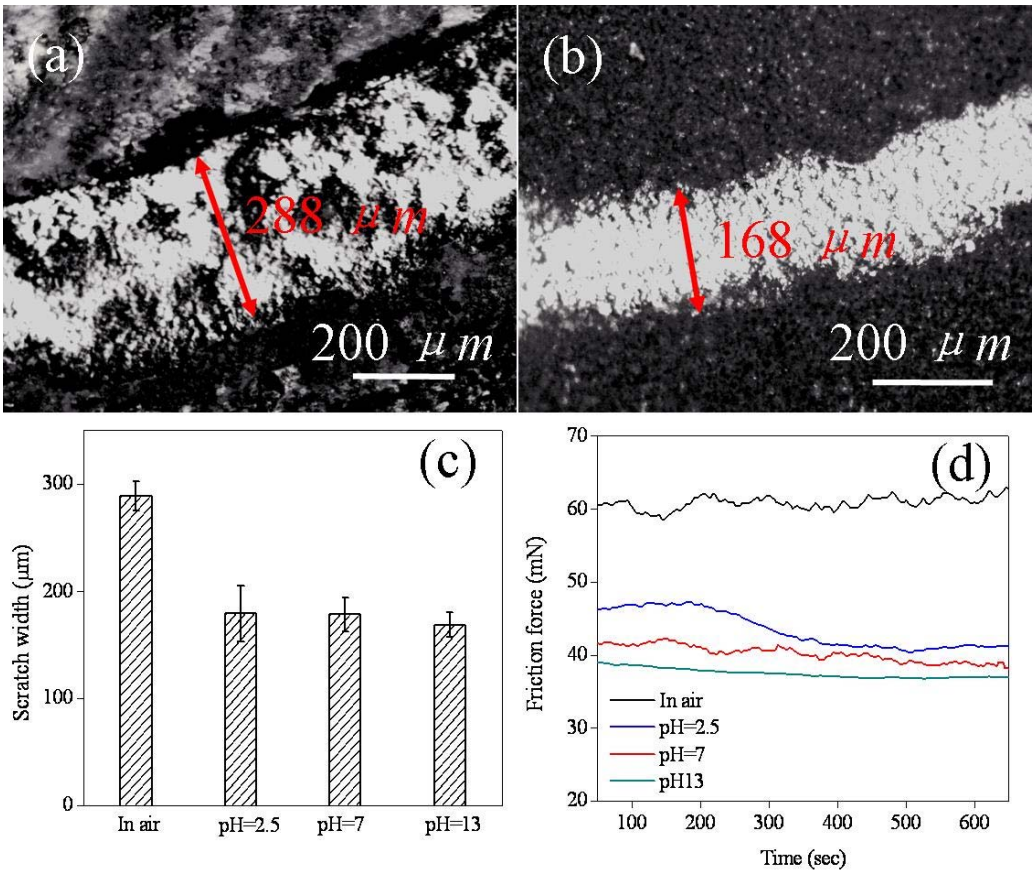

Figure 4-7 (a) The scratch track by sliding the nanotubular layer in air, (b) the scratch track by sliding the nanotubular layer in pH=13 solution, (c) the comparison of the width of the scratch track obtained under different conditions, and (d) the friction force curves versus time under different conditions.

References

[1] W. J. Lee, W. H. Smyrl, Zirconium Oxide Nanotubes Synthesized via Direct Electrochemical Anodization, Electrochem. Solid-State Lett. 8 (2005) B7-B9.

[2] L. Guo, J. Zhao, X. Wang, R. Xu, Z. Lu, Y. Li, Bioactivity of zirconia nanotube arrays fabricated by electrochemical anodization, Mater. Sci. Eng. C 29 (2009) 1174-1177.

[3] R. Huiskes, H. Weinans and B. Vanrietbergen, The relationship between stress shielding and bone-resorption around total hip stems and the effects of flexible materials, Clin. Orthop. Relat. Res. 274 (1992) 124-135.

[4] J. Zhao, R. Xu, X. Wang, Y. Li, In situ synthesis of zirconia nanotube crystallines by direct anodization, Corr. Sci. 50 (2008) 1593-1597.

[5] G. K. Mor, O. K. Varghese, M. Paulose, N. Mukherjee, C. A. Grimes, Fabrication of tapered, conical-shaped titania nanotubes. J. Mater. Res. 18 (2003) 2588-2593.

[6] X. Xiao, R. Liu, T. Tian, Preparation of bioactive titania nanotube arrays in HF/Na_2HPO_4 electrolyte, J. Alloys Comp. 466 (2008) 356-362.

[7] X. Tang, D. Li, Fabrication, geometry, and mechanical mroperties of highly ordered TiO_2 nanotubular arrays, J. Phys. Chem. C. 113 (2009) 7107-7113.

[8] S. J. Cox, C. Maeve McCarthy, The shape of the tallest column, Siam. J. Math. Anal. 29 (1998) 547-554.

[9] A. P. Boresi, R. J. Schmidt, Advanced Mechanics of Materials 6th ed.; John Wiley & Sons, Inc.: New York, 2003.

[10] R. W. Rice: Microstructure dependence of mechanical behavior of ceramics. In: MacCrone RK, editor. Treatise on materials science and technology, vol. 11, Academic Press, New York, 1977.

[11] K. K. Chawla: Composite materials science and engineering. Springer, New York, 1998.

[12] R. W. Rice: Mechanical properties of ceramics and composites, Marcel Dekker, New York, 2000.

[13] Z. Hashin, B. W. Rosen, The elastic moduli of fiber reinforced materials, J. Appl. Mech. 31 (1964) 223-232.

[14] G. A. Crawford, N. Chawla, K. Das, S. Bose, A. Bandyopadhyay: Microstructure and deformation behavior of biocompatible TiO_2 nanotubes on titanium substrate, Acta Biomater. 3 (2007) 359-367.

[15] http://www.azom.com/details.asp?articleid=133, access on April 16th, 2010.

[16] T. Adachi, Anion exchange separation of hard acid-metals using HF-H_3BO_3 media, Bull. Chem. Soc. Jpn. 55 (1982) 802-808.

[17] M. Kosmulski, Chemical Properties of Material Surfaces. New York: Marcel Dekker, 2001.

[18] J. Shyue, Y. Tang, M. R. De Guire, Forces between nitrogen-containing self-assembled monolayers (SAMs) and zirconia particles in aqueous solutions, J.

Mater. Chem. 15 (2005) 323-330.

Chapter 5 Enhancement of the capability of hydroxyapatite formation on anodic ZrO_2 nanotubular arrays via an effective chemical dipping treatment*

5.1 Introduction

In this section, ZrO_2 nanotubular arrays with different geometry were fabricated by electrochemical anodization. The as-formed specimens were then treated using the dipping method. Samples were immersed in SBF for different times to determine the relationship between time of immersion and rate of HA coating formation on the treated nanotubular layers. The amount of HA deposited were quantitatively determined from the layer thickness of the HA formed and the nanotubular dimensions. In addition, the bonding strength between the HA coating and ZrO_2 nanotubular arrays was measured to determine whether the coating has mechanical properties appropriate for clinical applications.

5.2 Experimental solution and comparison specimen

5.2.1 Dipping treatment of ZrO_2 nanotubular arrays

An accelerated calcium solution (ACS) was prepared by dissolving reagent

* Material in this chapter has been accepted by: J. Biomed. Mater. Res. B Appl. Mater.

grade NaCl, $CaCl_2$, and $KHPO_4$ in 1 L DI water (Table 5-1) [1]. The pH was adjusted to 7.4 by adding appropriate amount of 1 M HCl and tris(hydroxymethyl)aminomethane (tris). The anodically treated specimens were exposed vertically into ACS for approximately 10 s then withdrawn from the solution, leaving a wetting film on the surface. The samples were placed on a slide glass and left to dry in a compressed air stream for 10 min at room temperature. Every sample was treated up to eight times followed by rinsing in DI water and drying in an air stream. The process of the dipping method is shown in Figure 5-1.

Table 5-1 Ion Concentrations in ACS and SBF. [1-3]

	Concentrations (mM)							
	Na^+	K^+	Mg^{2+}	Ca^{2+}	Cl^-	HCO_3^-	HPO_4^{2-}	SO_4^{2-}
ACS	136.8	3.71	-	3.10	144.5	-	1.86	-
SBF	142.0	5.0	1.5	2.5	148.8	4.2	1.0	0.5

5.2.2 Comparison samples

For comparison purposes, some ZrO_2 nanotubular arrays were then annealed with a heating rate of 10 ^oC/min at 200 ^oC for 1 h [4]. These samples were then soaked in SBF to evaluate and compare their HA formation capability with that of the unannealed samples.

5.3 Results

5.3.1 Fabrication of ZrO_2 nanotubular arrays

Figure 5-2 shows examples of ZrO_2 nanotubular arrays anodized for 20 min under different applied voltages, 50 V (Figure 5-2a; bottom view shown in Figure 5-2d), 32 V (Figure 5-2b), and 20 V (Figure 5-2c). The inserted images are top view of the tubular arrays. The openings of the tubes are homogenously distributed over all the surfaces. It is apparent from Figure 5-2 that the nanotubes are open at the top while at the bottom they are closed. The diameters of the nanotubular openings and the layer thickness each decreased with the decline of the applied voltage. The effect of applied voltage and anodization time on the geometric factors, such as tube opening and tube layer thickness, is summarized in Figure 5-3. Figure 5-3a shows the influence of applied voltage on nanotubular diameter and nanotubular layer thickness. As the voltage increased from 20 – 50 V, the tube diameter increased from 35 nm to 80 nm, while the layer thickness increased from 1.79 μm to 3.80 μm. Thus the nanotubular diameters and layer thicknesses varied linearly with the applied potential, in agreement with other's report [5]. The results demonstrated that the layer thickness increased with increase in the anodizing voltage, which is understandable since an increase in anodic voltage will speed up the oxidation rate of the Zr foil, thus accelerating the formation of ZrO_2 nanotubular arrays. Figure 5-3b shows the kinetic curves for formation of nanotubular arrays under different

applied voltages, showing a linear relationship between the nanotubular layer thickness and applied voltage for a given time. The growth rate of the nanotubular arrays increased as the applied voltage increased from 20 V to 50 V. These data show a similar tendency to those of Lee et al. [6] though there was a different growth rate due to differences between electrolytes used in the two studies. Although the exact mechanism of the formation of ZrO_2 nanotubular arrays is still the subject of debate, it is well established that the formation of ZrO_2 nanotubular arrays in F- containing electrolyte is the result of three simultaneous processes: 1) electric field-assisted oxidation of Zr substrate to form zirconium oxide, 2) electric field-assisted dissolution of the zirconium oxide and 3) chemical dissolution of zirconium oxide. While the detailed processes of the growth of highly ordered nanotubular arrays still is unclear [7, 8], it is widely accepted that three processes can describe the growth procedure: 1) the formation of the initial barrier oxide layer; 2) the formation of the uniformly distributed nanopores; and 3) separation of the interconnection of the pores into nanotubes [9-11]. Moreover, further studies are required to fully clarify the mechanism of the growth of highly ordered ZrO_2 nanotubular arrays.

5.3.2 Dipping treatment on ZrO_2 nanotubular arrays

ZrO_2 nanotubular arrays anodized at 50 V for 20 min were used to investigate the effect of dipping treatment (Figure 5-2a). The treatment led to formation of crystallites growing from the inside surfaces of the tubular arrays. Figures 5-4a and

5-4b shows a top view of the nanotubular arrays after 4 and 8 times dipping treatment in ACS, respectively. The arrows in Figure 5-4a indicate examples of filled tubes containing tiny particles both inside and at the opening pores. After 8 times dipping, most of the opening pores were filled with deposited crystallites. EDX spectra of the top surface of samples after 4 and 8 times dipping were obtained to identify the chemical composition of the crystallites (Figure 5-4c). Ca peaks were detected after 4 times dipping and a larger amount of Ca was detected after 8 times dipping. Since the P peak overlapped the Zr peak in EDX, XPS was performed to determine the presence of P after 8 times dipping (Figure 5-4d). The XPS spectrum of P showed that the deposit was calcium phosphate (CaP) crystallites. The Ca amount also was determined to explore the effect of the dipping treatment. Generally, an increase of the dipping times leads to more CaP deposits on the ZrO_2 nanotubular arrays (Figure 5-4e). After 8 times dipping, the Ca amount was about 2.16 at%.

5.3.3 Formation of HA on dipping treated ZrO_2 nanotubular arrays

Figures 5-5a – 5-5d show top view SEM images of the dipping treated nanotubular arrays formed under 50 V applied voltage, after immersion in SBF for 1, 2, 4, and 8 days, respectively. It can be seen from Figure 5-5a that there were deposits on the surface after 1 day of immersion. After 2 days of immersion there was full coverage of the surface with formation of agglomerations. After 4 days, the deposited layer became denser. The 8 days of immersion resulted in a thick and

dense coating with small agglomerations, shown in the inserted image. Figure 5-5e presents the EDX spectrum of the sample shown in Figure 5-5d. A high intensity Ca peak was detected, which showed that a thick CaP layer was generated after only 8 days immersion in SBF. The side view of the coating layer can be seen in Figure 5-5f, which shows that the deposited layers had grown together to form a compact layer with about 5 μm thick.

In order to address the effect of the geometrical factors of nanotubular arrays on the dipping treatment and as-formed deposits layer, a series of nanotubes with different diameter but similar length were prepared. Figure 5-6a shows the mass increments for nanotubes having the same length, 3.79 μm but different tubular diameter, ranging from 33 nm to 80 nm. After 2 days soaking in SBF there was an approximately four-fold difference in mass between the 33 nm and 80 nm tube coatings. After 8 days of soaking, the difference increased to an eight-fold enhancement in deposition on the 80 nm diameter nanotubes. A series of nanotubular arrays formed under constant 50 V with the geometrical factors shown in Figure 5-2b also were evaluated to determine the dependence of deposition on tubular length. In Figure 5-6a mass gain measurements are shown for tubes having the same diameter, 80 nm, but different lengths in the range 0.5-3.79 μm after immersion in SBF for up to 8 days. Figure 5-6b shows the mass gain after the dipping treatment and soaking the samples in SBF for different numbers of days. The results showed that the tube length affected not only the dipping treatment but

also the subsequent coating formation in SBF. As both the tube diameter and length play a role, it may be concluded that a key factor for coating formation is the available tube volume.

Another aspect that needs to be addressed is the comparison of coating formation on annealed and unannealed samples. Previous work indicated that hydroxyapatite formation was found when the tube layers were annealed to 200 ^{o}C [4]. Therefore, in order to investigate the effect of the dipping treatment on the annealed nanotubular arrays, ZrO_2 nanotubular arrays were annealed to 200 ^{o}C according to the process in earlier reports. Nanotubular arrays with and without dipping treatment were immersed in SBF for up to 8 days. Figure 5-7a - 5-7f shows the top surface and the corresponding EDX spectrum for ZrO_2 nanotubular arrays with dipping treatment (Figure 5-7a and 5-7b), as-formed ZrO_2 (Figure 5-7c and 5-7d), and annealed ZrO_2 nanotubular arrays (Figure 5-7e and 5-7f) after immersion in SBF for 8 days. For the control specimen, which was an annealed ZrO_2 nanotubular array without dipping treatment, there was higher capability for the formation of coating than for more amorphous nanotubular arrays. By comparing the EDX spectra, a higher intensity of Ca was found for the annealed specimen than for the more amorphous specimen. However, the dipping treatment still led to a significant enhancement of the amount of coating deposited. All amorphous and annealed ZrO_2 nanotubes which were dipping-treated became completely covered by deposition. Figure 5-7g compares the results of the mass

increment measurements for amorphous ZrO_2 nanotubular arrays and annealed ZrO_2 nanotubular arrays with and without dipping treatment after soaking in SBF for 2 and 8 days. For those without dipping treatment, the specimens are defined as control samples. In every case the dipping treatment provided a basis for enhancement of coating formation in SBF. The morphology of the deposited layers formed on the annealed nanotubes with dipping treatment was similar to that on the amorphous nanotubular arrays.

Figure 5-8 shows the XRD spectra of the surfaces developed over different immersion periods in SBF. Figure 5-8a shows the spectrum of the intact substrate before immersion in SBF. The HA was detectable using XRD after 2 days of immersion (Figure 5-8b). With prolongation of immersion time from 4 d to 8 days, the peaks of Zr gradually became weaker compared to those of HA, as shown in Figures 5-8c and 5-8d, which indicated that calcium and phosphate were deposited onto the surface, formed HA crystals, and that HA became thicker with immersion time. Figure 5-9 shows the FTIR spectrum of the HA coating after 8 days of immersion in SBF. The characteristic peaks of phosphate groups, molecular and adsorbed water, and hydroxyl groups were apparent in the spectrum, as summarized in Table 5-2 [12]. Moreover, carbonate bands also were detected at 875, 1420 and 1460 cm^{-1} [13]. Therefore the coating is carbonated HA.

Figure 5-10 is the XPS spectrum showing the chemical composition of the as-formed HA coating. Semiquantitatively, the ratio of Ca to P was 1.45. The

spectrum also showed peaks for Mg and Na. These data demonstrated that the composition of the HA coating was close in composition to that of physiological HA, in which the Ca:P ratio ranges between 1.35 and 1.46, and it contains small amounts of both Mg and Na [3].

Table 5-2 Characterization of materials from FTIR spectra. [12, 13]

Groups	Wavenumber of vibration peak (cm^{-1})
Bending mode of PO_4^{3-}	474, 567, and 604
Vibration of HPO_4^{2-}	875 and 958
Bending mode of CO_3^{2-}	875
Stretching mode of PO_4^{3-}	960-1200
Vibration of CO_3^{2-} on PO_4^{3-} lattice site	1420 and 1460
Bending mode of H_2O vibration	1645
Vibration of adsorbed H_2O	2500-3600

5.3.4 Bonding strength of HA coating

The bonding strength of the HA coating on ZrO_2 nanotubes after 8 days of immersion in SBF was evaluated using the method described in Section 2.4. The bonding strength of the HA coating on ZrO_2 nanotubes was 21.2 ± 1.6 MPa. Bonding strengths of HA coatings on Bioglass and glass-ceramic-A-W are less then 10 MPa [14]. Figure 5-11 compares bonding strengths determined in the present study with published data and the ISO standard value (Figure 5-11a), surface

morphology (Figure 5-11b), and the EDX mapping of Ca on the fracture surfaces of substrates (Figure 5-11c). The bonding strength for ZrO_2, 21.2 ± 1.6 MPa, is higher than the value of the ISO standard 13779-2:2008, 15 MPa [15], for HA coated surgical implants. From the EDX mapping, the intensity of the reflected Ca peak was strong on the fractured surface of the substrate, which indicated that the HA coating adhered well to the substrate and that fracture happened within the HA coating layer and not along the interface between HA and ZrO_2 nanotubes.

5.4 Discussion

It is clear from the above results that the formation of HA coating on ZrO_2 nanotubes was enhanced dramatically using the dipping treatment. The dipping treatment induced deposition of calcium phosphate crystallites on the surfaces of ZrO_2 nanotubular arrays. When a specimen was transferred into the SBF these crystallites not only served as nucleation site for HA formation, but also to make the surface highly concentrated with Ca and P, which then were converted rapidly to HA.

The mechanism of the process in the dipping treatment described herein probably was as described previously in discussion of an evaporation-induced process [5, 16]. Figure 5-12 shows one nanotube as an example to illustrate the process occurring during the dipping treatment. The dipping in ACS left a wetting film in the surface. Since the nanotubular structure had a small diameter a large

pressure differential was generated across the liquid interface, so the liquid had a high surface tension similar to water and produced a large pressure difference as described by the Young-Laplace equation [3]. Thus the liquid penetrated into the nanotubes due to the capillary effect. Consequently, the wetting film in-filled and covered the inner wall of the nanotubes (Figure 5-12a). During the drying step, the wetting film gradually evaporated resulting in an increasing level of concentration within the liquid medium in the tubes. The high concentration induced calcium and phosphate deposition to form CaP crystallites adhering to the inner wall of the ZrO_2 nanotubes (e.g. Figure 5-12b). During the drying process, other chemicals (the blue particles in this figure) such as NaCl, KCl, $CaCl_2$, and tris also accumulated during evaporation. Some CaP may also have reacted or interacted within the wetting film and so may not have remained adherent to the tubular wall. The next dipping step caused a portion of the chemicals to dissolve, some CaP particles to detach, and a new wetting film to form. The repeated dipping treatment thus formed CaP-crystallite-covered inner walls of ZrO_2 nanotubes. The surfaces then were ready for deposition of calcium and phosphate which was converted rapidly to HA once the samples were immersed in SBF. The obtained HA coating was carbonated-HA after 8 days of immersion in SBF. It has been suggested that carbonated HA is formed after immersion in CO_3^{2-} containing SBF. The vibration bands at 1420 and 1460 cm^{-1} showed that (CO_3^{2-}) was partly substituted for (PO_4^{3-}), resulting in the formation of B-type carbonated HA, which is predominant in

biological bone tissues [17-19].

The mechanical properties such as tensile bonding strength of the calcium phosphate coating to metallic implant substrate are important coating properties. As shown in Figure 6-11a, the HA coating on ZrO_2 nanotubes in this study had high bonding strength and was tightly bonded to the substrate, while the coating remained HA. EDX mapping of Ca also confirmed that the fracture of the coating happened within the HA coating, not between the layers. A schematic of the fracture of HA coating is shown in Figure 5-13.

The high bonding strength can be explained as follows. Since the ZrO_2 nanotubes are filled with CaP nucleation sites after dipping treatment, the HA formed inside of the nanotubes. The structure of the coating then gradually changed from Zr substrate to ZrO_2 nanotubes with HA coatings. The gradual change of the structure resulted in a high bonding strength. It has been reported that, after the glass-ceramic A-W with CaP layer was implanted as a rabbit tibia for one month and a tensile stress was applied on the bone, the fracture occurred within the bone but not at the bone-implant surface [20]. This demonstrated that even the glass-ceramic A-W with CaP layer was strongly bonded after implantation. The present work showed that HA coating formed on ZrO_2 nanotubes had even higher bonding strength, and suggests that ZrO_2 having HA coating can bond very tightly to living bone.

5.5 Conclusions

A series of ZrO_2 nanotubular arrays formed by anodization in fluoride containing electrolyte, having diameters ranging from 35 nm to 80 nm and wall thickness from 1.79 μm to 3.80 μm was prepared using anodization of Zr at different voltages between 20 V and 50 V for 20 min. The as-formed ZrO_2 nanotubular arrays were found to be suitable for a dipping treatment leading to surface deposit of calcium phosphate crystallites. CaP crystallites were deposited uniformly on and inside the ZrO_2 nanotubular arrays. The pretreatment highly enhanced the capability of HA coating formation on ZrO_2 nanotubular arrays in SBF cultures, while in absence of the dipping treatment almost no HA formed. Several μm thick HA formed within 8 days immersion in SBF. Using the pretreatment, HA coating grew more quickly on unannealed arrays than on annealed tubular arrays.

XRD, XPS and FTIR analyses showed that the composition of deposited HA was close to physiological samples in ratio of Ca to P and incorporation of Mg, Na, and formation of carbonate functional groups within the crystalline structure. The tensile bonding strength of the HA coating on Zr with ZrO_2 nanotubular arrays after 8 days immersion in SBF is 21.2 ± 1.6 MPa, which fulfills the requirement according to the ISO standard.

The combination of anodization to form ZrO_2 nanotubular arrays and the dipping method for Zr implant materials is a highly promising method to

accelerate HA formation on as-formed ZrO_2 nanotubular arrays when immersed in SBF. Therefore the combined treatment provides an efficient way to enhance the rate of HA formation on Zr biomaterials. The results are consistent with an evaporation based mechanism and formation of CaP nucleation sites attached to the ZrO_2 nanotubular arrays.

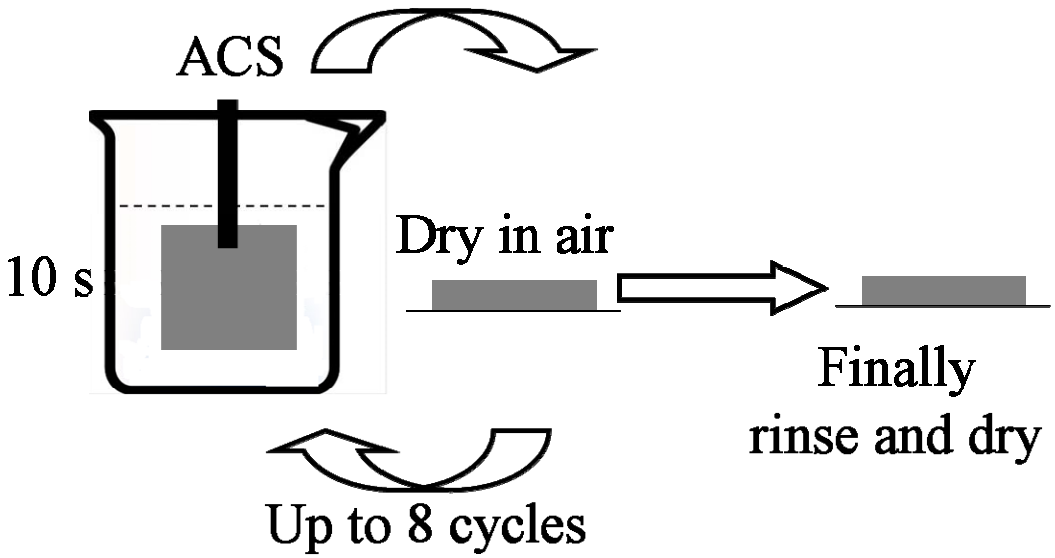

Figure 5-1 Schematic outline of the dipping treatment leading to deposition of CaP on ZrO_2 nanotubular arrays.

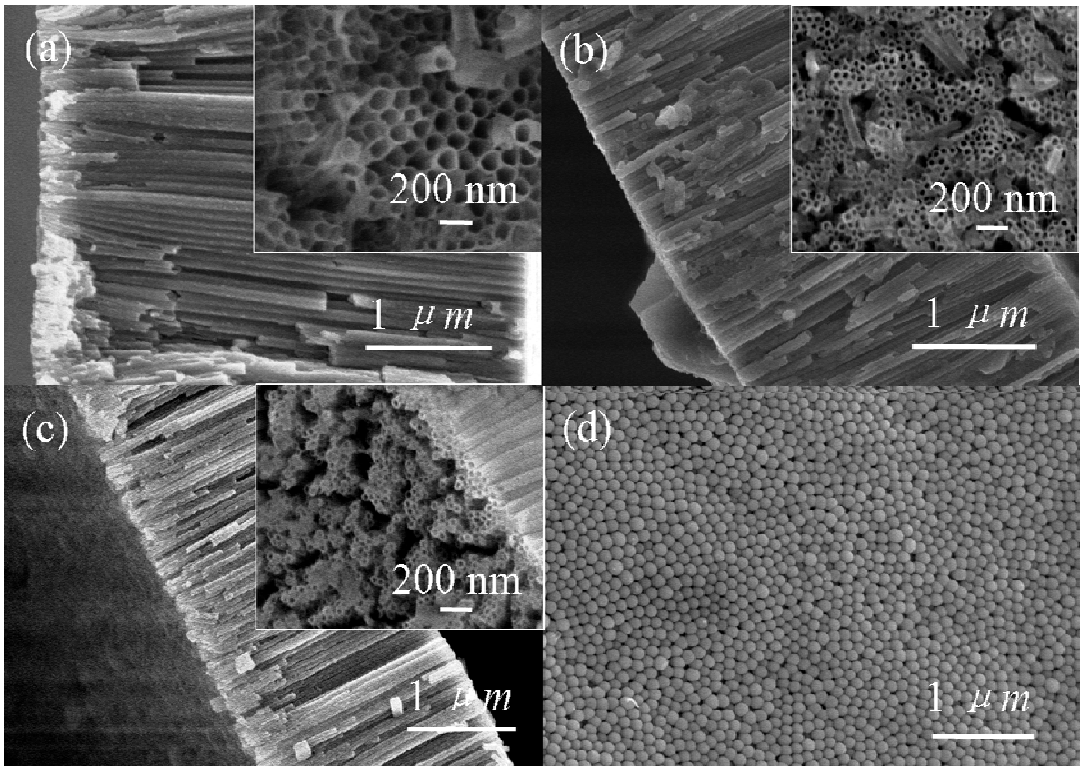

Figure 5-2 SEM images of surface morphology of anodic ZrO_2 nanotube structures; anodized for 20 min at: (a) 50 V; (b) 32 V; (c) 20 V; and (d) a bottom view of the sample for (a).

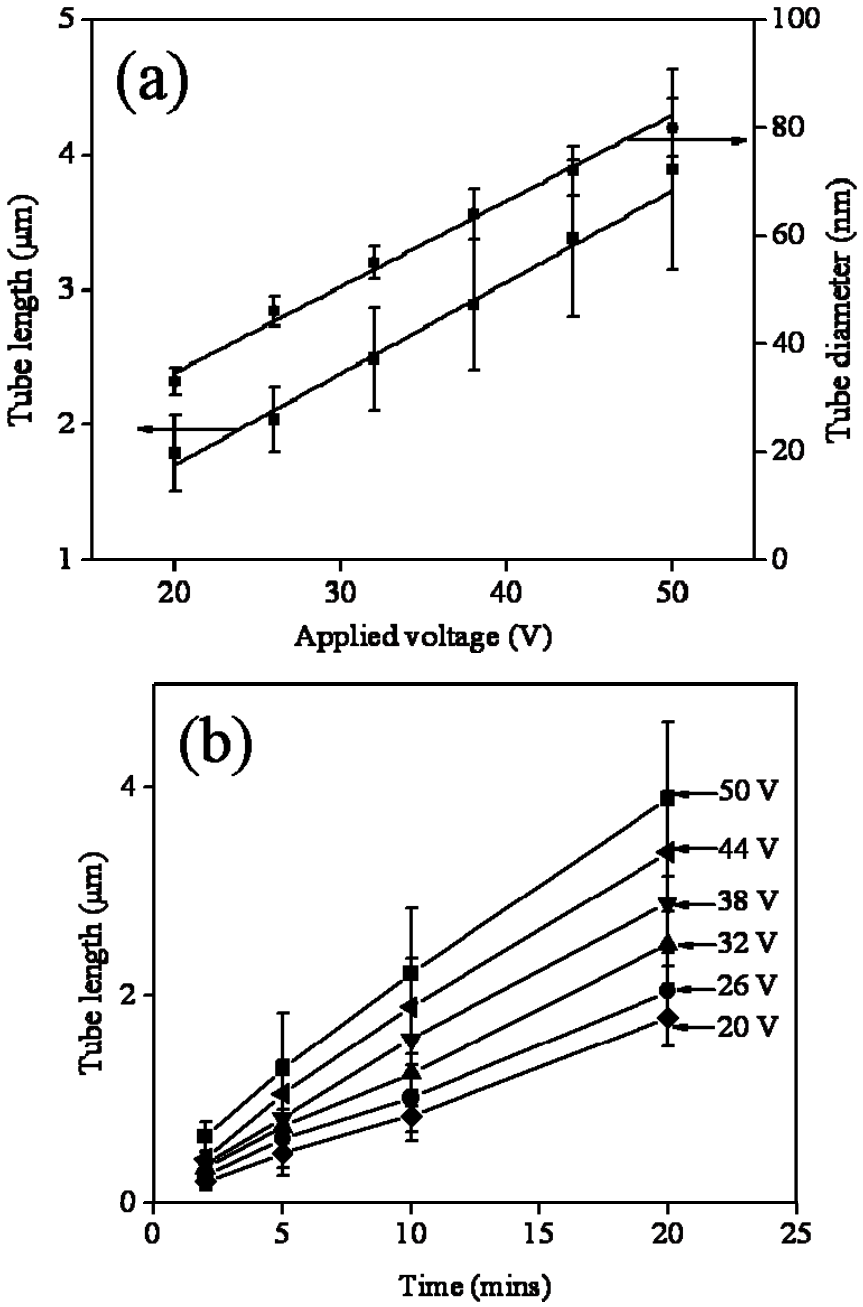

Figure 5-3 (a) Relationship between nanotube diameter, length, and applied voltage for 20 min anodization, and (b) kinetic curves of ZrO_2 nanotubular arrays anodized at different applied voltages for 20 min.

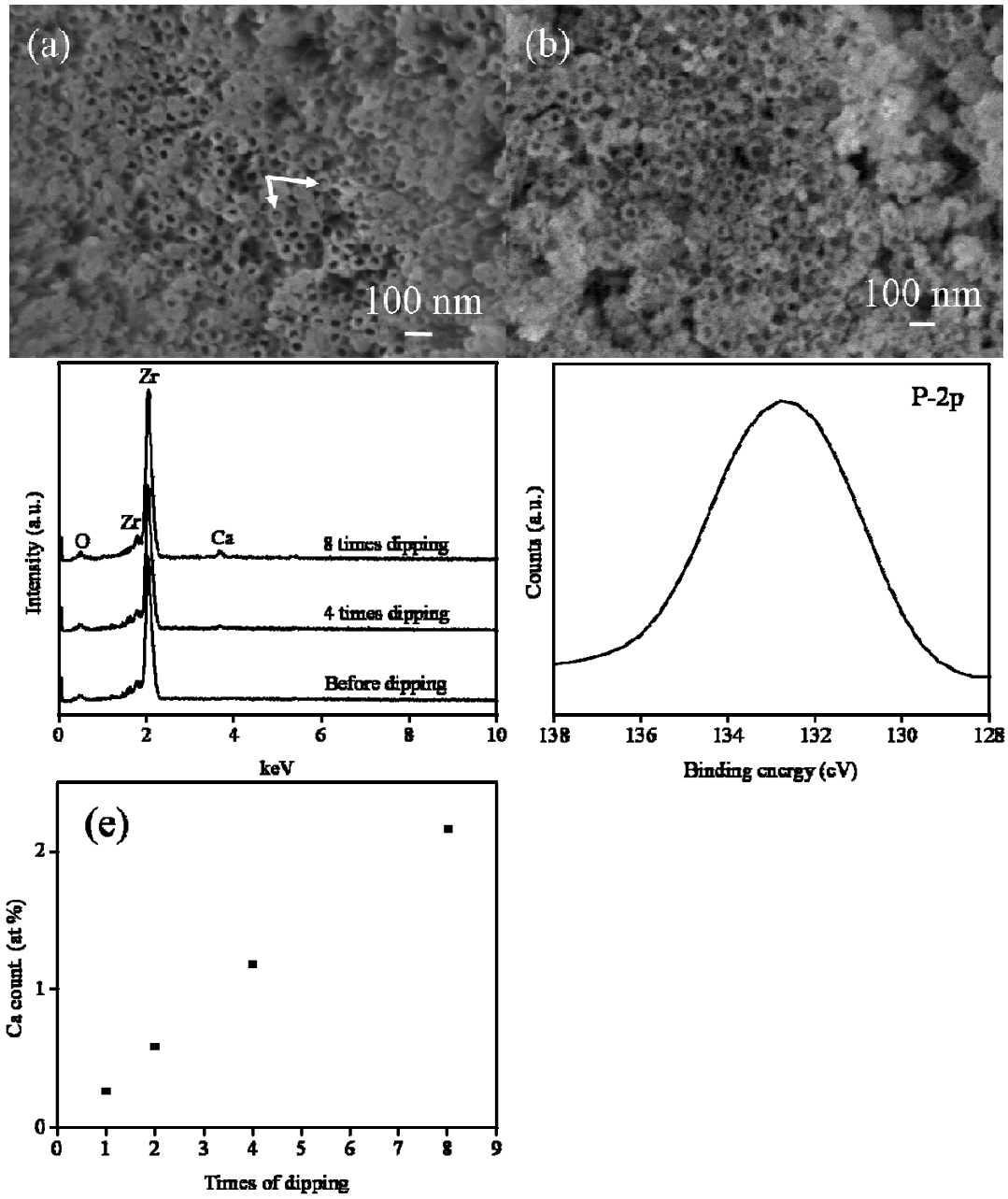

Figure 5-4 SEM image of surface morphology of ZrO_2 nanotubes anodized at 50 V for 20 min: after dipping (a) 4 times and (b) 8 times; (c) EDX spectra of the surface composition after different dipping treatments; (d) XPS spectrum of P-2p peak; (e) the amount of Ca deposited on the tubes as a function of cycles of dipping treatment.

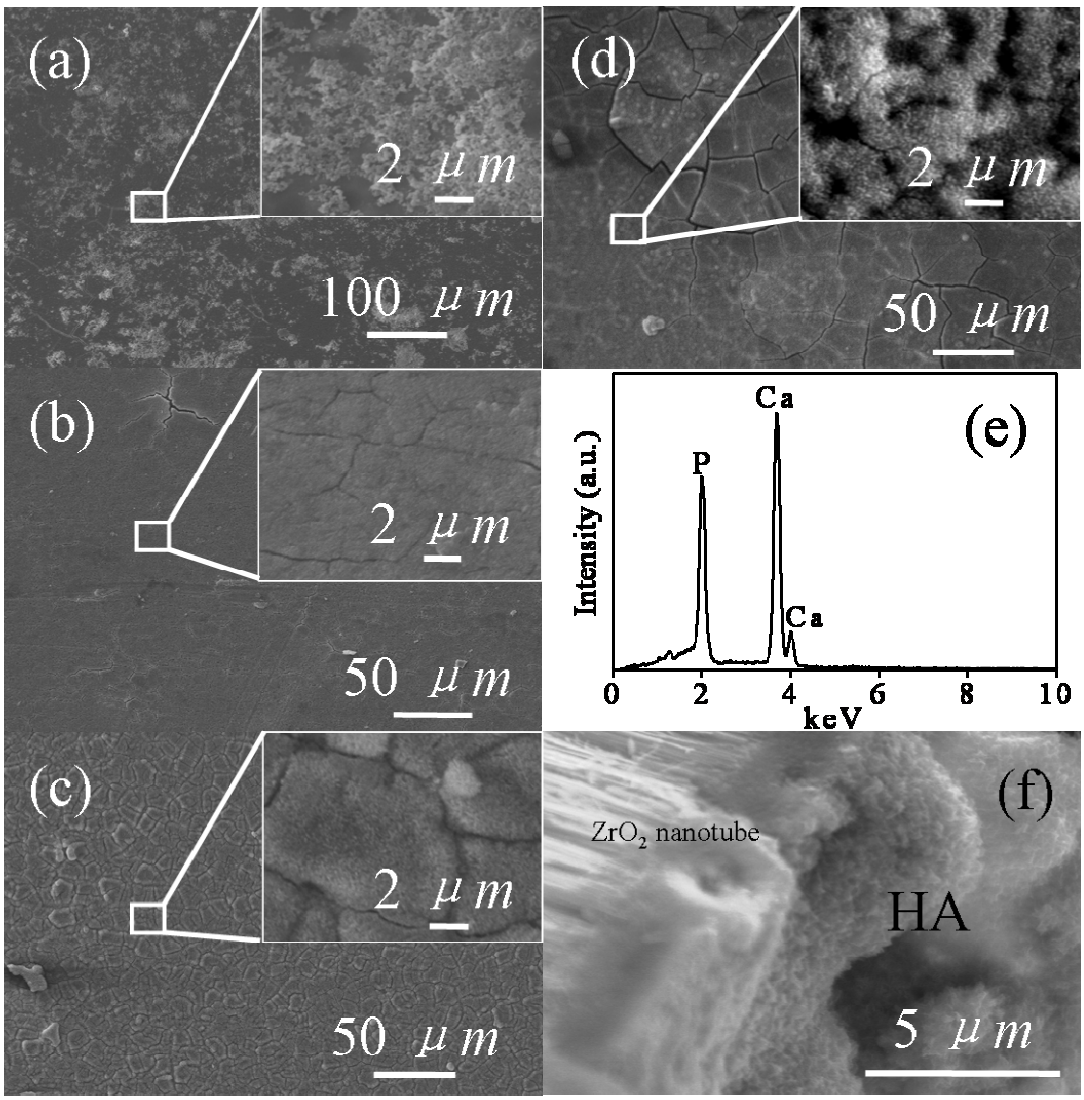

Figure 5-5 SEM images of the dipping-treated ZrO_2 nanotubular arrays immersion in SBF for different periods: (a) 1 day; (b) 2 days; (c) 4 days; and (d) 8 days; (e) EDX spectrum of the sample for (d); (f) SEM cross section view of the HA coating formed after 8 days of immersion in SBF.

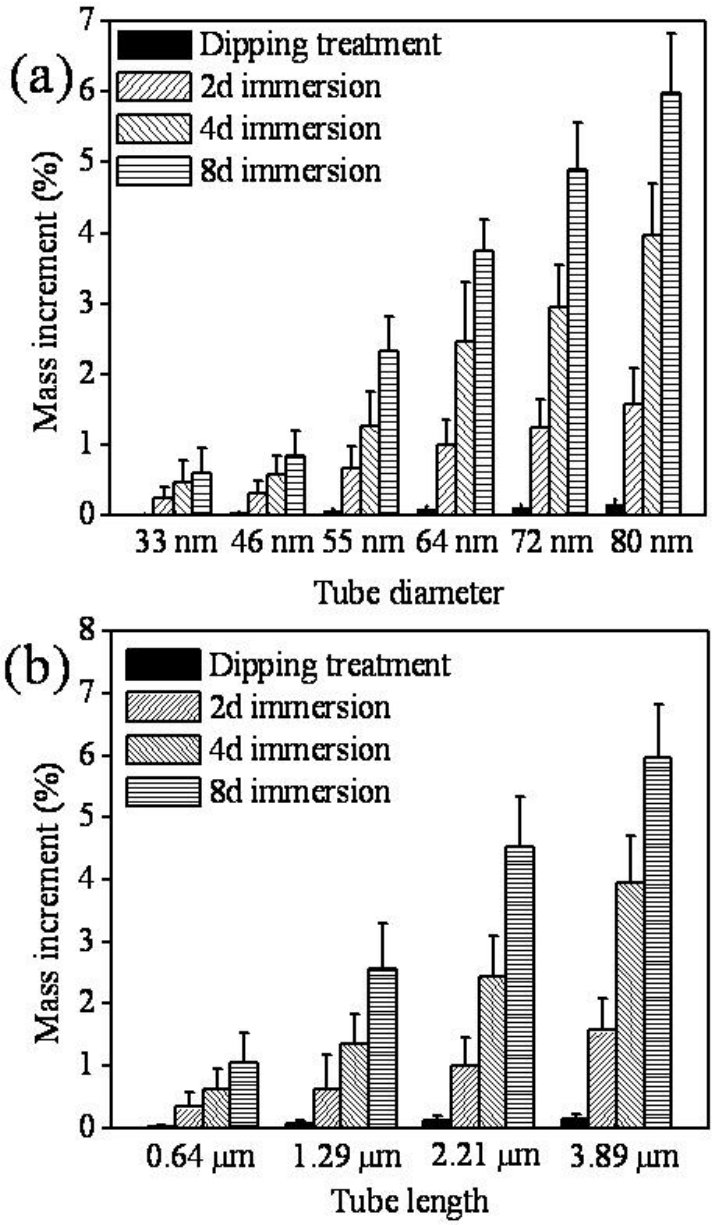

Figure 5-6 Effect of geometrical factors on the deposited HA coating formation: (a) mass increment of the samples as a function of tubular inner diameter after dipping treatment and soaking for up to 8 days, and (b) mass increment of the samples as a function of tubular length after dipping treatment and soaking for up to 8 days.

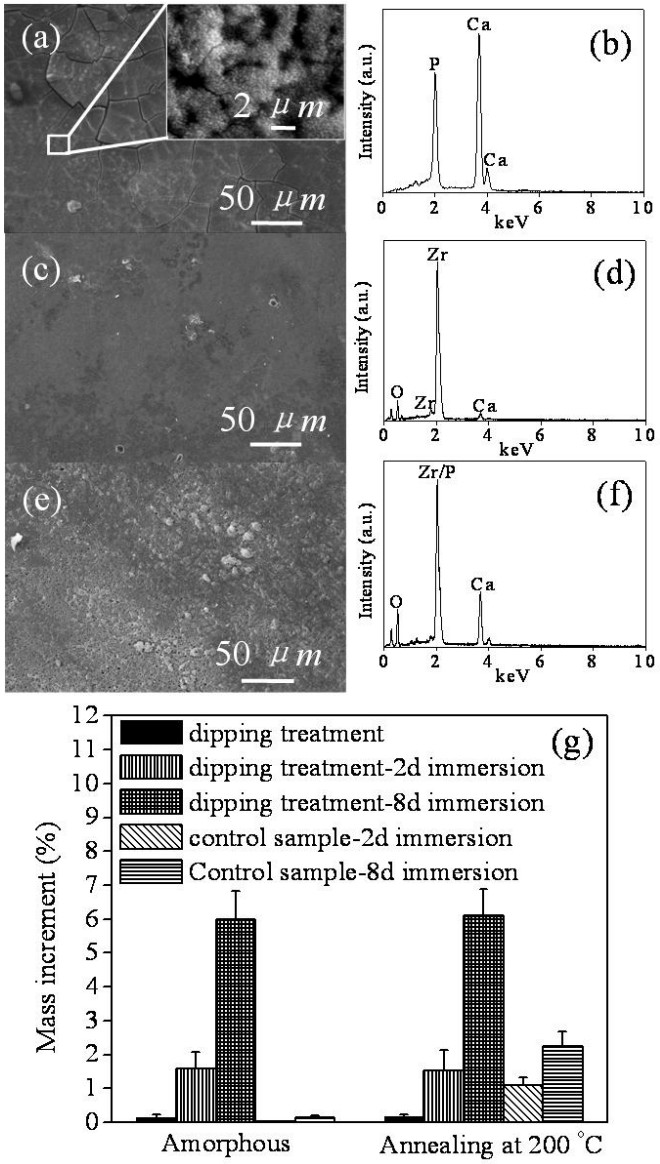

Figure 5-7 SEM top views of nanotubular arrays with: (a) dipping treatment; (c) no dipping treatment; (e) annealed at 200 ^{o}C after SBF soaking for 8 days; and the corresponding EDX spectra (b), (d) and (e); (g) mass increments of the unannealed and annealed samples after dipping treatment and after SBF soaking for 2 and 8 days each, without and with the dipping treatment.

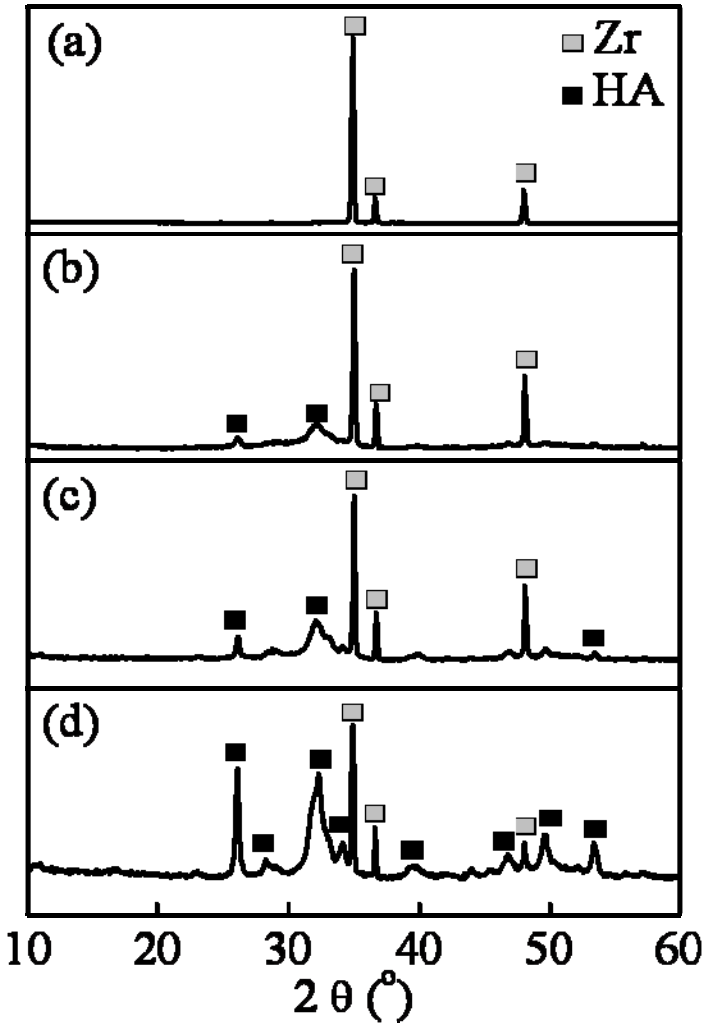

Figure 5-8 XRD patterns of the ZrO_2 nanotubular arrays: (a) before treatment; and after immersion in SBF for: (b) 2 days; (c) 4 days; and (d) 8 days.

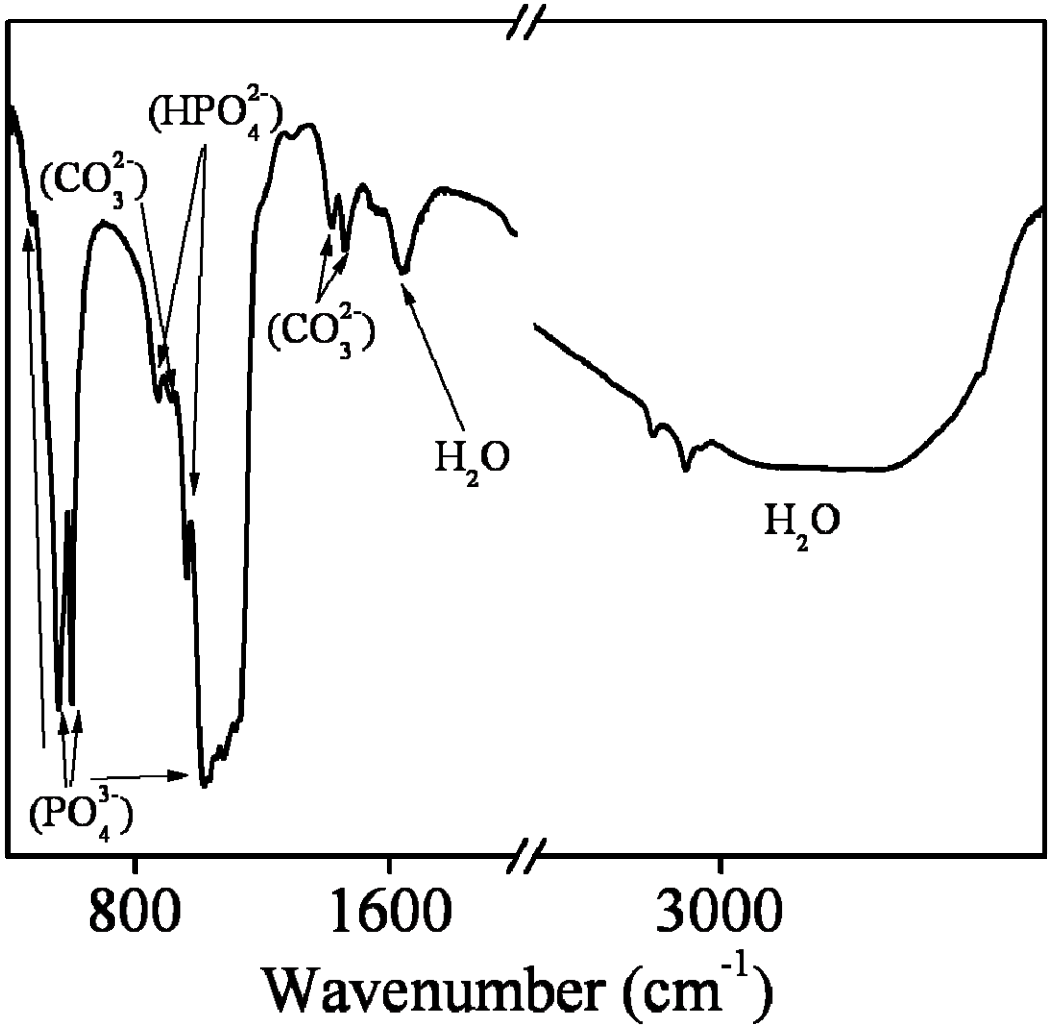

Figure 5-19 FT-IR spectra of the HA coating on ZrO_2 nanotubular arrays with dipping treatment after 8 days of immersion in SBF.

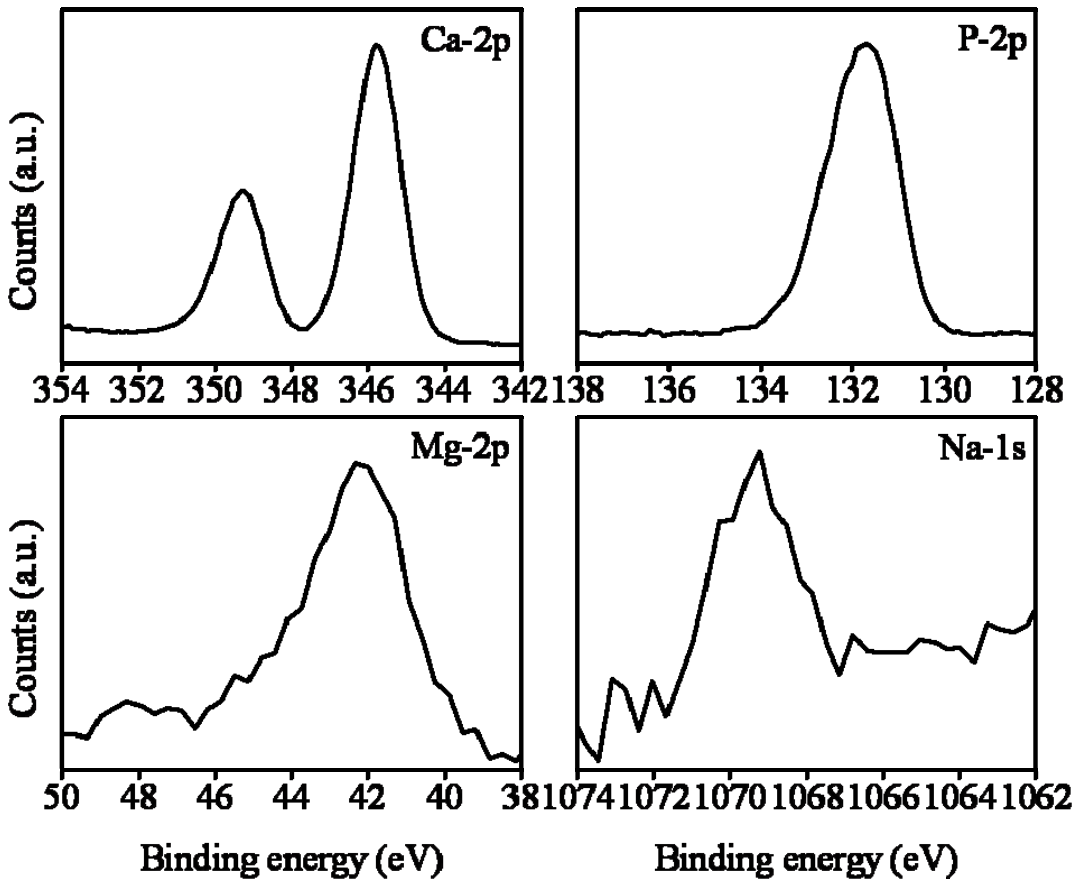

Figure 5-10 XPS spectra showing peaks for Ca-2p, P-2p, Mg-2p, and Na-1s for the HA coating grown in SBF for 8 days.

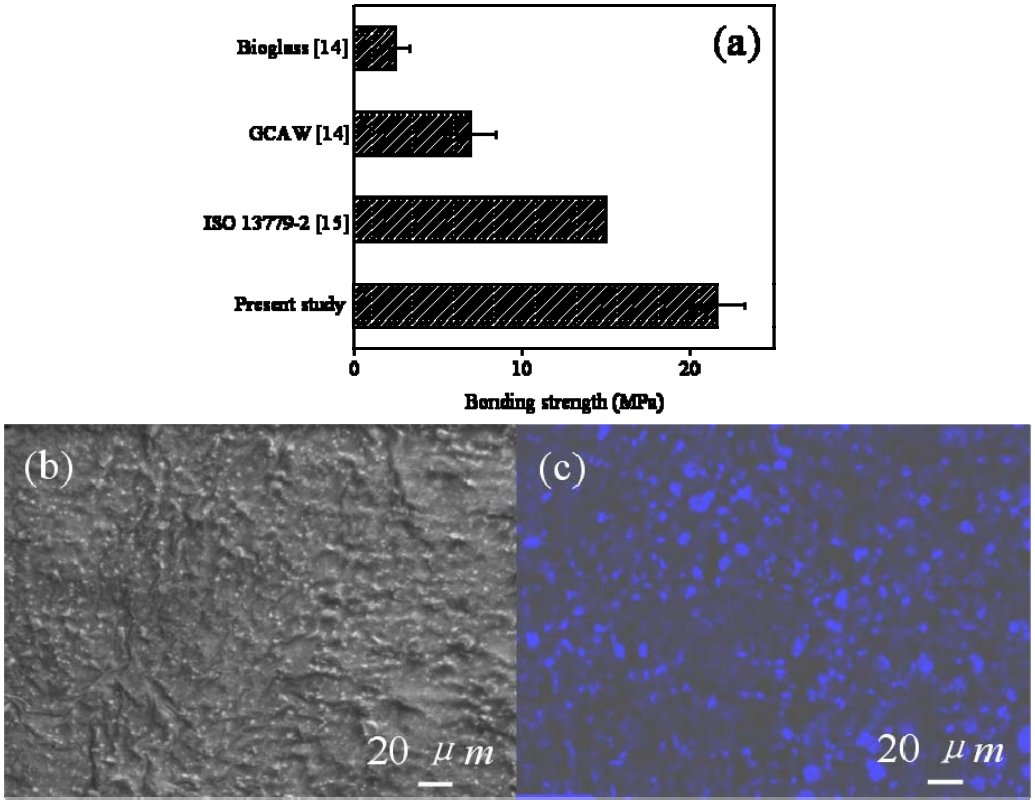

Figure 5-11 (a) SEM image of the fracture surface of the substrate, and (b) EDX mapping of Ca; (c) SEM image of the fracture surface part of a steel bar, and (d) EDX mapping of Ca.

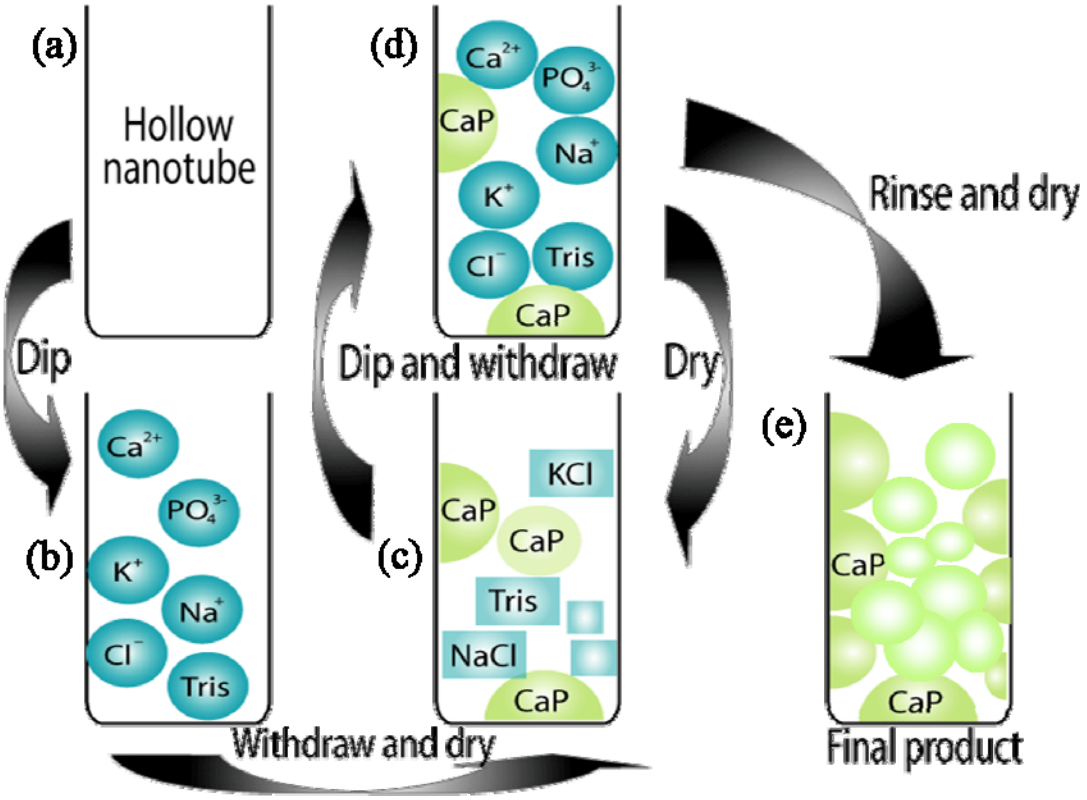

Figure 5-12 Proposed mechanism for the dipping treatment of ZrO_2 nanotubular arrays: (a) the Zr substrate with the ZrO_2 nanotubes dip and withdraw in ACS; (b) a wetting film filling in the nanotubes structure; (c) the film drying and forming CaP crystallites, and other crystalline chemicals, such as NaCl, KCl, and tris; CaP adheres to the nanotubes; (d) during the repeated dip-and-withdraw procedures, more and more CaP forms and adheres to the nanotubes; (e) the formation of CaP crystallites covers nanotubes after rinsing and drying (adapted from [5, 16]).

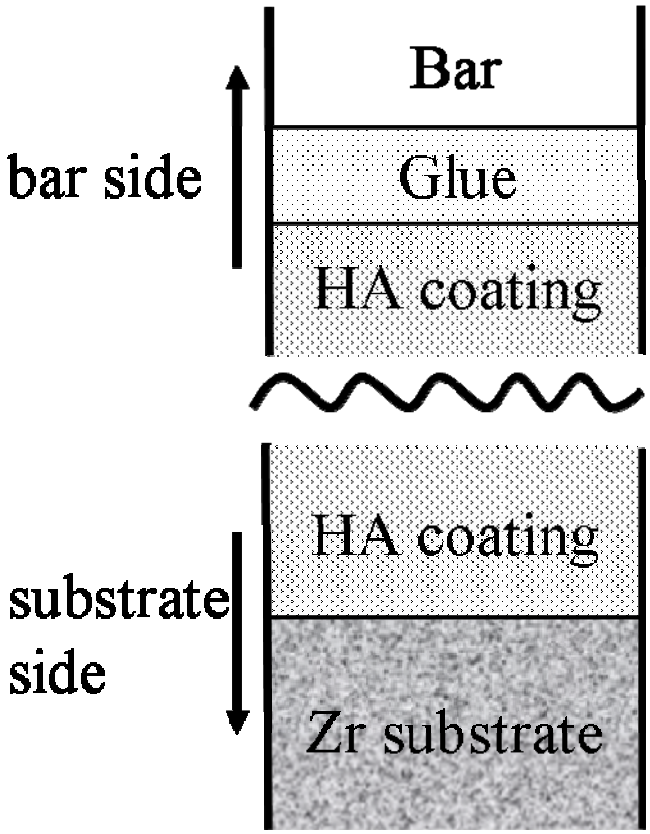

Figure 5-13 Schematic representation of the fracture mode of HA coating on ZrO_2 nanotubular arrays.

References

[1] H. B. Wen, Q. Liu, J. R. de Wijn, K. de Groot, F. Z. Cui, Preparation of bioactive microporous titanium surface by a new two-step chemical treatment, J. Mater. Mater. Med. 9 (1998) 121-128.

[2] T. Kokubo, H. Takadama, How useful is SBF in predicting in vivo bone bioactivity? Biomaterials 27 (2006) 2907-2915.

[3] L. Müller, F. A. Müller, Preparation of SBF with different HCO_3^- content and its influence on the composition of biomimetic apatite on anodic TiO_2 nanotubes. Acta Biomater. 2 (2005) 181-189.

[4] L. Guo, J. Zhao, X. Wang, X. Xu, H. Liu, Y. Li, Structure and bioactivity of zirconia nanotube arrays fabricated by anodization, Int. J. Appl. Ceram. Technol. 6 (2009) 636–641.

[5] L. N. Wang, J. L. Luo, Formation of hydroxyapatite coating on anodic titanium dioxide nanotubes via an efficient dipping treatment, Metal. Mater. Trans. A. DOI: 10.1007/s11661-010-0484-z.

[6] W. J. Lee, W. H. Smyrl, Zirconium oxide nanotubes synthesized via direct electrochemical anodization, Electrochem. Solid-State Lett. 8 (2005) B7-B9.

[7] J. Zhao, R. Xu, X. Wang, Y. Li, In situ synthesis of zirconia nanotube crystallines by direct anodization, Corr. Sci. 50 (2008) 1593-1597.

[8] L. Guo L, Zhao J, Wang X, Xu R, Li Y. Synthesis and growth mechanism of

zirconia nanotubes by anodization in electrolyte containing Cl^-. J Solid State Electrochem. 13 (2009) 1321-1326.

[9] G. K. Mor, O. K. Varghese, M. Paulose, N. Mukherjee, C. A. Grimes, Fabrication of tapered, conical-shaped titania nanotubes, J. Mater. Res. 18 (2003) 2588-2593.

[10] J. M. Macak, H. Tsuchiya, L. Taveira, S. Aldabergerova, P. Schmuki, Smooth anodic TiO_2 nanotubes, Angew. Chem. Int. Ed. 44 (2005) 7463-7465.

[11] R. Beranek, H. Hildebrand, P. Schmuki, Self-organized porous titanium oxide prepared in H_2SO_4/HF electrolytes, Electrochem. Solid State Lett. 6 (2003) B12-B14.

[12] R. Horváthová, L. Müller, A. Helebrant, P. Greil, F. A. Müller, *In vitro* transformation of OCP into carbonated HA under physiological conditions, Mater. Sci. Eng. C. 28 (2008) 1414-1419.

[13] C. Rey, C. Combes, C. Drouet, H. Sfihi, A. Barroug, Physico-chemical properties of nanocrystalline apatites: Implications for biominerals and biomaterials, Mater. Sci. Eng. C. 27 (2007) 198-205.

[14] H. M. Kim, F. Miyaji, T. Kokubo, T. Nakamura, Bonding Strength of Bonelike Apatite Layer to Ti Metal Substrate, J. Biomed. Mater. Res. B. Appl. Biomater. 38 (1997) 121–127.

[15] ISO Implants for surgery-hydroxyapatite-part 2: coatings of hydroxyapatite. ISO 13779-2 2008.

[16] K. Duan, A. Tang, R. Wang, A new evaporation-based method for the preparation of biomimetic calcium phosphate coatings on metals, Mater. Sci. Eng. C 29 (2009) 1334-1337.

[17] E. Landi, G. Celotti, G. Loggroscino, A. Tampieri, Carbonated hydroxyapatite as bone substitute, J. Euro. Ceram. Soc. 23 (2003) 2931-2937.

[18] I. R. Gibson, W. Bonfiel, Novel synthesis and characterization of an AB-type carbonate-substituted hydroxyapatite, J. Biomed. Mater. Res. 59 (2002) 697-708.

[19] S. M. Barinov, J. V. Rau, S. Nunziante Cesaro, J. Ďurišin, I. V. Fadeeva, D. Ferro, L. Medvecky, G. Trionfetti, Carbonate release from carbonated hydroxyapatite in the wide temperature rage, J. Mater. Sci. Mater. Med. 17 (2006) 597-604.

[20] T. Nakamura, T. Yamamuro, S. Higashi, T. Kokubo, S. Itoo, A new glass-ceramic for bone replacement: evaluation of its bonding to bone tissue, J. Biomed. Mater. Res. 19 (1985) 685-698.

Chapter 6 Fabrication and formation of bioactive anodic zirconium oxide nanotubes containing presynthesized hydroxyapatite via alternative immersion method*

6.1 Introduction

In this chapter, we explore the feasibility of the formation of ZrO_2 nanotubes with presynthesized HA via the AIM treatment and study whether the method promises an accelerated HA formation in a simulated biological environment on the AIM-treated ZrO_2 nanotubular arrays. The amount of the synthetic HA formed via AIM and HA formed during the immersion in SBF was quantified based on geometrical factors such as the diameter of the tube and the thickness of the layer. In order to prove the advantage of the present study, we also make a comparison with the existing method, i.e. HA formation on the annealed ZrO_2 nanotubes in simulated biological environment [1].

6.2 The AIM treatment process

The presynthesizing HA on ZrO_2 nanotubes was carried out by applying the AIM treatment. The specimens were vertically exposed into the following order:

* Material in this chapter has been published in:
L. N. Wang and J. L. Luo, Mater. Sci. Eng. C. 31 (2011) 740-747.

saturated $Ca(OH)_2$, DI water, 0.02 M $(NH_4)_2HPO_4$, and DI water respectively. The immersion in each solution lasted 1 min at room temperature and one cycle of immersion was defined as exposure in 3 solutions consequently. The specimens were immersed up to 20 cycles and then rinsed by DI water and dried in front of compressed air [1].

6.3 Results and discussions

6.3.1 The formation and structure of ZrO_2 nanotubes

The ZrO_2 nanotubes were synthesized with various applied voltages in different periods. Figure 6-1 shows an example of the nanotubes formed at 30 V for 1 h. The top view is portraited in Figure 6-1a with the higher magnification in Figure 6-1b. Figures 6-1c and 6-1d show the side view of the tubular layer and its higher magnification image. Figure 6-1 clearly shows an ordered nanotubular arrays with an average individual tube diameter of about 50 nm and layer thickness of about 5 μm. The layer thickness and the opening of tubes can be easily adjusted by changing the applied voltage and duration. Results obtained from SEM investigation on the ZrO_2 nanotubular layers in this work are compiled in Figure 6-2 for the tube openings and layers formed at voltages ranging from 15 to 30 V. Figure 6-2a shows the effect of applied voltage on the nanotubular thickness and inner diameter of tubes. It is apparent that the layer thickness and opening of the tubes linearly depend on the applied voltage. Figure 6-2b shows the relationship between tubular

layer thickness and the anodization time under constant applied voltage, 30 V for 1 h anodization. It is clearly seen that the layer thickness linearly increases with respect to the anodization time. The tendency is inline with the previous report of the growth of ZrO_2 in HF containing electrolyte [16]. Although the growth rate may not be the same, it can be attributed to the different electrolyte composition since the ZrO_2 in aqueous HF has higher oxidation rate than that in the electrolyte applied in this work.

The exact mechanism of the ZrO_2 nanotubes formation is still the subject of some debate. However, it has been well-established that the ZrO_2 nanotube formation in fluoride containing solution is a result of three simultaneous processes: (1) electric field-assisted oxidation of zirconium to form zirconium dioxide, (2) electric field-assisted dissolution of zirconium ions in electrolyte and (3) chemical dissolution of Zr and ZrO_2 by etching fluoride ions [2]. The formation of the tubes is most likely enhanced by the applied electric field for anodization, as observed in aluminum oxide [3]. Inside the tubes there are two interfaces: oxide/metal and oxide/anodizing solution. Applied electric field-enhanced oxidation occurs at the oxide/metal interface near the tube bottom when the oxygen-containing anions such as O^{2-} and OH^- transport from the solution to the oxide layer, along the direction of the tube growth. At the same time, metal ions migrate from the metal to the solution/oxide interface and dissolve into the solution. The electric field and concentration field can enhance the migration and diffusion of the metal ions. The

metal dissolution rate at the bottom is far greater than that at the wall, resulting in perpendicular growth of the channel with high aspect ratio. It is anticipated that some similar processes are operative in the ZrO_2 nanotube arrays found in present study.

6.3.2 The AIM treatment on ZrO_2 nanotubes

Figure 6-3 shows the top view of the samples after AIM treatment for 20 cycles. The treatment clearly leads to the formation of particles fully covering the surfaces. The higher magnification image (Figure 6-3b) shows the spherical particles. From the top views, it can be observed the homogenous distribution of deposits on the entire sample surfaces. To identify the surface chemicals and compositions, XPS and XRD were performed on the samples after AIM treatment. The XPS results revealed the existence of Ca and P species and showed the Ca and P peaks in Figure 6-3c. The phosphorous peak of the deposit is centered at 133 eV, which is in line with the observation for Ca species bound to phosphorous in the form of phosphates [4]. The semiquantitative analysis yields that the ratio of Ca to P is about 1.6, which is closed to that of the hydroxyapatite [4]. Figure 6-3d illustrates the XRD spectra of the samples before and after AIM treatment. The XRD spectrum of the controlled specimen shows only sharp and high peaks of Zr but no obvious peak of ZrO_2, which indicates that the as-formed ZrO_2 nanotubular is amorphous phase. After AIM treatment, peaks appear within 26-32^o, which is shown in the inserted figure. By comparison with the standard data (JCPDS 09-0432), it clearly shows

that after AIM treatment, the deposit layer is indeed the crystalline HA. Additionally, there are peaks indicating the existence of $Ca_2P_2O_7 \cdot 2H_2O$. The existence of $Ca_2P_2O_7 \cdot 2H_2O$ after AIM treatment is possible due to the dehydration of $CaHPO_4$ formed by Ca^{2+} and HPO_4^{2-} during the AIM treatment. Meanwhile, the $Ca_2P_2O_7 \cdot 2H_2O$ is considered as one of the intermediate products of bone mineralization [5]. We also address the effect of the cycles of AIM on the ZrO_2 nanotubular arrays. In various studies up to 20 cycles of AIM were carried out on the nanotubes obtained by 30 V for 1 h. An increase of Ca content during the HA presynthesizing is observed by XPS and shown in Figure 6-3e. It shows the 20 cycles of AIM on ZrO_2 nanotubes induced about 8 at% of Ca. Therefore, the 20 cycle immersion sequence is applied for the consequence studies.

6.3.3 The HA formations on AIM treated ZrO_2 nanotubes

Figure 6-4a shows the weight gain on ZrO_2 nanotubes with different tube diameters after AIM-treatment, soaking in SBF for 2 days and 5 days. It clearly shows that the measurement shows increase on all the tube diameters mentioned in Figure 6-2a. The deposition amount almost linearly increases as the tube diameter enhances. Moreover, the largest diameter with 55 nm has almost 3 times weight gains than that on the 25 nm diameter. Figure 6-4b shows the deposition amount on the ZrO_2 nanotubes with different tube length mentioned in Figure 6-2b. The measurement clearly demonstrates the effect of tube length on the AIM treatment and the subsequent HA formation in SBF. Hence both the tube diameter and length

play roles during the treatment. Thus it is possible to conclude that the AIM treatment and HA formation is highly affected by the tube geometrical factors.

Figure 6-5 shows the deposited HA on the AIM-treated ZrO_2 nanotubular arrays after immersion in SBF for 2 days (Figure 6-5a) and 5 days (Figure 6-5c). Figures 6-5b and 6-5d portrait the EDX spectra corresponding to Figures 6-5a and 6-5c, respectively. A weak Zr peak is shown in Figure 6-5b but not in Figure 6-5d, which indicates that not only a HA coating fully covers the substrate but also the coating becomes thicker and denser after the 5 days of soaking in SBF. Since it has been reported that HA formed on as-formed anodic ZrO_2 nanotubes during 30 days immersion in SBF, thus, present study shows that the AIM treatment shows a strong enhancement on the HA formation on as-formed ZrO_2 nanotubular arrays. On the other hand, previous work indicated that the annealed ZrO_2 nanotubular arrays at 200 ^{o}C for 3 hrs induced significant HA formation. Therefore, some ZrO_2 nanotubes were annealed based on previous study to investigate the effect of the AIM treatment. The annealed ZrO_2 nanotubes with and without AIM treatment were immersed in SBF for 2 days and 5 days. Figures 6-5e and 6-5f show the morphology and EDX spectrum of the annealed ZrO_2 nanotubular arrays without AIM treatment after soaking in SBF for 5 days. The image in Figure 6-5e shows that the surface is covered by a thin layer of spherical particles. By analyzing the EDX spectrum in a logarithm scale, it shows a weak peak of Ca but the P peak is not easily detected, which demonstrates poor HA formation capability on annealed

ZrO_2 nanotubular arrays within 5 days. However, the AIM treatment leads to a dramatic enhancement of the HA deposition on the annealed sample as shown in Figure 6-5g, which portraits a coating with large amount of agglomerated particles, similar as shown in Figure 6-5a. Figure 6-5h shows the comparison of the increment of weight measurements for the AIM-treated and non-AIM treated samples after immersion in SBF for 2 days and 5 days. It is obvious that in each case of non-annealed and annealed ZrO_2 nanotubes, the AIM treatment provides improvement of an accelerated HA formation in SBF. It also shows that the annealed and non-annealed cases show similar amount increment after AIM treatment. In fact, it indicates that by applying the AIM treatment, the capability of HA formation is dramatically enhanced compared to that on the annealed treatment.

The XRD spectrum of the coating formed after 5 days immersion in SBF was obtained by analyzing the powder scratched from the specimen surface. Figure 6-6 portraits the XRD spectrum of the HA powder and the black bar shows the standard pattern of the HA. It clearly shows the reflected peaks are in good agreement with the standard profile of HA [6] and the main peaks are cited in the figure. Figure 6-7 illustrates the FTIR spectrum of the HA coating and the summarized functional groups. Their vibration wavenumbers are listed in Table 6-2. A broad absorption band from 2500-3600 cm^{-1} and the bending mode at 1645 cm^{-1} of intercalated H_2O were observed in the spectra of the precipitated coatings. A broad phosphate band derived from the P-O asymmetric stretching mode (υ_3) of the PO_4^{3-} group was

found in the region from 1200 to 960 cm^{-1}, indicating a deviation of the phosphate ions from their ideal tetrahedral structure. The triple (υ_4) and double (υ_2)-degenerated bending modes of phosphates O-P-O bonds were found at 604, 567, and 474 cm^{-1}. The bands detected at 1460, 1420, and 875 cm^{-1} were assigned to the CO_3^{2-} group of B-type carbonated HA where PO_4^{3-} groups are substituted by CO_3^{2-}. However, characteristic peaks at 875 and 958 cm^{-1} indicate clearly the presence of HPO_4^{2-} in the crystal lattice [7, 8]. These results additionally confirm HA formation on nanotube structures after soaking in SBF. Figure 6-8 shows the XPS spectra of the chemical composition of the as-formed HA coating. From the semiquantitative analysis, the ratio of Ca to P is 1.4. High resolution peaks show that the composition of the HA layer grown in SBF is close to the physiological HA, since the physiological HA with the ratio of Ca to P is ranging from 1.35 to 1.46. Meanwhile, the HA layer coating also contain considerable amounts of Mg and Na [9].

6.4 Conclusions

The present work shows that anodic ZrO_2 nanotubes are appropriate for synthesizing presynthesized HA via an alternative immersion method (AIM). The AIM-treated nanotubes significantly enhance the HA formation in SBF culture. The HA formation can be obtained within 2 days immersion in SBF. By comparing with the existing annealed ZrO_2 method, there is little HA formed

under same SBF exposure condition. From XRD, XPS and FTIR investigations of the HA coating grown in SBF, it can be deduced that the chemistry of the deposited HA coating is close to physiological conditions not only concerning the ratio of Ca/P but also the incorporation of minor amounts of elements, Mg, Na and functional groups, such as carbonates into the crystalline structure. These results demonstrate that formation of ZrO_2 nanotubes with presynthesized HA via AIM treatment drastically induced the HA deposition and highly enhances the HA formation rate on zirconium and zirconium-based implant materials.

Table 6.2 The corresponding wavenumber of FTIR spectra.

Groups	Wavenumber of vibration peak (cm^{-1})
Bending mode of PO_4^{3-}	474, 567, and 604
Vibration of HPO_4^{2-}	875 and 958
Bending mode of CO_3^{2-}	875
Stretching mode of PO_4^{3-}	960-1200
Vibration of CO_3^{2-} on PO_4^{3-} lattice site	1420 and 1460
Bending mode of H_2O vibration	1645
Vibration of adsorbed H_2O	2500-3600

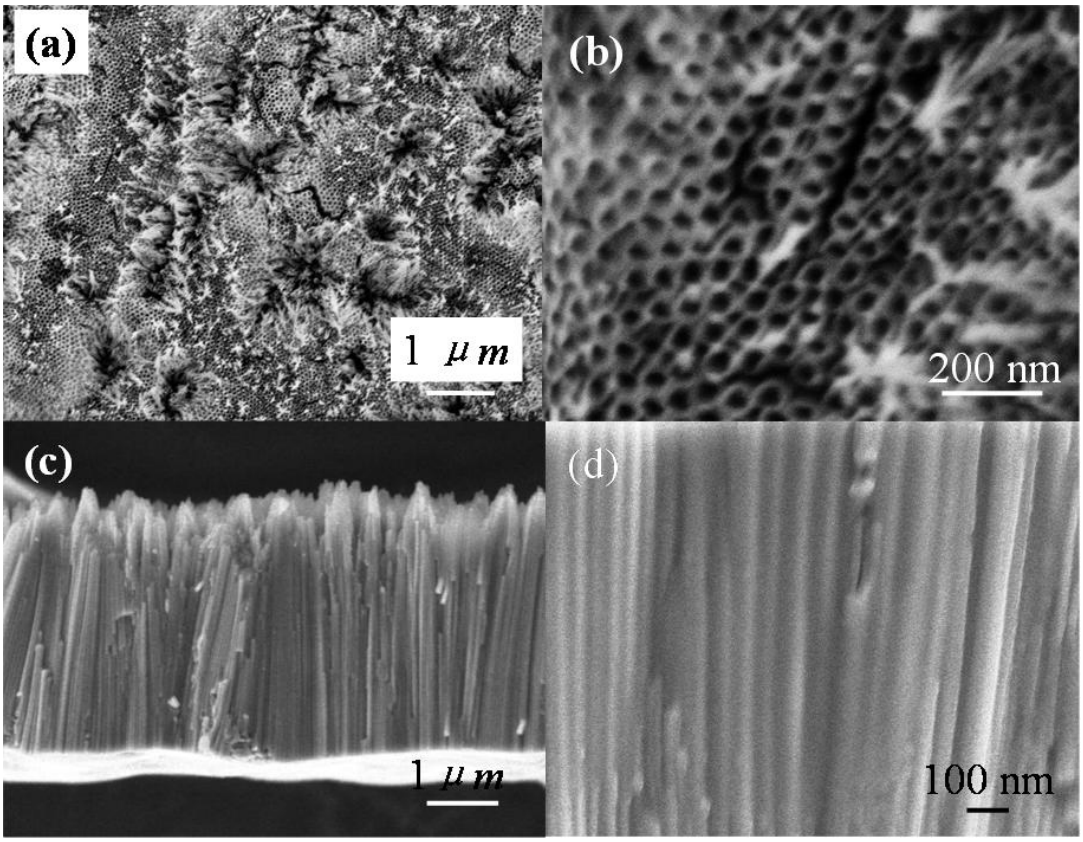

Figure 6-1 An example of SEM image of ZrO_2 nanotubular formed at 30V for 1h: (a) top view; (b) higher magnification of (a); (c) the side view and (d) the higher magnification of (c).

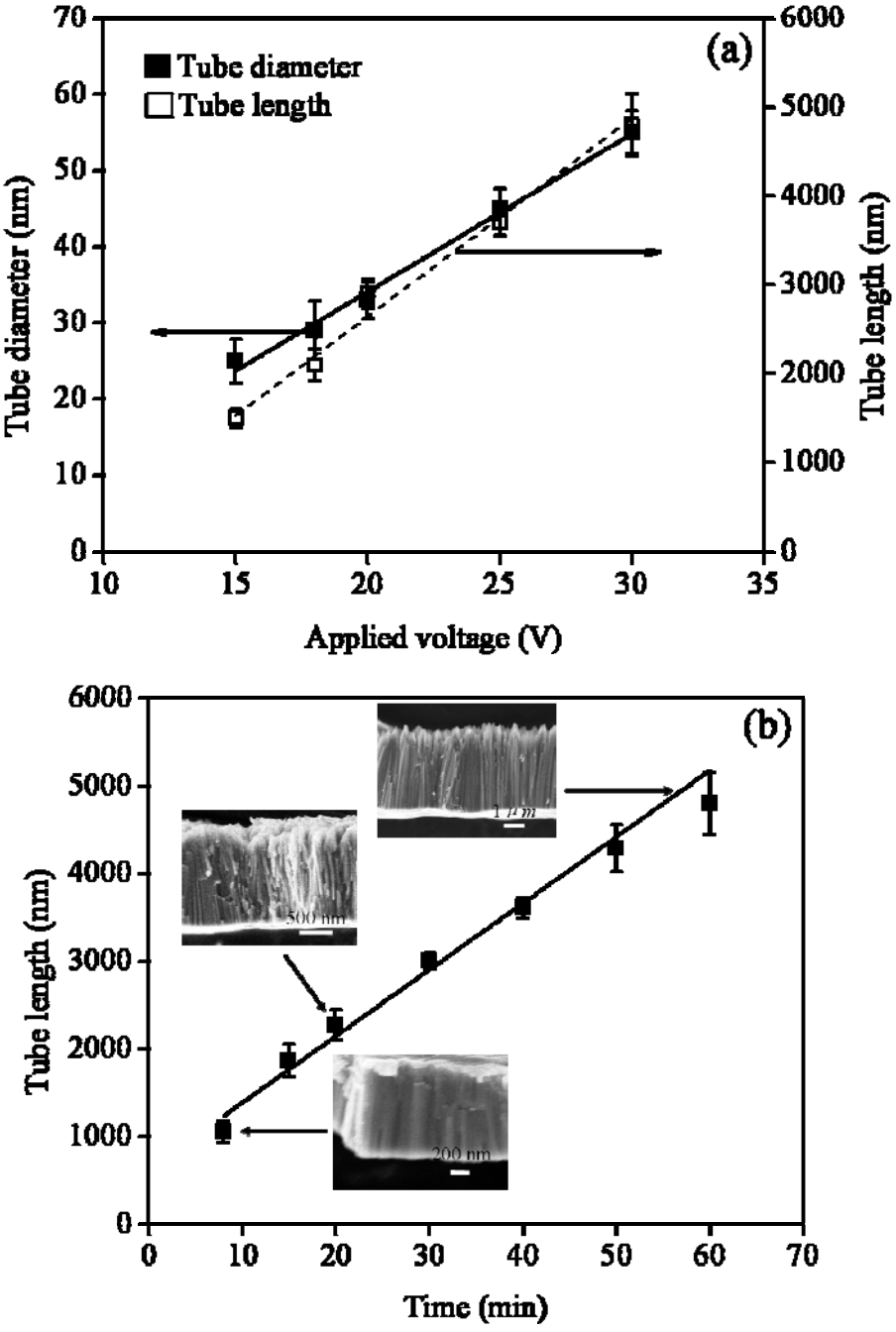

Figure 6-2 The relationship between (a) tube diameter, length and the anodization voltage and (b) anodization time at 30 V and the tube length.

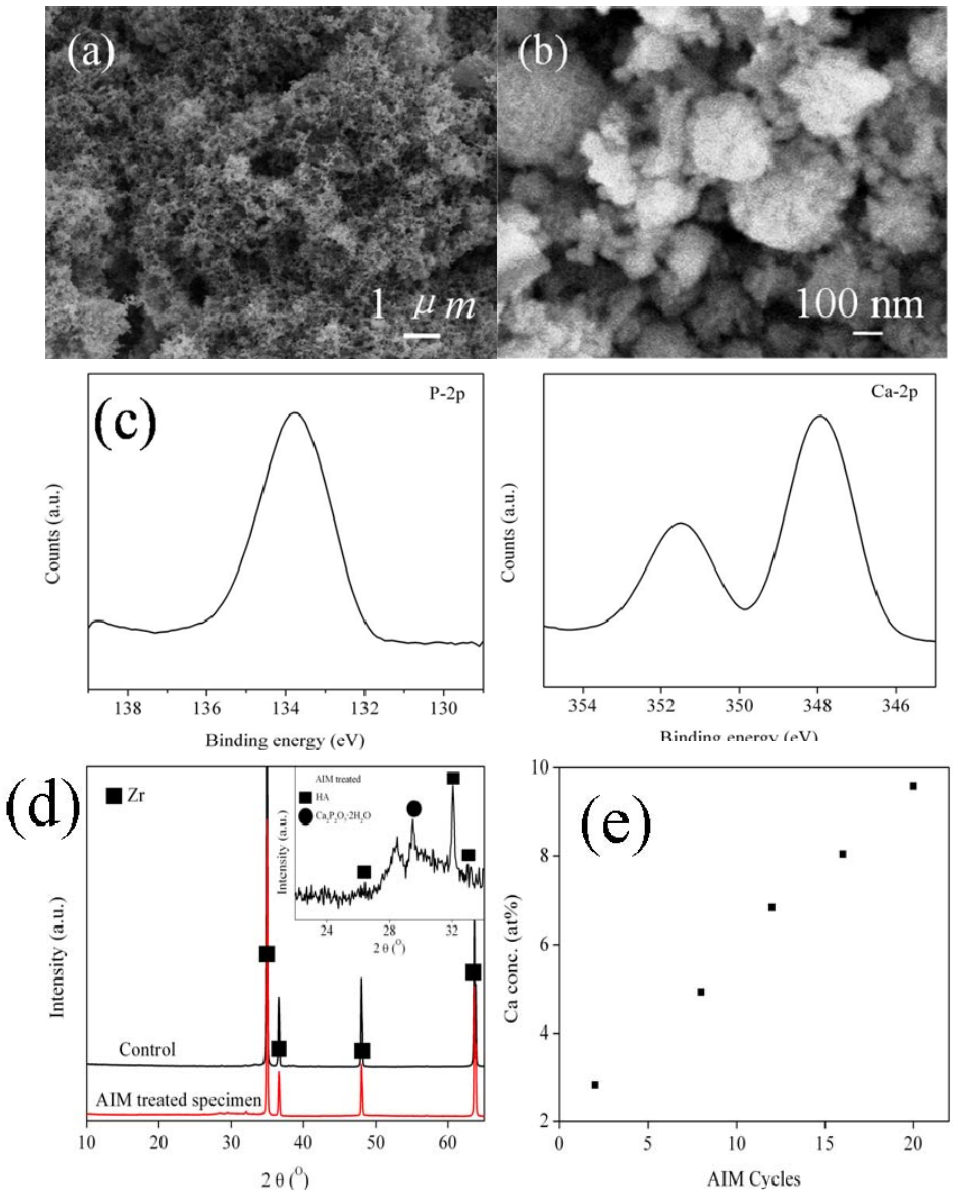

Figure 6-3 The SEM top view of the 20 cycles AIM treated ZrO_2 nanotubular arrays (a) and the higher magnification (b); XPS spectra of the Ca-2p and P-2p of the AIM treated AIM (c); The relationship between atomic concentration of Ca and the AIM treated times (d); The XRD spectra of the non-treated ZrO_2 nanotubular arrays and the AIM treated ZrO_2 nanotubular arrays (e).

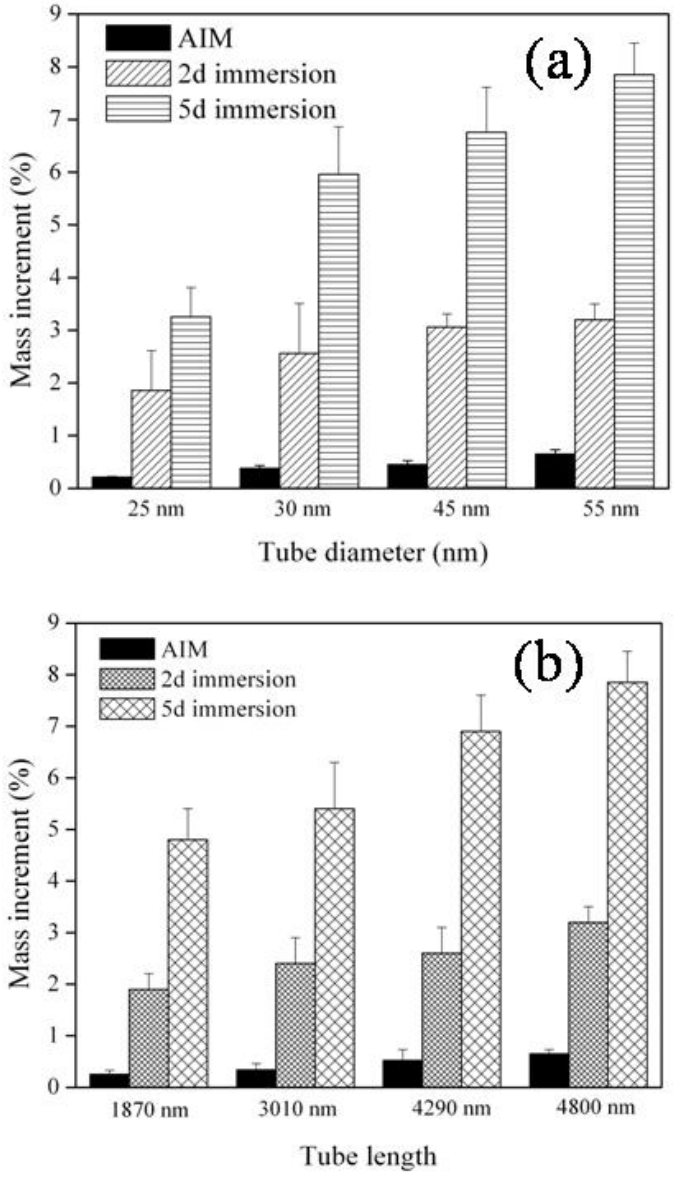

Figure 6-4 Dependence of weight gain of the samples on the tube diameter (a) and the tube length (b) after HA loading by AIM and immersion in SBF for 2 days and 5 days.

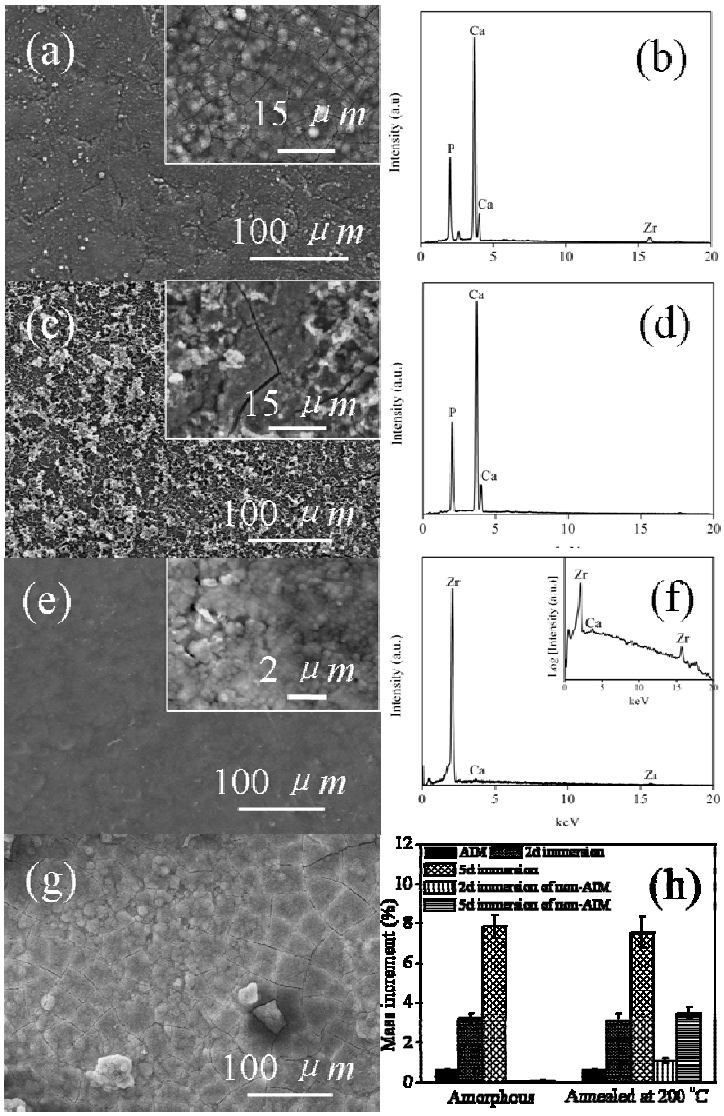

Figure 6-5 SEM images of the AIM-treated samples immersion in SBF for 2d (a) and the corresponding EDX spectrum (b); 5 d (c) and the corresponding EDX spectrum (d); the annealed sample immersion in SBF for 5 d (e) and the corresponding EDX spectrum (f); the annealed sample after AIM treatment and immersion in SBF for 5d (g) and the weight gain of the non-annealed and annealed samples after soaking in SBF for 2 and 5 d with and without AIM treatment (h).

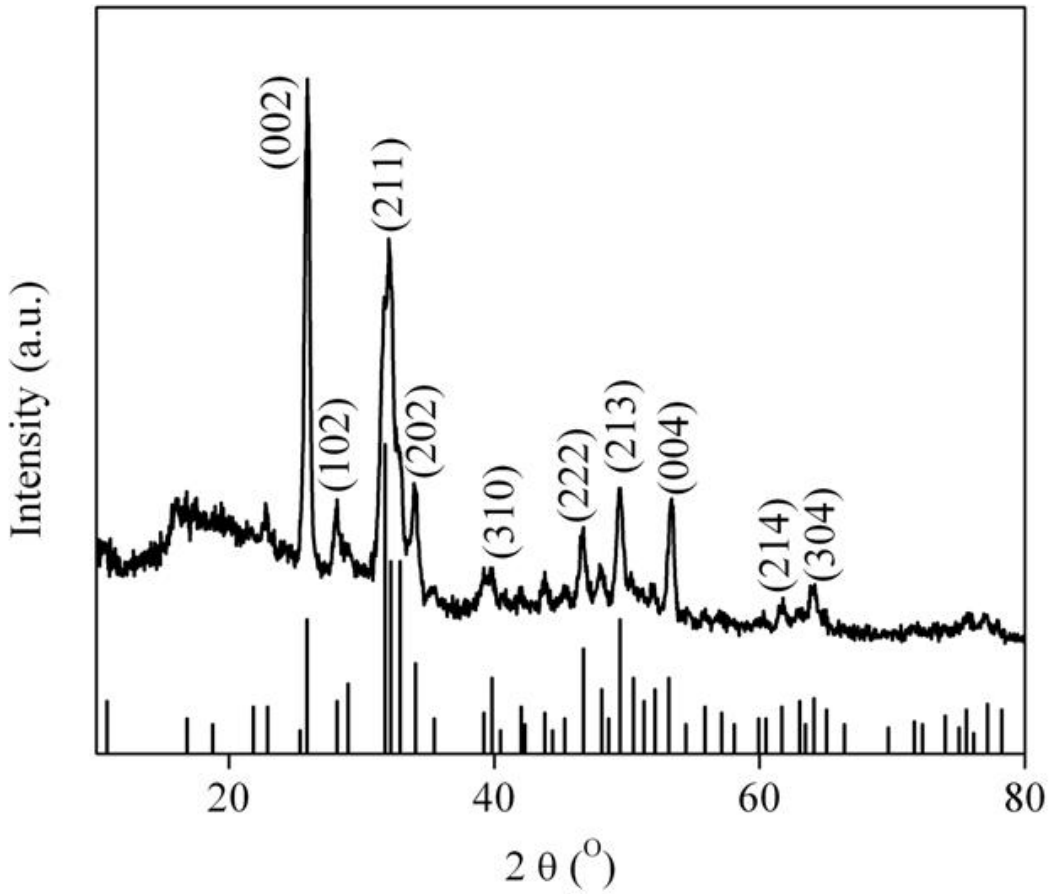

Figure 6-6 The XRD spectrum of the scratched HA coating after 5 days immersion in SBF.

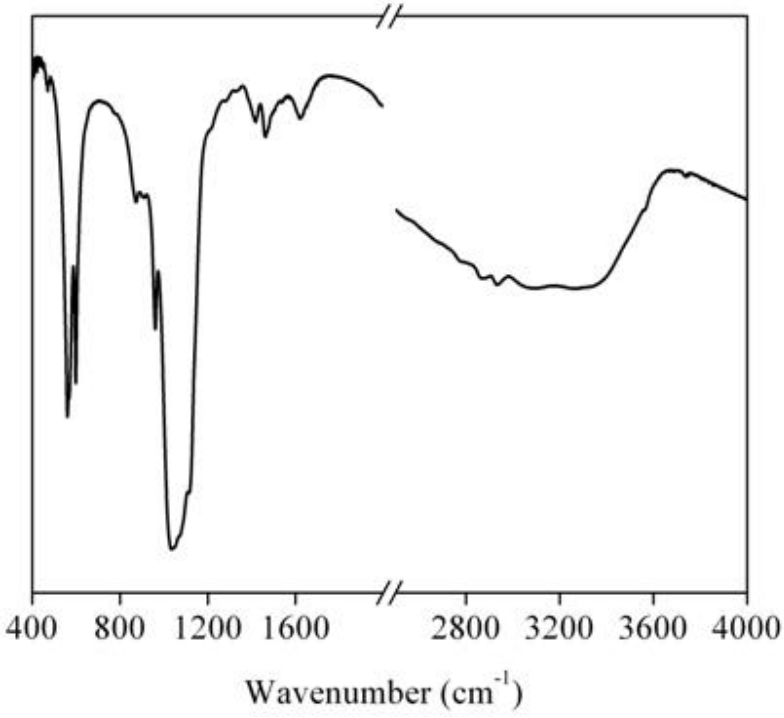

Figure 6-7 FT-IR spectrum of the HA coating after immersion in SBF for 5days.

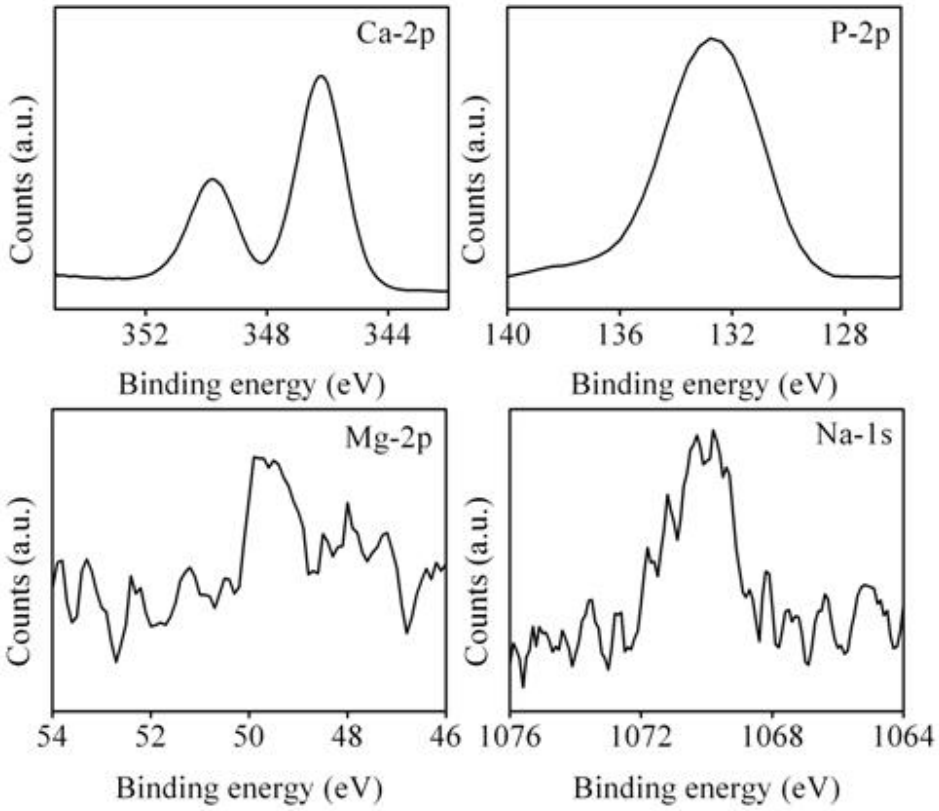

Figure 6-8 XPS P2p, Ca2p, Mg 2p and Na 1s peaks recorded from the HA coating that was grown in SBF for 5 days.

References

[1] A. Kodama, S. Bauer, A. Komatsu, H. Asoh, S. Ono, P. Schmuki, Bioactivation of titanium surfaces using coatings of TiO_2 nanotubes rapidly pre-loaded with synthetic hydroxyapatite, Acta Biomater. 5 (2009) 2322-2330.

[2] W. Lee, W. H. Smyrl, Oxide nanotube arrays fabricated by anodizing processes for advanced material application Curr. App. Phys. 8 (2008) 818-821.

[3] G. E. Thompson, G. C. Wood, Porous anodic film formation on aluminium, Nature 290 (1981) 230-232.

[4] J. Kunze, L. Müller, J. M. Macak, P. Greil, P. Schmuki, F. A. Müller, Time-dependent growth of biomimetic apatite on anodic TiO2 nanotubes, Electrochim. Acta 53 (2008) 6995-7003.

[5] F. H. Lin, C. C. Lin, C. M. Lu, H. C. Liu, J. S, Sun, C. Y. Wang, Mechanical properties and histological evaluation of sintered β-$Ca_2P_2O_7$ with $Na_4P_2O_7 \cdot 10H_2O$ addition, Biomaterials 16 (1995) 793-802.

[6] JCPDS 09-0432.

[7] A. Stoch, W. Jastrzebski, A. Brozek, J. Stoch, J. Szatraniec, B. Trybalska, G. Knita, FTIR absorption–reflection study of biomimetic growth of phosphates on titanium implants, J. Molec. Str. 555 (2000) 375-382.

[8] H. Tsuchiya, J. M. Macak, L. Müller, J. Kunze, F. A. Müller, P. Greil, S. Virtanen, P. Schmuki, Hydroxyapatite growth on anodic TiO_2 nanotubes, J. Biomed.

Mater. Res. 77A (2005) 534-541.

[9] L. Müller, F. A. Müller, Preparation of SBF with different HCO_3^- content and its influence on the composition of biomimetic apatites, Acta Biomater. 2 (2006) 181-189.

Chapter 7 Enhancing the bioactivity of zirconium with the coating of anodized ZrO_2 nanotubular arrays prepared in phosphate containing electrolyte*

7.1 Introduction

Some ions, such as phosphorous and sulfur ions have been reported to be incorporated to metallic substrate by anodization via tailoring the anodization electrolyte. Additionally, phosphorous species, such as HPO_4^{2-} and $H_2PO_4^-$ is essential for formation of hydroxyapatite coating via chemical immersion. [1,2] Therefore, in the present chapter, we examined the formation of self-organized ZrO_2 nanotubes in electrolyte containing predetermined amounts of phosphorous species. A key reason to study the formation in phosphate containing electrolyte is that the phosphorous species may be incorporated within the nanotubular layer and thereby highly enhance its bioactivity to rapidly form HA coating on the as-formed ZrO_2 nanotubular arrays.

7.2 Materials and methods

Anodization of Zr was conducted in a two-electrode electrochemical cell with a platinum foil applied as the counter electrode. The electrolyte was ethylene glycol

* Material in this chapter has been published in:
L. N. Wang and J. L. Luo, Electrochem. Comm. 12 (2010) 1559-1562.

containing 5 vol% H_2O, 0.35 M NH_4F and 0.05 M $(NH_4)_2HPO_4$, prepared using reagent grade chemicals and DI water. For comparison purposes, some samples were anodized in a phosphate-free electrolyte containing the same amounts of H_2O and NH_4F.

7.3 Results and discussions

ZrO_2 nanotubular arrays were synthesized at various applied voltages over different anodization periods. Figure 7-1 shows an example of the nanotubes formed at 30 V for 1 h. The cross section view is shown in Figure 7-1a, and the inserted figure shows a higher magnification view. The layer thickness is about 12 μm. Figure 7-1b shows a top view of the tubular layer with tube opening with an average individual tube diameter of about 75 nm. The layer thickness and the opening of tubes can be easily adjusted by changing the applied voltage and duration. Figures 7-1c and 7-1d compare TEM images of the ZrO_2 nanotubular arrays fabricated in phosphate containing and phosphate-free electrolyte. Both nanotubular arrays formed in the different electrolytes had the same inner diameter, 75 nm. Inserted diffraction patterns demonstrate that both of the as-formed nanotubes are amorphous. The tube openings and layer thicknesses formed at voltages ranging from 15 to 30 V, obtained from SEM on the ZrO_2 nanotubular layers, are compiled in Figure 7-2. Figure 7-2a shows that the layer thickness and diameter of the opening of the tubes depend linearly on the applied voltage. Figure

7-2b shows the relationship between nanotubular layer thickness and anodization time under 30 V for 1h anodization. The layer thickness linearly increases. The linear tendency is consistent with the previous report of the growth of ZrO_2 in HF containing electrolyte [3-4], and the difference in the growth rate can be attributed to the different electrolyte composition since ZrO_2 in aqueous HF has a higher oxidation rate than that in the electrolyte used in this work.

Chemical compositions of the anodic ZrO_2 nanotubular layers formed in phosphate containing electrolyte were characterized using XPS (Figure 7-3a). The C-1s peak at 284.6 eV was used as a reference binding energy for calibration. The spectrum revealed dominant peaks of Zr, O, and F along with a C-1s peak due to the presence of hydrocarbon species as surface contamination. The Zr-$3d_{5/2}$ and Zr-$3d_{3/2}$ peaks have binding energies of 183 eV and 185 eV, respectively, which represent the fully oxidized zirconium ion in its Zr^{4+} state (Figure 7-3b) [5]. The O-1s and the F-1s peaks were at 531 eV and 685 eV, respectively. Evidently, in the as-formed anodic ZrO_2 nanotubes, there are significant amounts of fluorine species. Remarkably, the layers contain phosphate species. The P-2p high-resolution spectrum is shown in Figure 7-3c, with a peak at binding energy of 133.8 eV assigned to phosphate-type species, such as HPO_4^{2-} [9]. Quantitative evaluation showed the presence of 8 at% P on the surface, which indicated very strong adsorption of phosphate species on the surface. XPS data showed that phosphate was embedded in the anodic ZrO_2. The phosphate was distributed almost

homogeneously over the entire tubular length, as evident from consistent levels of ToF-SIMS measurements of phosphate signal over a cross-section of the nanotubular structure of ZrO_2 nanotubular arrays (Figure 7-3d).

The phosphate content of ZrO_2 nanotubular arrays highly enhanced their bioactivity to form HA coating. Figure 7-4 shows the surface morphologies of the ZrO_2 nanotubular arrays prepared in different electrolytes after soaking in SBF for 8 days. There was an obvious layer formed on the surface of ZrO_2 nanotube arrays obtained in the phosphate containing electrolyte (Figure 7-4a). The morphology was very similar to that of the deposited HA on a substrate through biomimetic deposition in SBF [6]. EDX spectra showed the presence of Ca and P on the surface of the ZrO_2 nanotubular layer (insert in Figure 7-4a). However, there was no obvious intact layer, but instead some agglomerated particles formed on the surface of the ZrO_2 nanotubular arrays which were fabricated in phosphate-free solutions (Figure 7-4b). Under higher magnification the only detectable features are a nanotubular structure and a very thin layer on the top the openings of tubular arrays, which demonstrated the poor capability of the HA formation in SBF. Figure 7-4c – 7-4e shows the XRD pattern of the intact Zr, ZrO_2 nanotubular arrays and the layer shown in Figure 7-4a. As can be seen from Figures 7-4c and 7-4d, no peaks were present except for those attributable to zirconium metal, both before and after anodization. However, broad halo patterns (Figure 7-4d) attributed to an amorphous phase were observed at around $2\theta = 30°$. The XRD spectra indicated

that the as formed ZrO_2 nanotubular layer was amorphous, consistent with the TEM diffraction pattern (Figure 7-1c). Comparing XRD data (Figure 7-4e) with the standard profile (JCPDS 09-432) showed that the layer formed on the surface of the ZrO_2 nanotubular arrays was HA.

ZrO_2 nanotubular arrays formed in phosphate-free had poor capability for HA formation in SBF, in contrast to those formed in fluoride containing electrolyte solution with a low concentration of phosphate species. TEM diffraction and XRD data showed that ZrO_2 nanotubular arrays were amorphous, and there was no new material formed in the nanotube arrays prepared in phosphate containing electrolyte.

From these data we conclude that the unique reason for the HA forming ability of the ZrO_2 nanotubular arrays was HPO_4^{2-} incorporation into the nanotubes by diffusion in the electrical field [7]. After rinsing and drying of ZrO_2 nanotubular arrays, HPO_4^{2-} ions remained adhered to the walls of tubes by physical adsorption. XPS of the material supported the proposed reason. After soaking in SBF, HPO_4^{2-} ions adhering to the walls of tubes can deprotonate to form PO_4^{3-} ions in the solution, and the mobilized ions may move to the nanotubular surface. Ca^{2+} ions then are absorbed around the PO_4^{3-} by electrostatic attraction, resulting in a higher supersaturation of calcium and phosphorous at the interface of specimen and solution than that of ZrO_2 nanotubular arrays without HPO_4^{2-} incorporated. The enhancement of the supersaturation at the interface induces the nucleation of HA.

Once the HA nuclei are formed, they spontaneously grow by consuming the calcium and phosphate ions from SBF. As a result, HA nucleates and grows on the ZrO_2 nanotubular arrays.

7.4 Conclusions

Anodic oxidation in phosphate containing electrolyte is an effective way to prepare bioactive ZrO_2 nanotubular arrays. Zirconium oxide nanotubes are formed in phosphate/fluoride electrolytes. Under different potentials from 15 V to 30 V at an anodization period of 1h, self-organized nanotubular structures with diameters from 35 nm to 75 nm and lengths from 2 μm to 12 μm are formed, the dimensions depending on the conditions. The surfaces of the nanotubular arrays so made contain a certain phosphate species and these enhance the bioactivity for formation of hydroxyapatite (HA) coatings in simulated biological culture. Bioactive evaluation shows that HA coating is formed on ZrO_2 nanotubular arrays during 8 days immersion in SBF.

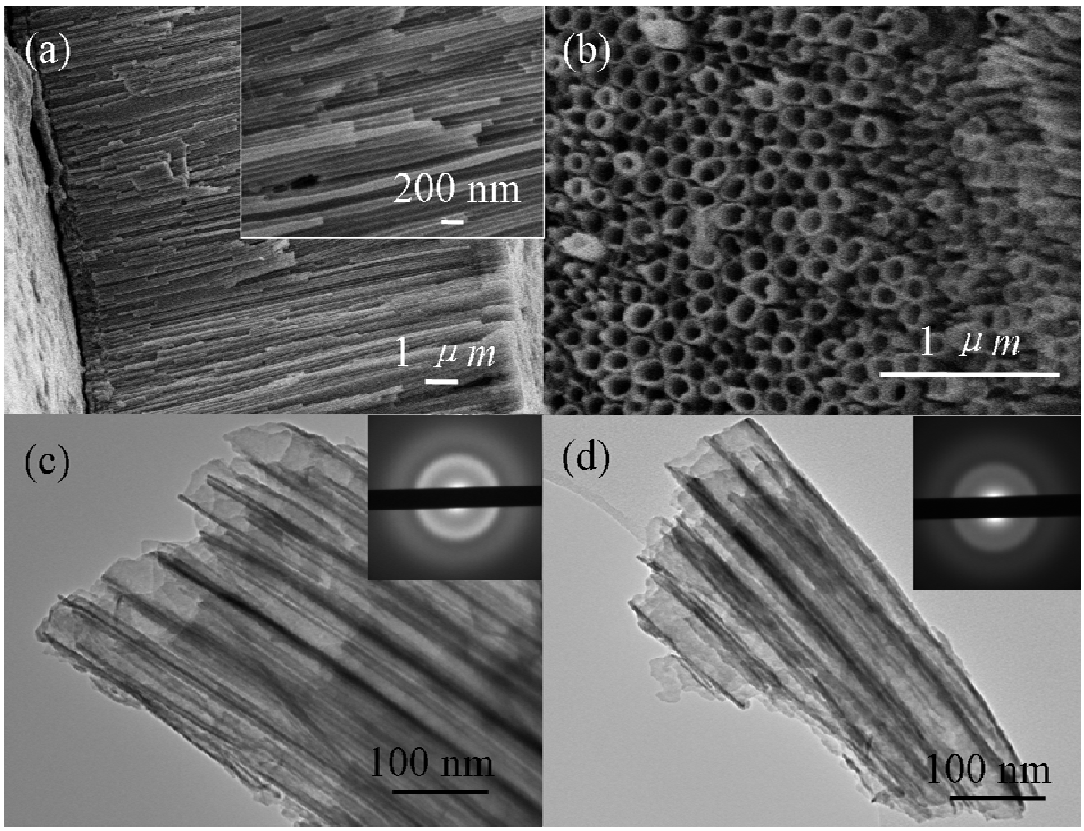

Figure 7-1 SEM images of ZrO_2 nanotubular arrays formed at 30 V for 1 h in ethylene glycerin containing 5 vol% H_2O, 0.35 M NH_4F and 0.05 M $(NH_4)_2HPO_4$: (a) cross-section and (b) top view; and TEM images of ZrO_2 nanotubular arrays formed in glycerin containing 5 vol% H_2O, 0.35 M NH_4F (c) with and (d) without 0.05 M $(NH_4)_2HPO_4$.

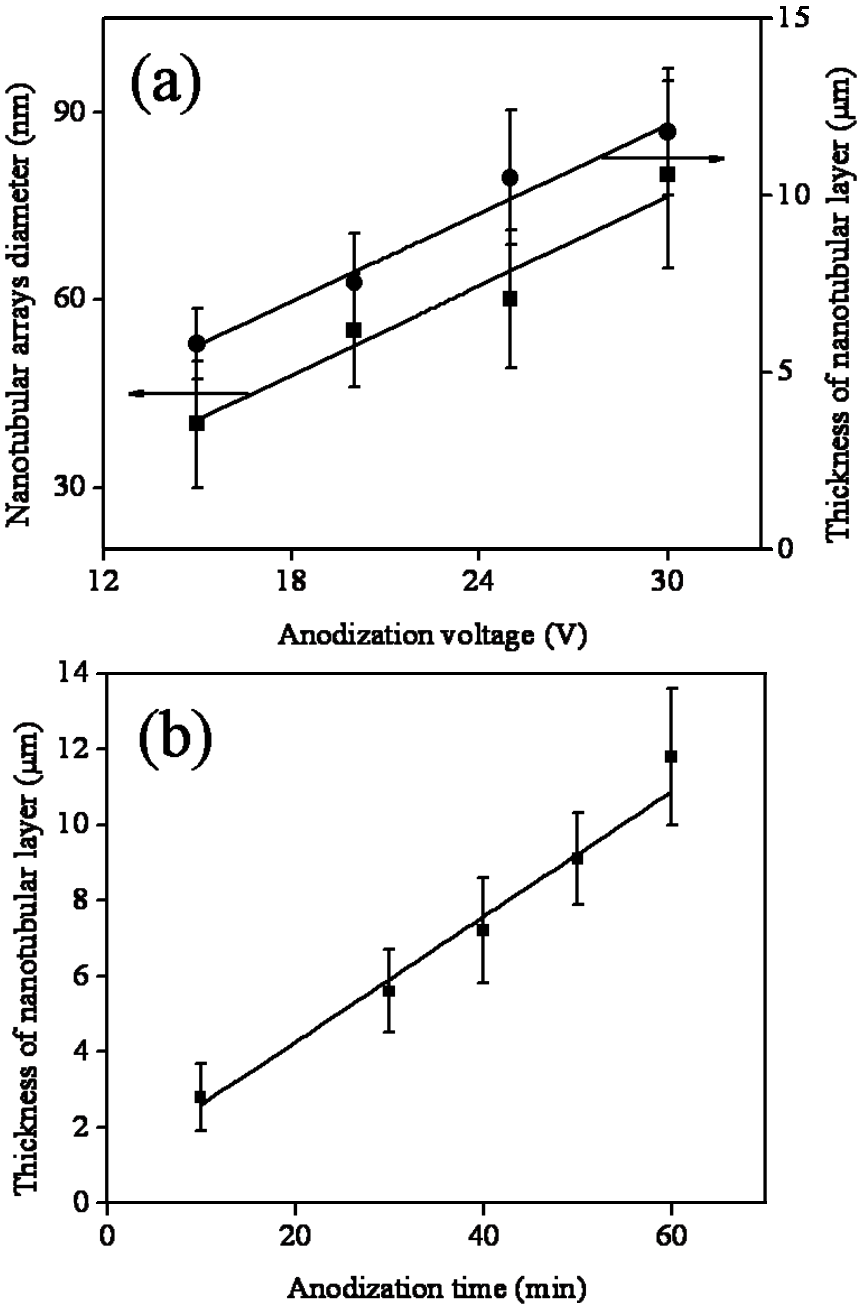

Figure 7-2 (a) Influence of applied voltage on the nanotubular arrays diameter and layer thickness, and (b) dependence of ZrO_2 nanotubular thickness on the anodization period at 30 V.

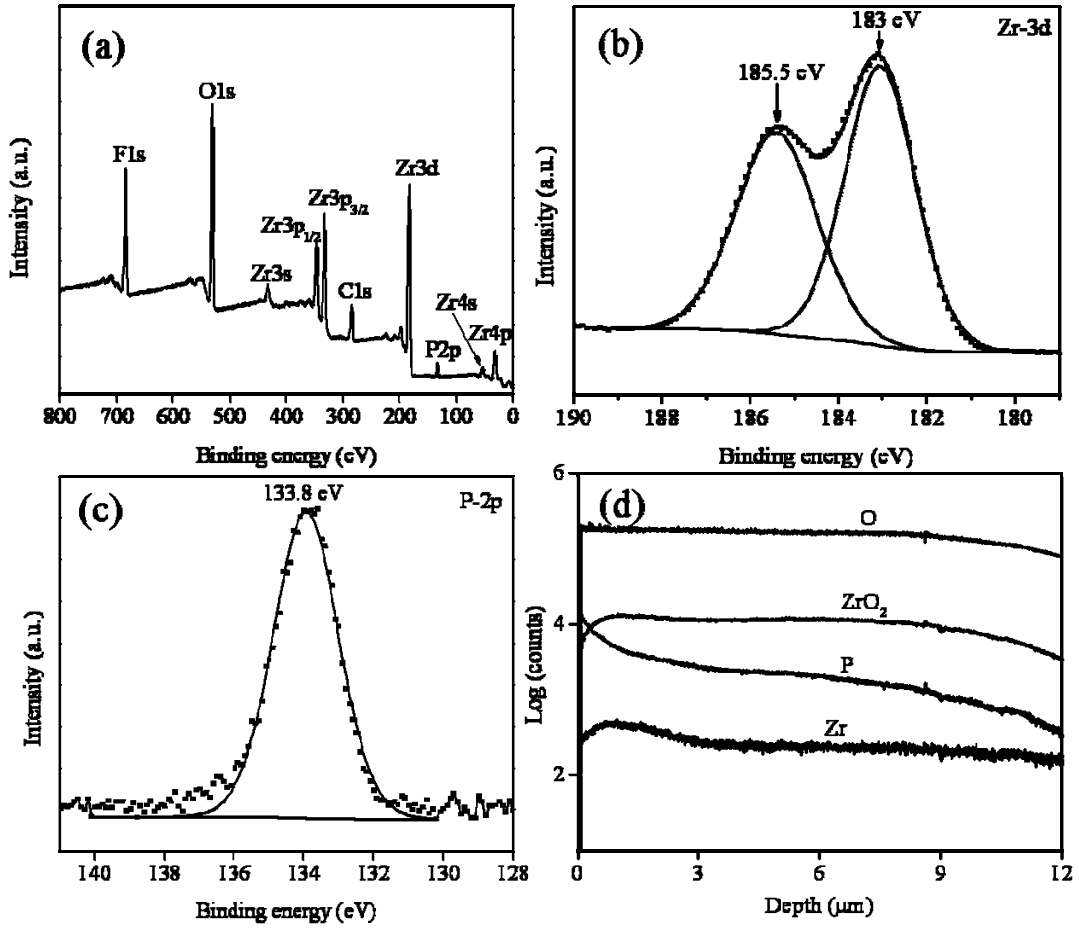

Figure 7-3 A survey of XPS spectra of anodic ZrO_2 nanotubular arrays obtained in: (a) glycerin containing 5 vol% H_2O, 0.35 M NH_4F and (b) 0.05 M $(NH_4)_2HPO_4$; (c) XPS spectra of Zr-3d and P-2p; and (d) ToF-SIMS over the cross section of the ZrO_2 nanotubular arrays.

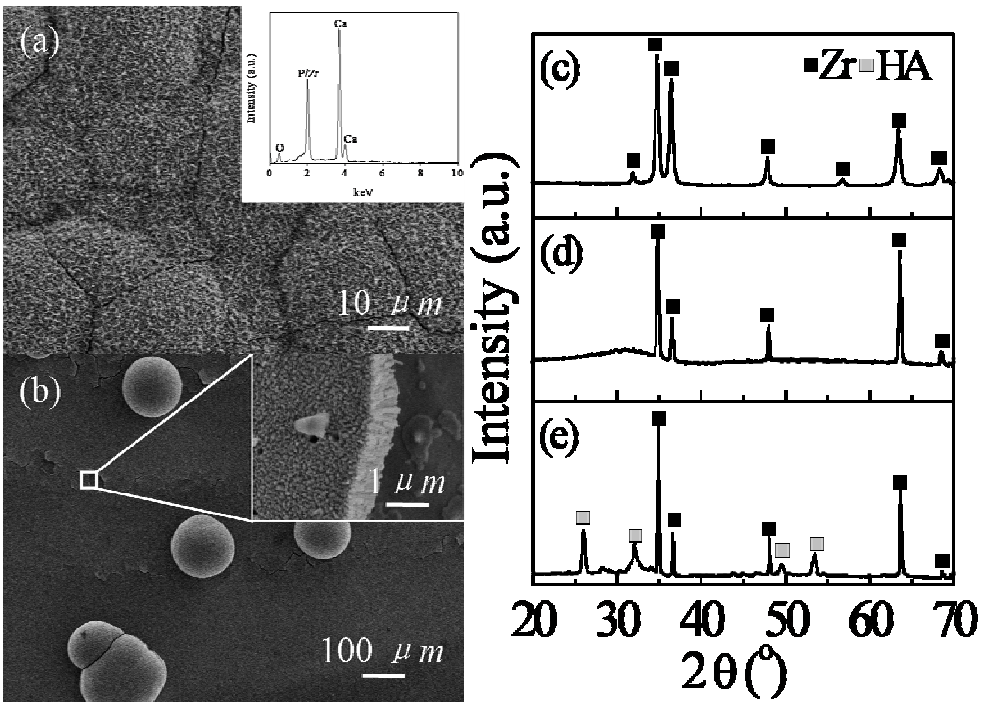

Figure 7-4 SEM images of ZrO_2 nanotubular arrays formed in (a) phosphate-containing and (b) phosphate-free electrolytes after soaking in SBF for 8 days, the inserted figure showing the EDX spectrum; (c) XRD profile of intact Zr, (d) anodized ZrO_2 nanotubular arrays, (e) HA coating formed on ZrO_2 after soaking in SBF for 8 days.

References

[1] H. Tsuchiya, J. M. Macak, L. Taveira, P. Schmuki, Fabrication and characterization of smooth high aspect ratio zirconia nanotubes, Chem. Phy. Lett. 410 (2005) 188-191.

[2] Y. Zhang, W. Fu, H. Yang, S. Liu, P. Sun, M. Yuan, D. Ma, W. Zhao, Y. Sui, M. Li, Y. Li, Synthesis and characterization of P-doped TiO_2 nanotubes, Thin Solid Film 518 (2009) 99-103.

[3] W. Lee, W. H. Smyrl, Zirconium Oxide Nanotubes Synthesized via Direct Electrochemical Anodization, Electrochem. Solid-State Lett. 8 (2005) B7-B9.

[4] Y. Shin, S. Lee, A freestanding membrane of highly ordered anodic ZrO2 nanotube arrays, Nanotech. 20 (2009) 105301, 6pp.

[5] D. Krupa, J. Baszkiewicz, J. A. Kozubowski, A. Barcz, J. W. Sobczak, A. Bilinski, M. Lewandowska-Szumie, B. Rajchel, Effect of calcium-ion implantation on the corrosion resistance and biocompatibility of titanium, Biomaterials 22 (2001) 2139-2151.

[6] L. Müller, F. A. Müller, Preparation of SBF with different HCO_3^- content and its influence on the composition of biomimetic apatites, Acta Biomater. 2 (2006) 181-189.

[7] X. Xiao, R. Liu, T. Tian, Preparation of bioactive titania nanotube arrays in HF/Na_2HPO_4 electrolyte, J. Alloys Com 466 (2008) 356-362.

Chapter 8 Summary and future directions

8.1 Main conclusions

As stated in Chapter 2, an objective of the present work is to synthesize *in situ* zirconium dioxide (ZrO_2) nanotubular arrays on Zr via electrochemical anodization technique, thus providing the mechanical properties of such nanotubular structures. Meanwhile, several wet chemical techniques have been applied to modify the *in vitro* biocompatibility of ZrO_2 nanotubular arrays in terms of formation capability of hydroxyapatite (HA) coating in simulated biological culture. The following main conclusions can be made on the basis of the separate investigations of these aspects:

(1) Highly ordered ZrO_2 nanotubular arrays are fabricated in fluoride containing electrolyte. The geometrical factors of anodic ZrO_2 nanotubular arrays, such as thickness and tubular diameter, are linearly dependent on the applied voltage. The growth of nanotubular arrays has two stages: acceleration stage and equilibrium stage. Mechanical properties of ZrO_2 nanotubular arrays such as Young's modulus, W_e/W_{tot}, hardness, and wear resistance rely strongly on the thickness of nanotubular arrays. Further, the wear resistance of ZrO_2 nanotubular arrays is highly affected not only by the surrounding dry and wet environments but also by the acidic and alkali nature of the wetting condition.

(2) Several wet chemical techniques can be employed on ZrO_2 nanotubular arrays

efficiently to obtain bioactive HA coating, and the rate of formation of HA coating is enhanced several fold (within 8 days compared to 4 weeks).

A dipping wet chemistry pretreatment enhances the capability for formation of hydroxyapatite (HA) coating on ZrO_2 nanotubular arrays. The pretreatment process includes several dip-and-dry stages in a calcium and phosphate containing solution, resulting a full coverage of calcium phosphate crystallites on the ZrO_2 nanotubular arrays. The HA coating forms on the treated ZrO_2 nanotubular arrays within 8 days. Additionally, this HA coating has mechanically strong bonding strength to the substrate.

A presynthesized HA thin layer formed using an alternative immersion method (AIM) has been developed to enhance the bioactivation of ZrO_2 nanotubular arrays in simulated biological culture. The presynthesized HA thin layer also promises the formation of HA coating shortly after 5 days immersion in SBF.

(3) By tailoring the electrolyte composition, bioactive ZrO_2 nanotubular arrays also can be fabricated by electrochemical anodization in phosphate containing electrolyte. The surfaces of the nanotubular arrays so made contain phosphate species and these enhance the bioactivity and quickly induce formation of hydroxyapatite (HA) coatings in simulated biological culture.

8.2 Contributions to the knowledge

Based on the experimental results and analyses conducted during this work, the

following papers have been published, accepted, submitted, or are in preparation:

(1) L. N. Wang, J. L. Luo, Enhancing the bioactivity of zirconium with the coating of anodized ZrO_2 nanotubular arrays prepared in phosphate containing electrolyte, Electrochem. Comm. 12 (2010) 1559–1562,

(2) L. N. Wang, J. L. Luo, Formation of Hydroxyapatite Coating on Anodic Titanium Dioxide Nanotubular via an Efficient Dipping Treatment, Metall. Mater. Trans. A, DOI: 10.1007/s11661-010-0484-z,

(3) L. N. Wang, J. L. Luo, Fabrication and formation of bioactive anodic zirconium oxide nanotubes containing presynthesized hydroxyapatite via alternative immersion method, Mater. Sci. Eng. C 31 (2011) 748-754,

(4) L. N. Wang, J. L. Luo, Fabrication and Mechanical Characterization of Anodic ZrO_2 nanotubular arrays, J. Phys. D: Appl. Phys. 44 (2011) 075301,

(5) L. N. Wang, J. L. Luo, Enhancement of the capability of hydroxyapatite formation on Zr with anodic ZrO_2 nanotubular arrays via an effective dipping pretreatment, J. Biomed. Mater. Res. B accepted,

(6) Lu-Ning Wang and Jing-Li Luo, “Preparation of calcium phosphate coatings on CoCrMo implants using an effective electrochemical and chemical approach,” Mater. Character. under review,

(7) L. N. Wang and J. L. Luo, Enhancement of hydroxyapatite formation on anodic TiO_2 nanotubular arrays via precalcification, in preparation.

8.3 Recommendations for future work

The investigations conducted in the present work show that the materials developed are attractive and interesting for biomedical applications of anodic nanotubular arrays. Nevertheless, some experimental phenomena and mechanisms

remain subjects for debate, and further experimental investigations are required to more fully elucidate these phenomena. Based on the results acquired from this research, the following suggestions are made for future work.

(1) Optimization of the geometry and mechanical properties of anodic ZrO_2 nanotubular arrays: In the present work we showed the fabrication, geometry, and mechanical properties of ZrO_2 nanotubular arrays under certain applied voltage and electrolyte conditions. The optimum geometry with proper mechanical properties of ZrO_2 nanotubular arrays for different biomedical applications is not yet known.

(2) Biocompatibility of ZrO_2 nanotubular arrays in cell cultures: In this thesis, we showed that ZrO_2 nanotubular arrays with wet chemistry pretreatment have superior capability for hydroxyapatite coating formation in simulated biological culture. Nanotubular arrays immersed in *in vivo* cultures have to contact the cellular culture. The interactions of such pretreated ZrO_2 nanotubular arrays with cells are not yet understood. A detailed cellular culture test is suggested for further study.

(3) Size effect of ZrO_2 nanotubular arrays for biomedical applications: It was shown in the present work that nanotubular arrays with diameter over 50 nm with longer thickness show better capability to provide larger volume to form HA coating. Considering different sizes of cell and bony tissue *in vivo*, ZrO_2 nanotubular arrays with varied size may influence the biocompatibility. Thus impact of different sizes of ZrO_2 nanotubular arrays should be studied with respect to interactions with cell cultures and *in vivo* conditions.

(4) Effect of electrolyte composition on biocompatibility of the anodic ZrO_2 nanotubular arrays: The preliminary studies herein indicate that phosphate species highly improve the biocompatibility in terms of HA coating formation. A wider range of phosphate compositions and electrochemical conditions for the fabrication of such ZrO_2 nanotubular arrays has to be studied. Additionally, such nanotubular arrays have to be proved to have proper biocompatibility by *in vivo* test.

Appendix I Formation of Hydroxyapatite Coating on Anodic Titanium Dioxide Nanotubes via an Efficient Dipping Treatment *

AI.1 Introduction

Titanium and its alloys are widely applied in orthopaedic and orthodontic implants owing to their excellent mechanical properties, adequate corrosion resistance, and good biocompatibility [1-4]. Moreover, titanium and its alloys are bioinert materials, which can be covered by the host organism without being integrated with bone [5-6]. Thus surface modification on titanium and its alloys was required and has been reported during the last several decades [7-9]. For example, chemical etching in either acidic or alkaline solutions or anodization above breakdown potential to obtain a porous structure were reported by numerous groups [10-15]. Besides the etching and oxidation modification methods, different calcium phosphates (CaP), such as hydroxyapatite (HA, $Ca_{10}(PO_4)_6(OH)_2$), has been used often as a coating on titanium to improve its biocompatibility [7, 16-18]. The plasma-sprayed HA coated titanium alloys have been clinically applied [19-21]. However reports describe the difficulty of controlling the quality, composition, and crystallinity of plasma sprayed HA coatings [22-24]. An alternative immersion method (AIM) was recently reported to form calcium phosphate coating by dipping

* Material in this chapter has been published in:
L. N. Wang and J. L. Luo, Metal. Mater. Trans. A. DOI:10.1007/s11661-010-0484-z

and withdrawing the metallic implant in $Ca(OH)_2$ and $(NH_4)_2HPO_4$ solutions for various times, resulting in HA covered surfaces. This method was applied to efficiently deposit synthetic HA after short term immersion and can be applied on various porous metallic substrates such as aluminum and magnesium [25].

Anodic oxidation is increasingly applied for surface treatment on titanium and its alloys to obtain nanotube structures at the surface. During the last decade, there have been numerous studies on the formation of TiO_2 nanotube by anodization [26-30]. It was reported that the tubes with lengths ranging between 15-500 nm with about several microns thickness could be grown under anodic potentials range from 1-20 V in F^- containing acidic electrolyte [26, 27], resulting in TiO_2 nanotubes possessing a hollow structure for filling with bioactivating species and providing an interface suitable for anchoring connective tissue. It was reported that the TiO_2 nanotubes have many potential biomedical applications, for example, use as a bond scale and supporting platform for bone and stem cells, local delivery of antibiotics off-implant at the site of implantation, and the control of hemorrhaging by forming significantly stronger clots with reduced clotting times [31-33]. Recently, HA coatings on TiO_2 nanotubes were developed for biomedical applications. It has been reported that HA coating was formed on the annealed TiO_2 nanotubes by immersion in 1.5 SBF (simulated biological fluid with 1.5 times of Ca and P concentration than standard SBF) for 2 days. The resulting HA coating, however, was only about 10 nm thick [30]. Another study reported that HA could form on the

titania nanotubes array when it was subjected to immersion in 5 M NaOH at 60 ^{o}C for 24 h or saturated $Ca(OH)_2$ for 6 h followed by immersion in SBF [34]. However, there was a concern that the as-formed nanotubes structure were dissolved or destroyed during the alkaline treatment and it was difficult to identify the role of the damaged nanotube structure in the formation of HA.

It is believed that the nanostructure should be beneficial to tight adhesion of HA coating to titanium substrate and offer larger surface area for the nucleation of calcium and phosphate [35]. Therefore combination of the two methods, which are to apply the dipping method on the anodic TiO_2 nanotube layers and form the HA coating, may form HA on TiO_2 nanotubes more efficiently than either method alone. In the present study, we investigated the possibility of filling the TiO_2 nanotubes with CaP nucleation sites using several dip-and-dry steps at room temperature, and investigated whether the treated tube layers showed an accelerated effect of HA formation when exposed to SBF. The coating was characterized and the mechanism of the formation is discussed.

AI.2 Experimental procedures

AI.2.1 TiO_2 nanotube formation

The sample material was Ti thin foil (99.6% purity, Alfa Aesar, USA) with size of 1 cm × 1 cm and a thickness of 0.5 mm. Prior to anodization, the samples were ground with sandpaper up to 1200 grit and were ultrasonically rinsed with

deionized (DI) water and ethanol for 20 min, sequentially, and then dried using compressed air at room temperature. The titanium specimen was rinsed in saturated H_2SO_4 for 1 min to clean the surface before anodization. Anodization was conducted at room temperature in a two-electrode electrochemical cell with a graphite foil (1 cm × 1cm) used as the counter electrode and 0.5 M H_3PO_4 + 0.5 wt % NaF solution as the electrolyte. A direct current power supply (1715A, B&K Precision Corporation, Yorba Linda, CA) was used as the voltage source to drive reactions involved in the anodization process. A constant 20 V potential was applied over a range of anodization periods. All as-prepared TiO_2 nanotube array films were rinsed using DI water and then dried using compressed air. In order to compare the materials formed using different treatments some anodically treated samples were annealed at 723 K (450 ^oC) and 823 K (550 ^oC) for 3 h in air using a furnace with a heating rate of 10 K/min (10 ^oC/min).

AI.2.2 The dipping method

An accelerated calcium solution (ACS) was prepared by dissolving 8 g NaCl, 0.42 g $CaCl_2$, and 0.27 g $NaHPO_4$ in 1 L DI water [36]. The pH was adjusted to 7.4 by adding appropriate amounts of 1M HCl and tris(hydroxymethyl)aminomethane (tris). The anodically treated specimen were vertically exposed in ACS for approximately 10 s, and withdrawn from the solution with a wetting film remaining on the surface. The samples were placed on a slide glass and left to dry under flowing air for 10 min at room temperature. Every sample was treated up to 8 times

followed by rinsing in DI water and drying in an air stream. The process of the dipping method is shown in Figure AI-1.

AI.2.3 HA formation

The HA formation of anodized TiO_2 nanotubes after dipping treatment was evaluated by immersion tests in a simulated biological fluid (SBF, Table AI.1) [37]. The electrolyte with ionic concentrations similar to human plasma was prepared by dissolving reagent grade NaCl, KCl, $NaHCO_3$, $MgCl_2 \bullet 6H_2O$, Na_2SO_4, $CaCl_2$, and $K_2HPO_4 \bullet 3H_2O$ into DI water and buffered at pH = 7.25 with tris and HCl at 310 K (37 ^oC). The ratio of sample surface to the volume of SBF, S/V, was about 0.01 cm^{-1}. Separate samples were immersed in SBF for 2 days and 4 days without stirring to investigate their bioactivity. After immersion, the samples were removed, rinsed with DI water, and dried in air.

Table AI.1 Ion Concentrations of SBF and Human Blood Plasma

	Concentrations (mM)							
	Na^+	K^+	Mg^{2+}	Ca^{2+}	Cl^-	HCO_3^-	HPO_4^{2-}	SO_4^{2-}
SBF	142.0	5.0	1.5	2.5	148.8	4.2	1.0	0.5
Blood plasma	142.0	5.0	1.5	2.5	103.0	27.0	1.0	0.5

AI.2.4 Surface characterizations

Field emission scanning electron microscopy (FE-SEM) was used to determine surface morphology using a JEOL JSM6301FXV SEM with a FE electron source running at 5 kV and a JEOL field emission JAMP 9500F at 25 kV. X-ray photoelectron spectroscopy (PHI 5600 XPS spectrometer) was used to characterize the chemical composition of the surface. The XPS spectra were recorded using Al Kα radiation (1486.6 eV) as excitation source. The composition and thickness of the TiO_2 nanotubes after dipping treatment were determined through Time of Flight Secondary Ion Mass Spectrometry (ToF-SIMS) using an ION-TOF IV spectrometer. The compositions of the coating were determined with an energy dispersive X-ray spectrometer (EDX) and Fourier transform infrared spectrometer (FT-IR, Nicolet 5700). The crystal structure was determined using a thin film X-ray diffractometer (TF-XRD) with Cu Kα radiation. The bonding strength of the HA layer to the substrate was measured using a method described by Kim *et al.*, which is a modified ASTM C-633-08 method, through an Instron Model 4505 Universal Testing System [38]. Five samples were selected to obtain the bonding strength of the coating layer. Both sides of the sample were fixed to stainless steel square bars using rapid-type LePage® glue, as shown in Figure AI-2. After the glue had fully dried, a continuous tensile load was applied vertical to the sample surfaces using a weight scale. The load (N) at which the coating separated from the substrate was recorded. The bonding strength was calculated by dividing the load at fracture by the sample surface area. The adhesive strength value (MPa) was taken as the

average from five tested samples.

AI.3 Results

AI.3.1 The structure of TiO_2 nanotubes

Figure AI-3 shows examples of TiO_2 nanotubes formed at 20 V for different anodization periods, 20 min (AI-3a), 40 min (AI-3b), and 100 min (AI-3c). The nanotubes have about 100 nm diameters and are distributed on the surface in a regular pattern. The inserted figures in Figures AI-3a-3c portray side views of the cross sections of nanotubes. The tube layers were about 200 nm in thickness when the nanotubes were formed for 20 min, 520 nm after 40 min, and 1.15 μm after 100 min. The samples show that only the thickness, and not the diameter, of the tubes is a function of the anodization time. The thickness of the tubes as a function of anodization time is illustrated in Figure AI-3d. The data show that the growth of TiO_2 nanotubes at 20 V increased rapidly in the initial stage, about 60 min. After the first 60 min, the growth of TiO_2 nanotubes gradually decreased and the nanotube length after anodization for 120 min was 1.22 μm. It is well accepted that the formation of TiO_2 nanotubes in F^- containing solution relies on three spontaneous processes: field assisted oxidation of titanium to form titanium dioxide, field assisted dissolution of titanium dioxide, and chemical dissolution of the TiO_2 by etching with fluoride ions [29, 32, 33]. It is believed that the final thickness of nanotube array is dominated by the dynamic equilibrium between the oxidation and

the dissolution processes. As shown in Figure AI-3d, the diffusion of fluoride anions through the short nanotubes to etch the titanium substrate to develop the TiO_2 nanotubes is relatively facile, as demonstrated in the first 60 min anodization. However, as the tube lengthened, the diffusion of F^- in the tubes became increasingly difficult, with the consequence that longer time was required for ions to reach the bottom of TiO_2 and form the TiO_2 tubes. As a result, the rate of growth of the tubes decreased after 60 min, as shown in Figure AI-3d. Since the tube length did not change much between the anodization periods from 100 min and 120 min, the subsequent aspects of this work used anodized TiO_2 nanotube obtained at 20 V with 120 min.

AI.3.2 Dipping effect on the precipitation on TiO_2 nanotubes

Figure AI-4 shows the top and side view of the nanotubes after dipping twice (AI-4a) and eight times (AI-4b) in ACS solution. It clearly shows that some tubes are filled by deposition only after dipping twice. After eight times of dipping, most of tubes are filled and some tubes are even covered by the precipitations. As shown in side view, one can clearly see the openings of tubes after dipping twice and fully covered surfaces after eight times of dipping. XPS spectra further confirm the deposition of calcium and phosphate species (Figure AI-5a). The quantitative study of the amount of calcium is shown in Figure AI-5b and it suggests that eight times of dipping treatment results in about 4 at% of calcium on the surface. Therefore, for the remaining portion of the study, the standard procedure was eight times of

dipping treatment. Figure AI-6 shows the TOF-SIMS depth profile of the specimen after eight times of dipping treatment. Calcium and phosphate were enriched at the top surface and gradually decreased with depth, which indicated that calcium and phosphate penetrated well into the nanotubes

AI.3.3 Formation of HA coating on TiO_2 nanotubes with dipping treatment

Figure AI-7 shows SEM images of dipping treated TiO_2 nanotubes after soaking in SBF for 2 days and 4 days. It is clearly shown in Figure AI-7a that after 2 days of immersion, the surface of the sample was already covered by a layer of small spherical particles. Figure AI-7b and the inserted figure show the coating morphology and chemical compositions obtained after 4 days of immersion. It shows that the small spherical particles agglomerated to form a dense coating, which were similar to the HA formed in SBF as described by others [26, 39, 40]. The EDX spectra demonstrated that the coating contained mainly Ca and P, and there was no peak for Ti which indicated that the coating thickness was of the order of micrometers since there was no information from the substrate. For comparison purposes, separate samples of TiO_2 nanotubes were annealed for 723 K (450 ^{o}C) (Figure AI-8a) and 823 K (550 ^{o}C) (Figure AI-8c), and then immersed in SBF for 4 days. Their morphologies and the corresponding EDX spectra are shown in Figures AI-8b and AI-8d. The nanotubes annealed at both temperatures were covered by very thin layers and both EDX spectra showed mainly Ti peaks while the peaks for Ca and P were weak, which indicated that only a minor amount of calcium and

phosphate was deposited on the surfaces. Figure AI-9 shows the TF-XRD results of the surfaces with different immersion periods in SBF. Figure AI-9a shows the spectrum of the intact substrate before immersion in SBF. The HA was detectable using TF-XRD after 2 days of immersion (AI-9b). With prolongation of immersion time, the peaks of Ti gradually became weaker compared to those of HA, as shown in (AI-9c), which indicated that calcium and phosphate were deposited onto the surface, formed HA crystals and HA became thicker with immersion time. Figure AI-10 shows the FTIR spectrum of the HA coatings obtained after 4 days of immersion in SBF. The characteristic peaks of phosphate groups, molecular and adsorbed water bands and hydroxyl groups became apparent in the spectrum, as summarized in Table AI.2. Moreover, carbonate bands also were detected at 1420 and 1460 cm^{-1}. Therefore, the coating is carbonated HA [41, 42].

AI.3.4 The bonding strength of the HA coating

The bonding strength of the HA coating on TiO_2 nanotubes after 4 days of immersion in SBF was evaluated using the method described in Section 2.4. The bonding strength of the HA coating on titanium dioxide nanotubes was 27.2 ± 1.6 MPa. It was reported that bonding strengths of HA coatings on Bioglass and glass-ceramic-A-W were less then 10 MPa [38]. Figure AI-11 compares bonding strengths of our result with others (AI-11a), the SEM morphology (AI-11b) and the EDX mapping of different elements, Ca, P, and Ti, on the fracture surfaces of substrates (AI-11c-11e). The bonding strength in this work, 27.2 MPa, is higher

than the value, 15 MPa, of the ISO standard 13779-2:2008 [43] for surgery apatite coating implants. From the EDX mapping, it can be seen that the intensities of reflected Ca and P peaks are strong on the fractured surface of the substrate, and Ti was hardly detected, which indicated that the HA adhered well to the substrate and the fracture happened within the HA coating layer but not along the interface between HA and TiO_2 nanotubes.

Table AI.2 Characterization of materials from FTIR spectra

Groups	Wavenumber of vibration peak (cm^{-1})
Bending mode of PO_4^{3-}	474, 567, and 604
Vibration of HPO_4^{2-}	875 and 958
Bending mode of CO_3^{2-}	875
Stretching mode of PO_4^{3-}	960-1200
Vibration of CO_3^{2-} on PO_4^{3-} lattice site	1420 and 1460
Bending mode of H_2O vibration	1645
Vibration of adsorbed H_2O	2500-3600

AI.4 Discussion

In this study, the sequential dipping treatment induced deposition of calcium and phosphate before immersion in SBF and resulted in rapid HA formation on the titanium dioxide nanotubes structures. The mechanism of the dipping treatment tentatively proposed is an evaporation-induced process, shown in Figure AI-12

using a single tube as an example. The initial dipping step leaves a wetting film in the surface. Since the nanotubes structure has a small diameter a large pressure differential is generated across the liquid interface, so the ACS has a high surface tension similar to water and produces a large pressure difference described by the Young-Laplace equation [35]. Thus the ACS can penetrate into the nanotubes due to the capillary effect. Consequently, the wetting film will in-fill and cover the inner wall of the nanotubes. During the drying step, the wetting film gradually evaporates resulting in an increasing supersaturation within the tubes. The supersaturation will induce calcium and phosphate depositions to form CaP crystallites adhering to the inner wall of the TiO_2 nanotubes (e.g. AI-12b). The CaP may also react or interact with the other chemicals, such as NaCl, KCl, tris, etc. in the wetting film. These CaPs can be identified as those non-adhesive CaP particles within the tubes. The next dipping step makes the chemicals dissolve, non-adhesive CaP particles detach, and a new wetting film will form [44]. The repeated dipping treatment thus formed CaP-crystallite-covered inner walls of nanotubes, corresponding to the SIMS spectra shown as Figure AI-6. These CaP crystallites serve as nucleation sites for the generation of HA coating [44].

It was reported by Tsuchiya et al. that HA formed on the annealing TiO_2 nanotubes without pretreatment after 14 days of immersion in SBF [26]. The same group also reported that HA can form on TiO_2 nanotubes over 2 days by applying SBF10 after preloading HA treatment [45]. Feng et al. reported that an HA coating

formed on annealing TiO_2 by immersion in SBF3 for 4 days [35]. From their results, either annealing of as-formed TiO_2 or a saturated simulated biological fluid (SBF10 or SBF3) was required to obtain the HA coating within 4 days. In this study, a typical SBF was used and HA formed on substrate after 2 days and had about 10 μm thickness within 4 days. The data herein indicate that TiO_2 nanotubes after the dipping treatment are fully covered by CaP nucleation sites. Therefore, the surface must have been supersaturated with calcium and phosphate once it was immersed in SBF, ready for the deposition of calcium and phosphate which then was converted rapidly to HA. The obtained HA coating was carbonated-HA after 2 days of immersion. It has been suggested that carbonated HA was formed after immersion in CO_3^{2-} containing SBF. The vibration bands at 1420 and 1460 cm^{-1} showed that CO_3^{2-} was partly substituted for PO_4^{3-}, resulting in the formation of B-type carbonated HA, which is predominant in biological bone tissues [46-48].

The mechanical properties such as tensile bonding strength of the calcium phosphate coating to substrate are important aspects of the coating properties [12]. As shown in Figure AI-11a, the HA coating on TiO_2 nanotubes in this study had high bonding strength and was tightly bonded to the substrate, while remaining HA coating. EDX mapping (AI-11c-11e) also confirmed that the fracture of the coating happened within the HA coating, not between layers. The high bonding strength can be explained as follows. Since the TiO_2 nanotubes are filled with CaP nucleation sites after dipping treatment, the HA formed from the inside of the

nanotubes. The structure of the coating then gradually changed from Ti substrate to TiO_2 nanotubes with HA coatings. The gradual change of the structure resulted in a high bonding strength. It has been reported that after the glass-ceramic A-W with CaP layer was implanted as a rabbit tibia for one month and a tensile stress was applied on the bone, the fracture occurred within the bone but not at the bone-implant surface [49]. This result demonstrated that even the glass-ceramic A-W with CaP layer contained enough bonding strength after implantation. The present work showed that HA coating formed on TiO_2 nanotubes had even higher bonding strength, which indicated that the HA coating with TiO_2 can bond very tightly to the living bone.

AI.5 Conclusions

Titanium dioxide nanotubes structures were fabricated by anodization in F^- containing electrolyte at 20 V. The anodization duration did not affect the nanotube diameter, only the length of the nanotubes. The tube length was increased in the initial stage of anodization and the rate of growth gradually decreased after about 1 h anodization.

A combination treatment with dipping method and anodized TiO_2 nanotubes developed in this work forms strongly bonded coatings. The HA coating readily formed on Ti implant materials with this treatment shortly after 2 days immersion in SBF. After 4 days of immersion in SBF, the HA typically formed spherical

particles that fully covered the surface. FTIR showed that the coating was carbonated HA.

The tensile bonding strength of the HA coating on Ti with TiO_2 nanotubes after 4 day immersion in SBF was about 27.2 ± 1.6 MPa.

The combination of anodization to form TiO_2 nanotubes and the dipping method on Ti implant materials strongly accelerated HA formation on as-formed TiO_2 nanotubes when immersed in SBF. Therefore, the combined treatment was an efficient way to enhance the rate of HA formation on titanium biomaterials. Additionally, the results are consistent with an evaporation based mechanism and resulted in a CaP nucleation sites attached to the TiO_2 nanotubes.

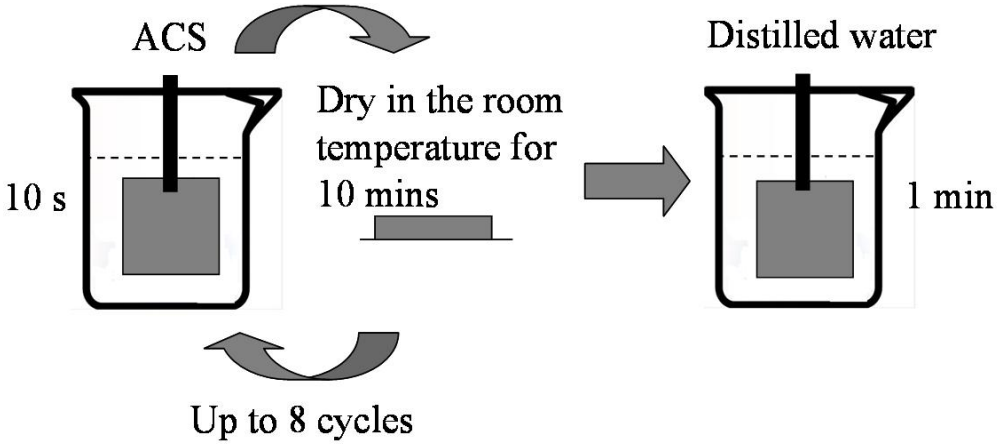

Figure AI-1 Schematic of the procedure for dipping treatment.

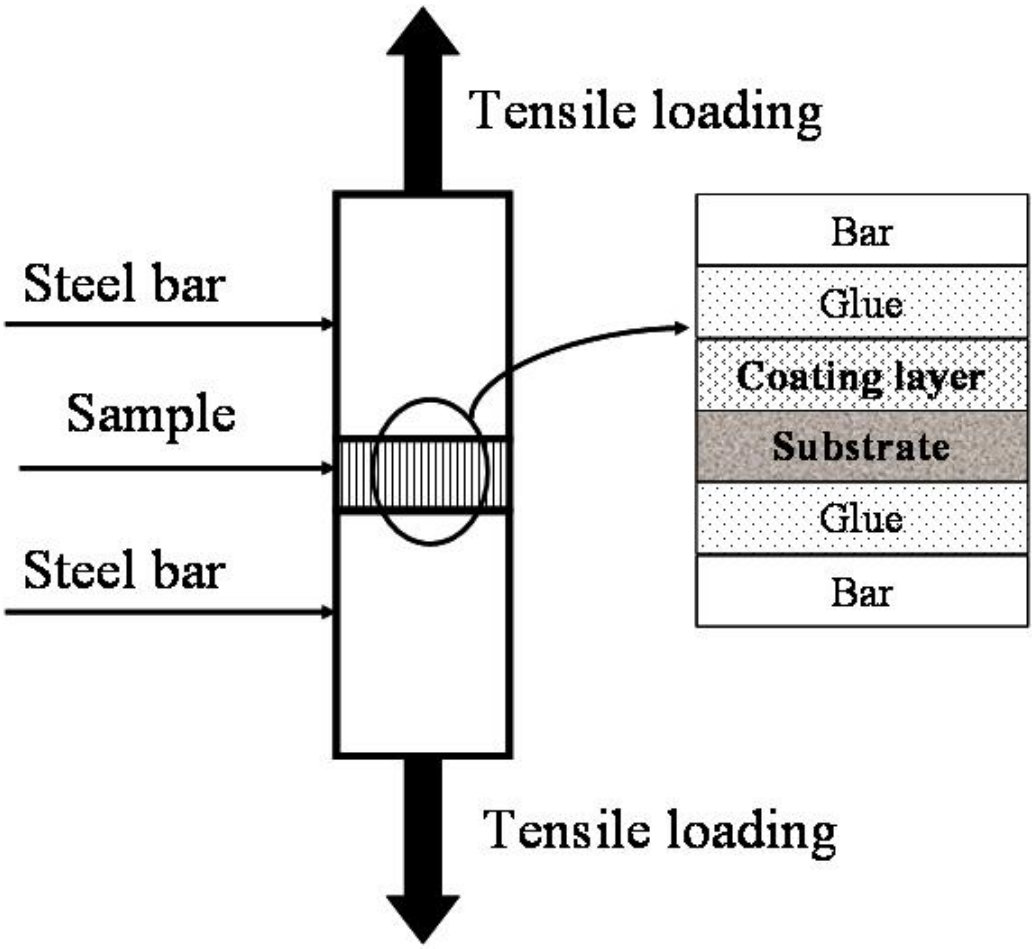

Figure AI-2 Schematic of the bonding strength test of the HA coating to the substrate.

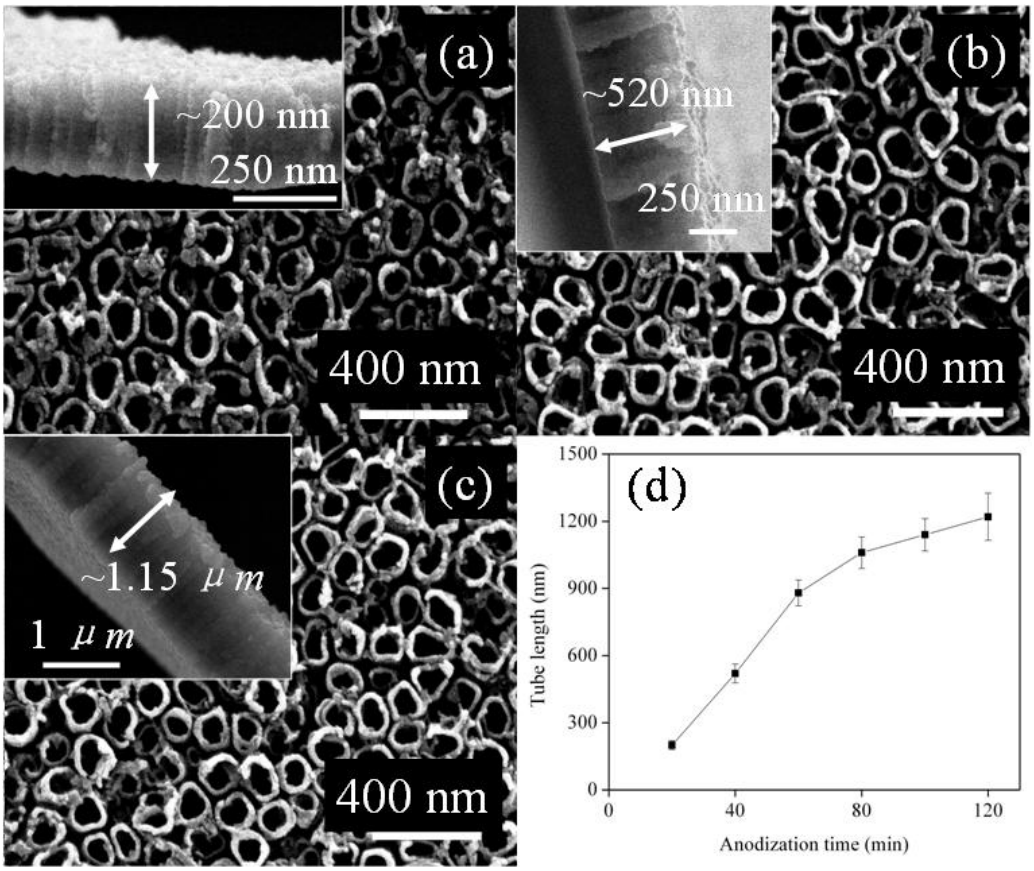

Figure AI-3 FE-SEM images showing top view and the side view (the inserts) of TiO_2 nanotubes after different anodization periods (a): 20 min, (b) 40 min, (c) 100 min, and (d) the relationship between nanotube length and anodization period.

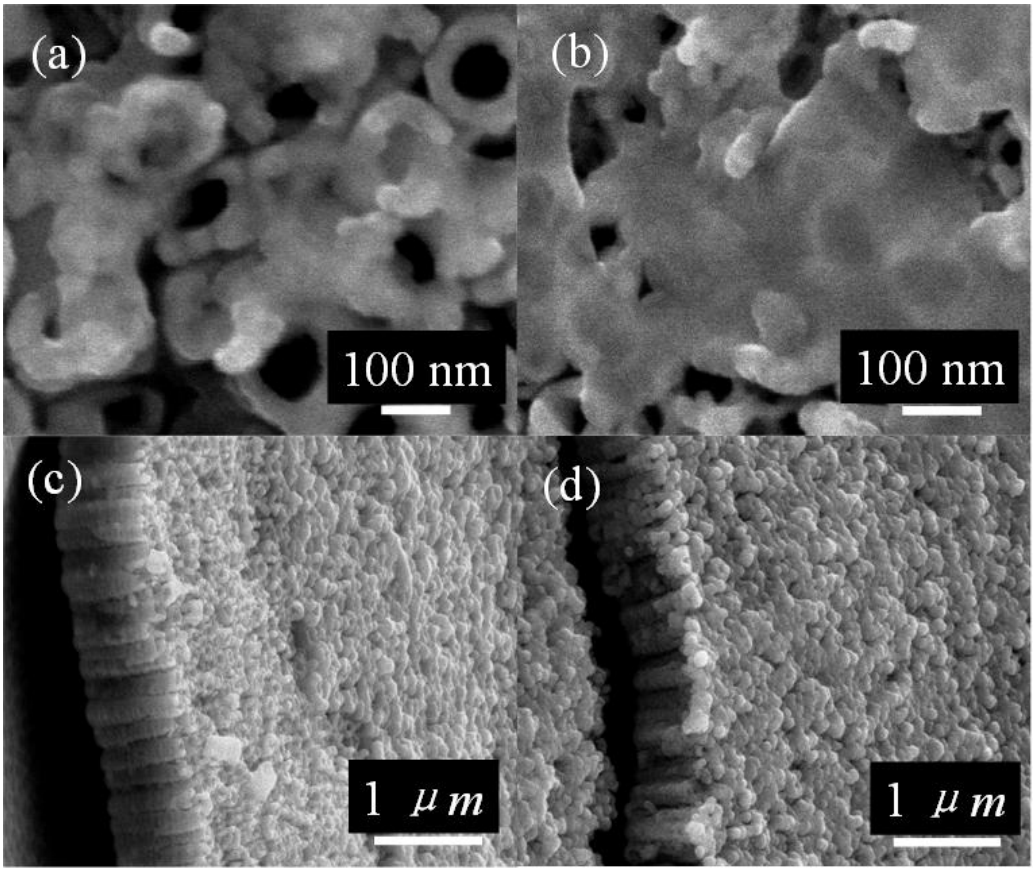

Figure AI-4 FE-SEM images of TiO_2 nanotubes after different numbers of cycles of dipping treatment: (a) and (c) are the top view and side view , respectively, of the TiO_2 nanotubes after dipping for twice; (b) and (d) are the top view and side view, respectively, of the TiO_2 nanotubes after dipping eight times.

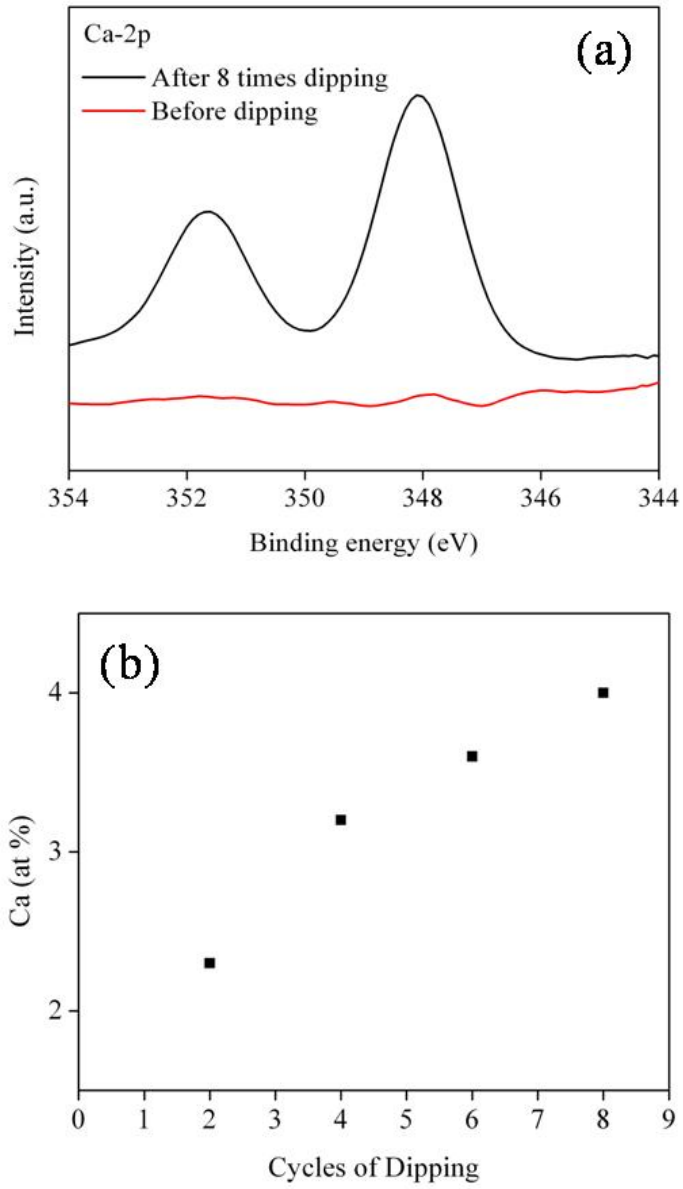

Figure AI-5 (a) XPS spectra showing Ca-2p peaks before and after eight times of dipping treatment, and(b) the atomic concentration of Ca as a function of number of cycles of dipping treatment.

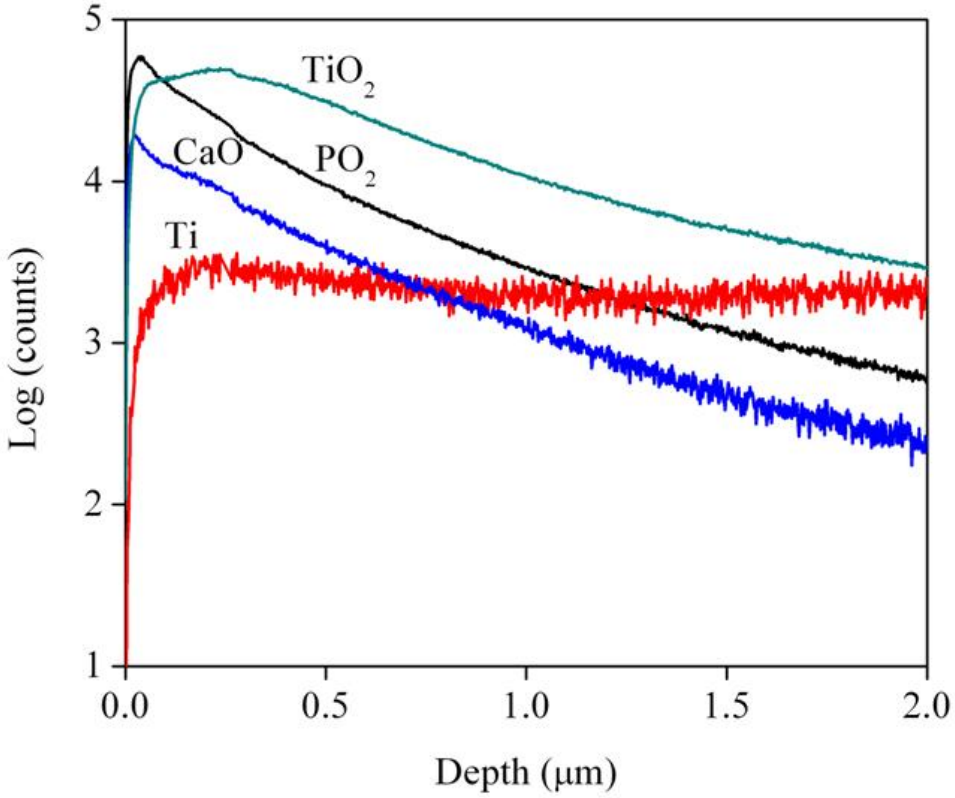

Figure AI-6 SIMS spectra of the TiO_2 nanotube structure after eight times of dipping.

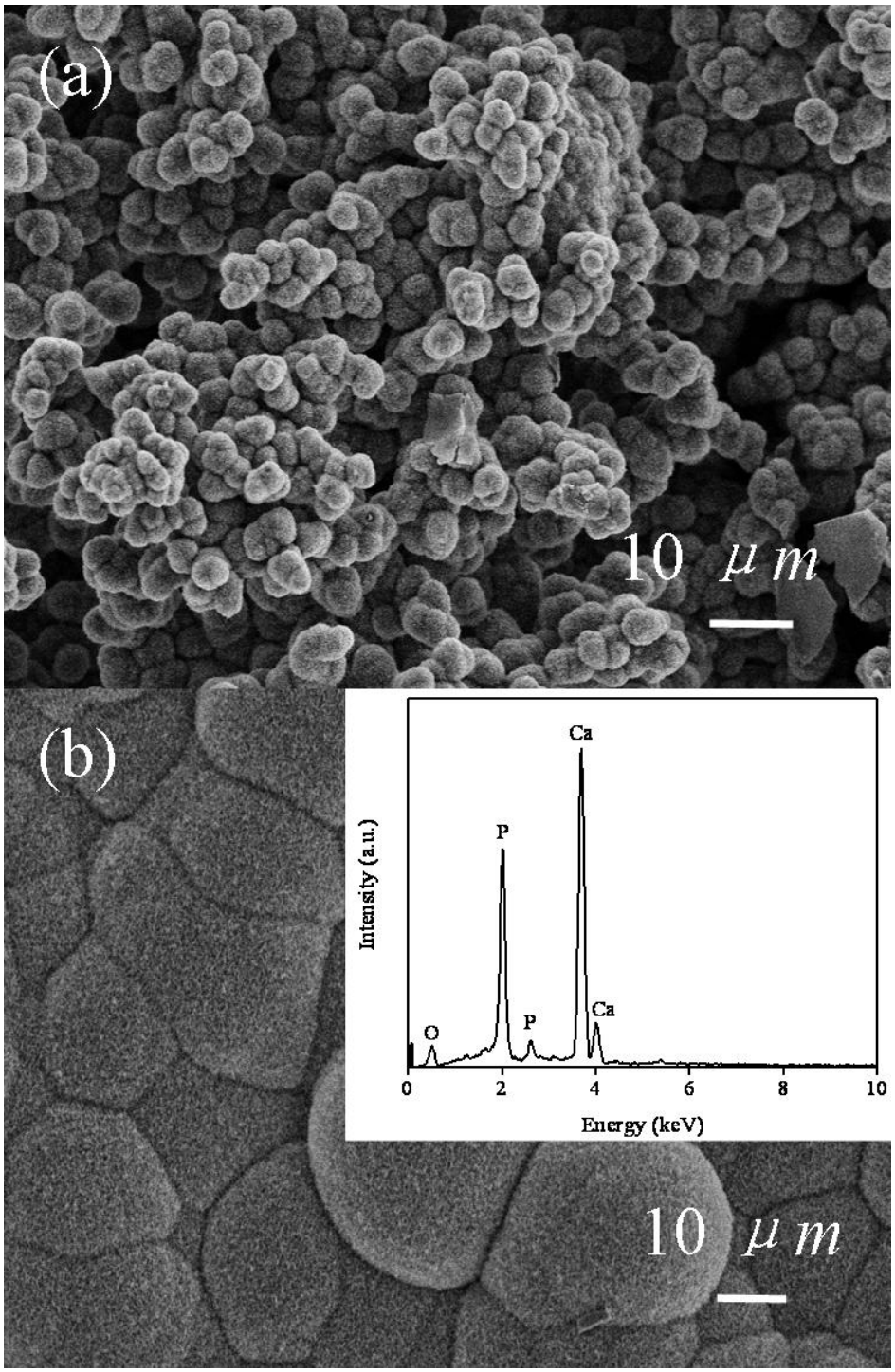

Figure AI-7 SEM images the TiO_2 nanotubes immersed in SBF for different periods:

(a) 2 days and (b) 4 days; the insertion presents the EDX spectrum.

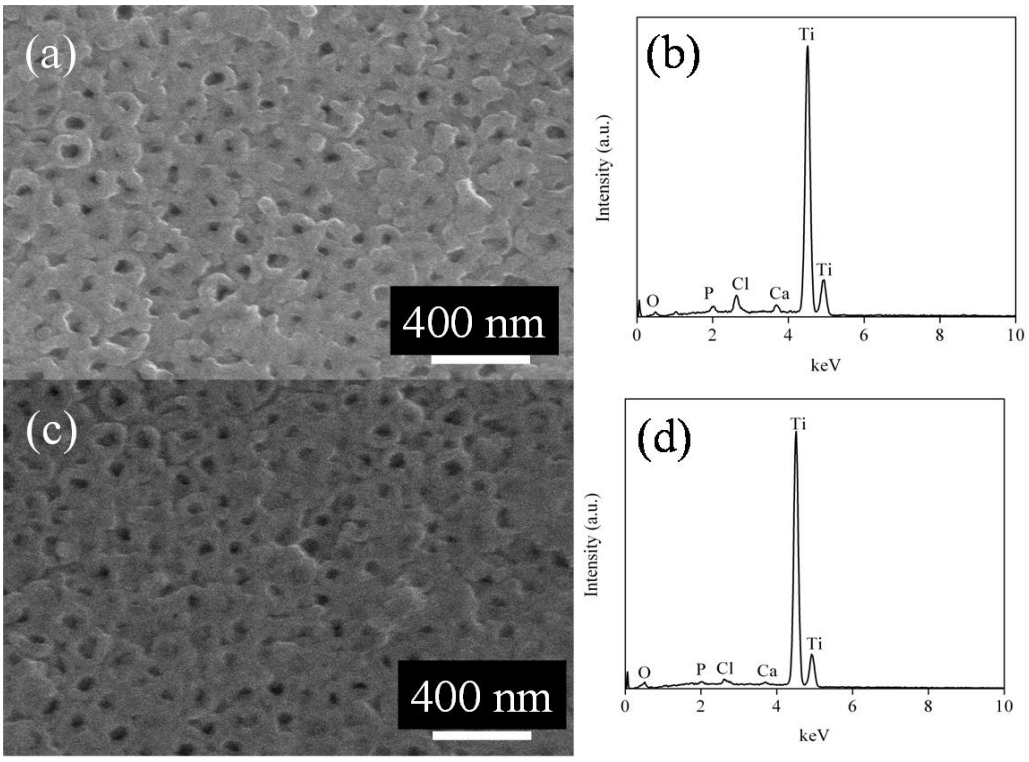

Figure AI-8 (a) SEM images of TiO_2 nanotubes annealed at 723 K (450 ^{o}C) for 3 hr and then immersed in SBF for 4 days and (b) the corresponding EDX spectrum; (c) annealed at 823 K (550 ^{o}C) for 3 h and then immersed in SBF for 4 days and (d) the corresponding EDX spectrum.

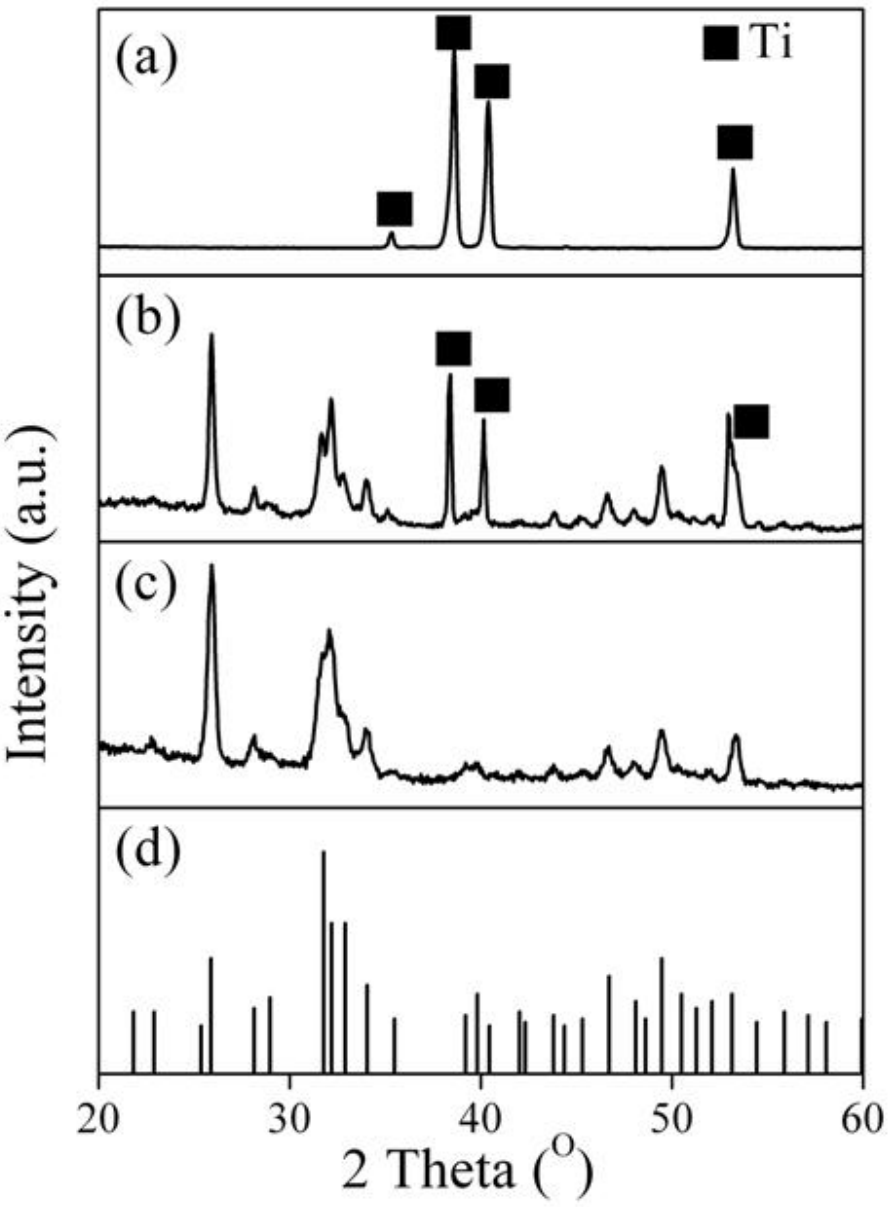

Figure AI-9 TF-XRD patterns of the TiO_2 nanotube structure: (a) before treatment, (b) after immersion in SBF for 2 days, and (c) after 4 days,, and the standard pattern for HA (JCPDF 09-0432).

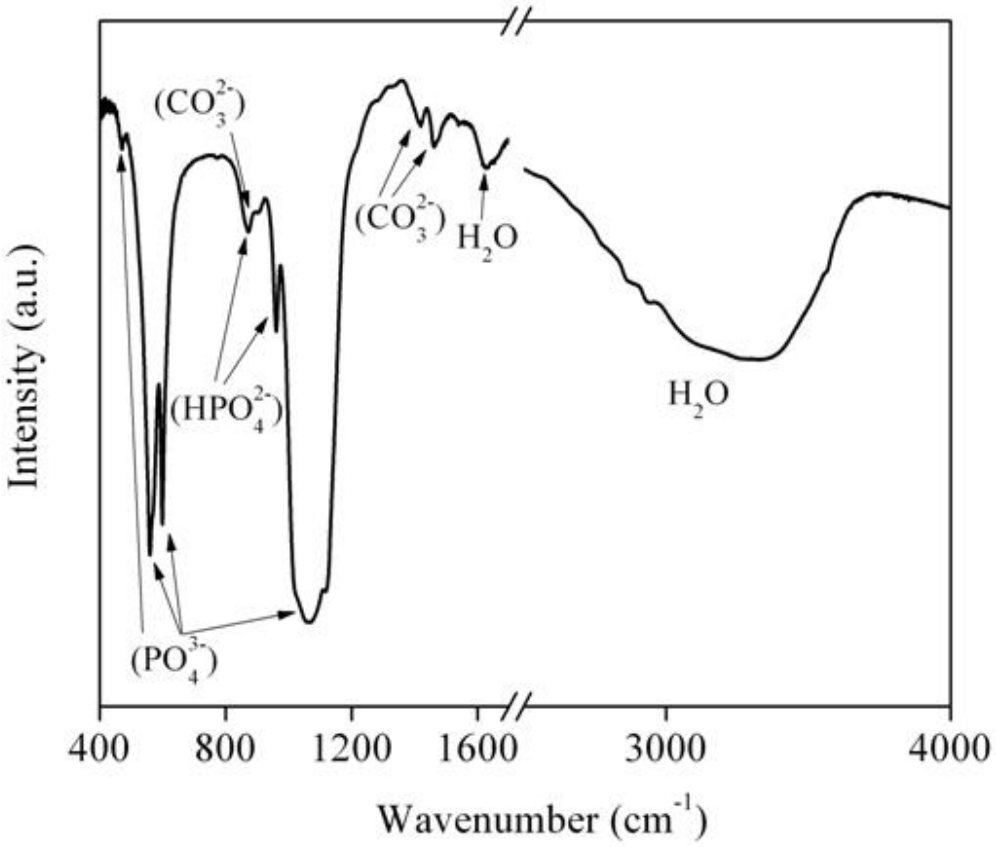

Figure AI-10 FT-IR spectra of the HA coating on TiO_2 nanotubes with dipping treatment after 4 days of immersion in SBF.

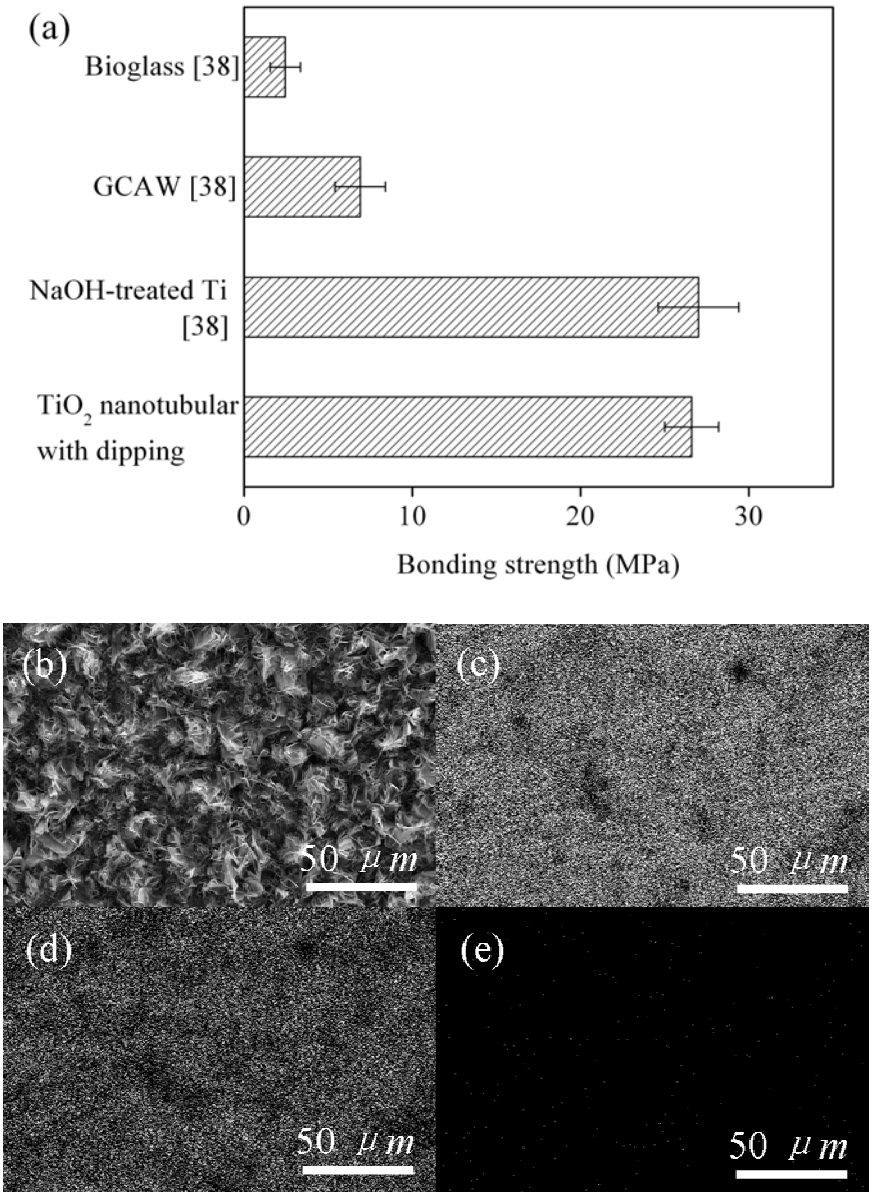

Figure AI-11 (a) Comparison of the tensile bonding strengths of HA layers bonded to different substrates; (b) FE-SEM image of the fracture surface of the substrate; and EDX mapping of the elements (c) Ca, (d) P, and (e) Ti at the fracture surface.

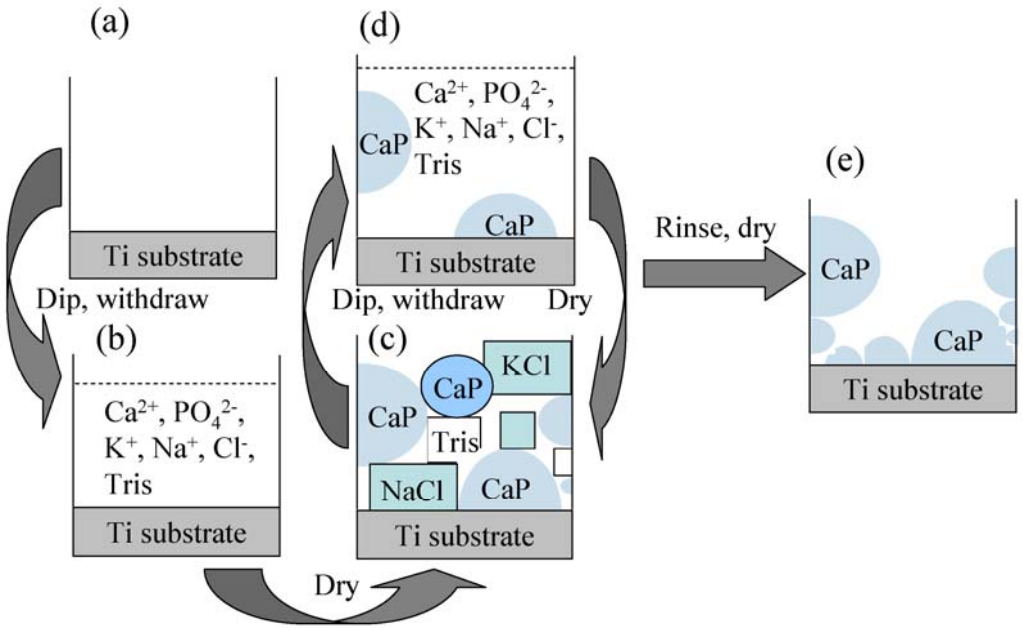

Figure AI-12 Proposed mechanism of the dipping treatment on the TiO_2 nanotube: (a) the Ti substrate with the TiO_2 nanotubes dip and withdraw in the ACS; (b) a wetting film filled in the nanotubes structure; (c) the film dries and results in the formation of CaP crystalline and other chemical crystalline, such as NaCl, KCl, and tris; some CaP adheres to the nanotubes; (d) during the repeated dip-and-withdraw procedures, more and more CaP forms and adheres to the nanotubes; (e) the formation of CaP crystalline covers nanotubes after rinsing and drying (adapted from [25] and [44]).

References

[1] N. Sykaras, A. M. Iacopino, V. A. Marker, R. G. Triplett, R. D. Woody, Implant Materials, Designs, and Surface Topographies: Their Effect on Osseointegration. A Literature Review, Int. J. Oral. Max. Impl., 11 (2000) 675-690.

[2] A. C. Fraker, in: A. C. Fraker, C. D. Griffin, (Eds.), Corrosion and Degradation of Implant Materials, Second International Symposium, American Society for Testing and Materials, Philadelphia, PA, 1985.

[3] S. Tamilselvi, V. Raman, N. Rajendran, Corrosion behaviour of Ti-6Al-7Nb and Ti-6Al-4V ELI alloys in the simulated body fluid solution by electrochemical impedance spectroscopy, Electrochim. Acta 52 (2006) 839-846.

[4] W. Österle, D. Klaffke, M. Griepentrog, U. Gross, I. Kranz, Ch. Knabe, Potential of wear resistant coatings on Ti–6Al–4V for artificial hip joint bearing surfaces, Wear, 264 (2008) 505-517.

[5] M. Textor, C. Sittig, V. Frauchiger, S. Tosatti, D. Brunette: Properties and biological significance of natural oxide films on titanium and its alloys, in: D. Brunette, D. Tengvall, M. Textor, P. Thomsen (Eds.), Titanium in Medicine: Materials Science, Surface Science, Engineering, Biological Responses and Medical Applications, Springer-Verlag, Berlin, 2001.

[6] Y. Han, S.-H. Hong, K. Xu, Structure and in vitro bioactivity of titania-based films by micro-arc oxidation, Surf. Coat. Technol. 168 (2003) 249-258.

[7] R. Wang, K. Duan, Surface modifications of bone implants through wet chemistry, J. Mater. Chem. 16 (2006) 2309-2324.

[8] X. Liu, P. K. Chu, C. Ding: Surface modification of titanium, titanium alloys, and related materials for biomedical applications, Mater. Sci. Eng. R. 47 (2004) 49-124.

[9] Y. Yang, J. L. Ong, J. Tian, Deposition of highly adhesive ZrO_2 coating on Ti and CoCrMo implant materials using plasma spraying, Biomaterials 24 (2003) 619-627.

[10] X. Zhao, X. Liu, C. Ding, Acid-induced bioactive titania surface, J. Biomed. Mater. Res. 75A (2005) 888-894.

[11] D. K. Pattanayak, T. Kawai, T. Matsushita, H. Takadama, T. Nakamura, T. Kokubo, Effect of HCl concentrations on apatite-forming ability of NaOH-HCl- and heat-treated titanium metal, J. Mater. Sci. Mater. Med. 20 (2009) 2401-2411.

[12] H.-M. Kim, F. Miyaji, T. Kokubo, T. Nakamura, Preparation of bioactive Ti and its alloys via simple chemical surface treatment, J. Biomed. Mater. Res. 32 (1996) 409-417.

[13] A. Rakngarm, Y. Miyashita, Y. Mutoh, Formation of hydroxyapatite layer on bioactive Ti and Ti-6Al-4V by simple chemical technique, J. Mater. Sci. Mater. Med. 19 (2008) 1953-1961.

[14] B. Yang, M. Uchida, H.-M. Kim, X. Zhang, T. Kokubo, Preparation of bioactive titanium metal via anodic oxidation treatment, Biomaterials 25 (2004)

1003-1010.

[15] A. Arvidsson, V. Franke-Stenport, M. Andersson, P. Kjellin, Y.-T. Sul, A. Wennerberg, Formation of calcium phosphates on titanium implants with four different bioactive surface preparations An in vitro studyJ. Mater. Sci. Mater. Med. 18 (2007) 1945-1954.

[16] Q. Tang, R. Brooks, N. Rushton, S. Best, Formation of calcium phosphates on titanium implants with four different bioactive surface preparations An in vitro study, J. Mater. Sci. Mater. Med. 21 (2010) 173-181.

[17] M. A. Lopez-Heredia, P. Weiss, P. Layrolle, An electrodeposition method of calcium phosphate coatings on titanium alloy, J. Mater. Sci. Mater. Med. 18 (2007) 381-390.

[18] P. Habibovic, F. Barrère, C. A. Van Blitterswijk, K. De Groot, P. Layrolle, Biomimetic hydroxyapatite coating on metal implants, J. Am. Ceram. Soc. 85 (2002) 517-522.

[19] K. De Groot, R. Geesink, C. P. Klein, P. Serekianm, Plasma sprayed coatings of hydroxylapatite, J. Biomed. Mater. Res. 21 (1987) 1375-1381.

[20] Y. C. Tsui, C. Doyle, T. W. Clyne, Plasma sprayed hydroxyapatite coatings on titanium substrates Part 1: Mechanical properties and residual stress levels, Biomaterials 19 (1998) 2015-2029.

[21] Y. C. Tsui, C. Doyle, T. W. Clyne, Plasma sprayed hydroxyapatite coatings on titanium substrates Part 2: Optimization of coating properties, Biomaterials 19

(1998) 2031-2043.

[22] K. A. Gross, C. C. Berndt, Thermal processing of hydroxyapatite for coating production, J. Biomed. Mater. Res. 39 (1998) 580-587.

[23] Y. C. Yang, E. Chang, Influence of residual stress on bonding strength and fracture of plasma-sprayed hydroxyapatite coatings on Ti-6Al-4V substrate, Biomaterials 22 (2001) 1827-1836.

[24] A. Tonino, C. Oosterbos, A. Rahmy, M. Therin, C. Doyle, Hydroxyapatite-Coated Acetabular Components: Histological and Histomorphometric Analysis of Six Cups Retrieved at Autopsy Between Three and Seven Years After Successful Implantation, J. Bone Jt. Surg. Am. 83 (2001) 817-825.

[25] S. Ono, A. Kiyotake, H. Asoh, Effect of nanostructured surfaces of light metals on hydroxyapatite coating, ECS Trans. 11 (2008) 1-8.

[26] Tsuchiya, J. M. Macak, L. Müller, J. Kunze, F. Müller, P. Greil, S. Virtanen, P. Schmuki, Hydroxyapatite growth on anodic TiO_2 nanotubes, J. Biomed. Mater. Res. 77A (2006) 534-541.

[27] S. Bauer, S. Kleber, P. Schmuki, TiO_2 nanotubes: Tailoring the geometry in H_3PO_4/HF electrolytes, Electrochem Commun. 8 (2006) 1321-1324.

[28] A. Ghicov, H. Tsuchiya, J. M. Macak, P. Schmuki, Titanium oxide nanotubes prepared in phosphate electrolytes, Electrochem Commun. 7 (2005) 505-508.

[29] J. Tao, J. Zhao, C. Tang, Y. Kang, Y. Li, Mechanism study of self-organized

TiO_2 nanotube arrays by anodization, New J. Chem. 32 (2008) 2164-2168.

[30] J. Kunze, L. Müller, J. M. Macak, P. Greil, P. Schmuki, F. A. Müller, Time-dependent growth of biomimetic apatite on anodic TiO_2 nanotubes Electrochim. Acta. 53 (2008) 6995-7003.

[31] J. Park, S. Bauer, K. A. Schlegel, F. W. Neukam, K. Von Der Mark, P. Schmuki, TiO_2 nanotube surfaces: 15 nm, an optimal length scale of surface topography for cell adhesion and differentiation, Small 5 (2009) 666-671.

[32] K. Das, A. Bandyopadhyay, S. Bose, Biocompatibility and in situ growth of TiO_2 nanotubes on Ti using different electrolyte chemistry, J. Am. Ceram. Soc. 91 (2008) 2808-2814.

[33] J. Park, S. Bauer, K. Von Der Mark, P. Schmuki, Nanosize and vitality: TiO_2 nanotube diameter directs cell fate, Nano Lett. 7 (2007) 1686-1691.

[34] X. Xiao, T. Tian, R. Liu, H. She, Influence of titania nanotube arrays on biomimetic deposition apatite on titanium by alkali treatment, Mater. Chem. Phys. 106 (2007) 27-32.

[35] B. Feng, X. Chu, J. Chen, J. Wang, X. Lu, J. Weng, Hydroxyapatite coating on titanium surface with titania nanotube layer and its bond strength to substrate, J. Porous. Mater. 17 (2010) 453-458.

[36] H. B. Wen, Q. Liu, J. R. De Wijn, K. De Groot, F. Z. Cui, Preparation of bioactive microporous titanium surface by a new two-step chemical treatment, J. Mater. Sci. Mater. Med. 9 (1998) 121-128.

[37] T. Kokubo, H. Takadama, How useful is SBF in predicting in vivo bone bioactivity? Biomaterials 27 (2006) 2907-2915.

[38] H.-M. Kim, F. Miyaji, T. Kokubo, T. Nakamura, Bonding strength of bonelike apatite layer to Ti metal substrate, J. Biomed. Mater. Res. Appl. Biomater. 38 (1997) 121-127.

[39] M. Uchida, H.-M. Kim, T. Kokubo, S. Fujibayashi, T. Nakamura, Structural dependence of apatite formation on titania gels in a simulated body fluid, J. Biomed. Mater. Res. 64A (2003) 164-170.

[40] D. K. Pattanayak, T. Kawai, T. Matsushita, H. Takadama, T. Nakamura, T. Kokubo, Effect of HCl concentrations on apatite-forming ability of NaOH-HCl- and heat-treated titanium metal, J. Mater. Sci. Mater. Med. 20 (2009) 2401-2411.

[41] R. Horváthová, L. Müller, A. Helebrant, P. Greil, F. A. Müller, In vitro transformation of OCP into carbonated HA under physiological conditions, Mater. Sci. Eng. C 28 (2008) 1414-1419.

[42] C. Rey, C. Combes, C. Drouet, H. Sfihi, A. Barroug, Physico-chemical properties of nanocrystalline apatites: Implications for biominerals and biomaterials, Mater. Sci. Eng. C 27 (2007) 198-205.

[43] Implants for surgery-hydroxyapatite-part 2: Coating of hydroxyapatite. ISO 13779-2 2008.

[44] K. Duan, A. Tang, R. Wang, A new evaporation-based method for the preparation of biomimetic calcium phosphate coatings on metals, Mater. Sci. Eng.

C 29 (2009) 1334-1337.

[45] A. Kodama, S. Bauer, A. Komatsu, H. Asoh, S. Ono, P. Schmuki, Bioactivation of titanium surfaces using coatings of TiO_2 nanotubes rapidly pre-loaded with synthetic hydroxyapatite, Acta Biomater. 5 (2009) 2322-2330.

[46] E. Landi, G. Celotti, G. Loggroscino and A. Tampieri, Carbonated hydroxyapatite as bone substitute, J. Euro. Ceram. Soc. 23 (2003) 2931-2937.

[47] I. R. Gibson, W. Bonfield, Novel synthesis and characterization of an AB-type carbonate-substituted hydroxyapatite, J. Biomed. Mater. Res. 59 (2002) 697-708.

[48] S. M. Barinov, J. V. Rau, S. Nunziante Cesaro, J. Ďurišin, I. V. Fadeeva, D. Ferro, L. Medvecky, G. Trionfetti, Carbonate release from carbonated hydroxyapatite in the wide temperature range, J. Mater. Sci. Mater. Med. 17 (2006) 597-604.

[49] T. Nakamura, T. Yamamuro, S. Higashi, T. Kokubo, S. Itoo, A new glass-ceramic for bone replacement: evaluation of its bonding to bone tissue, J. Biomed. Mater. Res. 19 (1985) 685-698.